Terahertz Time-Domain Derivative Spectroscopy using MEMS

by

Behnoosh MESKOOB

THESIS PRESENTED TO ÉCOLE DE TECHNOLOGIE SUPÉRIEURE IN PARTIAL FULTILLMENT FOR A MASTER'S DEGREE WITH THESIS IN ELECTRICAL ENGINEERING
M.SC

MONTREAL, DECEMBER 20, 2024

ÉCOLE DE TECHNOLOGIE SUPÉRIEURE
UNIVERSITÉ DU QUÉBEC

BOARD OF EXAMINERS

THIS THESIS HAS BEEN EVALUATED

BY THE FOLLOWING BOARD OF EXAMINERS

Mr. François Blanchard, Thesis Supervisor
Department of electrical engineering at École de technologie supérieure

Mr. Frédéric Nabki, Thesis Co-supervisor
Department of electrical engineering at École de technologie supérieure

Mr. Dominic Deslandes, President of the Board of Examiners
Department of electrical engineering at École de technologie supérieure

Mr. Michaël Ménard, Member of the jury
Department of electrical engineering at École de technologie supérieure

THIS THESIS WAS PRESENTED AND DEFENDED

IN THE PRESENCE OF A BOARD OF EXAMINERS AND PUBLIC

DECEMBER 12, 2024

AT ÉCOLE DE TECHNOLOGIE SUPÉRIEURE

ACKNOWLEDGMENTS

First of all, I would like to thank my supervisor, Prof. Blanchard. He accepted me even when I had no background in this field, and he taught me patiently. His kind support and passion for this field are highly appreciated, and I will never forget it. I am grateful to my co-supervisor, Prof. Nabki, who motivated and inspired me to continue this research and supported me throughout the process. Many appreciation to Dr. Mathieu Gratuze; your help and support were wonderful, merci beaucoup. I thank my colleagues at the TeraÉTS lab and office, who patiently answered my questions and helped me with the lab research. Each one of them supported me with different topics, and I enjoyed learning from them. This research was possible by funding from Prof. Blanchard and Prof. Nabki. I also received research funding from Fonds de Recherche du Québec (FRQNT) for a limited time.

Besides my studies, I worked part-time at Spark Microsystems. I am proud to work there and grateful for their support and flexibility; otherwise, it would not have been possible. They helped me have a healthy balance between studies and work. Working at Spark is not just a job; it gave me a chance to grow professionally, learn French, and plan for my future.

I am blessed with a support network of wonderful people who prayed for me whenever I needed them, cared for my health, supported me spiritually, and allowed me to spend wonderful and meaningful moments with them. I wish I could thank each of you individually, everyone in the society; you are angels. I am forever grateful to Prof. Clément Fortin for the million reasons you know, and I cannot find enough or proper words to express them. You are a guiding light.

Thanks to my friends in Canada and those who are not here and who make this world more beautiful. Thanks to ÉTS SVE for their support with everything a student would need.

Finally, to my family, Mom and Dad, whose unconditional love and support make everything possible, you are the meaning in my life, purpose, light, and joy to live and continue. I dedicate this thesis to my family…

Spectroscopie dérivée dans le domaine temporel térahertz à l'aide de MEMS

Behnoosh MESKOOB

RESUMÉ

Le domaine térahertz (THz), dont les fréquences s'étendent de 0,1 à 10 THz, entre les bandes micro-ondes et infrarouges, fait le lien entre le monde de l'électronique et celui de la photonique. Historiquement, cette partie du spectre électromagnétique (EM) était connue sous le nom de « fossé térahertz » en raison de la complexité de la génération et de la détection de cette onde. Au cours des dernières décennies, les progrès réalisés dans le domaine des lasers ultrarapides et des méthodes de génération et de détection cohérentes ont permis de révéler le potentiel de cette onde unique. La faible énergie de l'onde THz la rend appropriée pour des applications non ionisantes et non destructifs en pénétrant les matériaux non polaires et non métalliques. La spectroscopie THz dans le domaine temporel (THz-TDS) est un outil robuste qui tire parti des caractéristiques des ondes THz pour de nombreuses applications, de la caractérisation des matériaux aux applications pharmaceutiques, en passant par les communications, le contrôle de la qualité des dispositifs à semi-conducteurs et l'imagerie. Cet outil fournit des informations sur la nature transitoire du champ électrique qui peuvent aider à obtenir l'amplitude et la phase du signal.

Une approche innovante pour améliorer le THz-TDS consiste à ajouter un modulateur dans le système et à obtenir une spectroscopie dérivée dans le domaine temporel du THz (THz-TDDS). La fonction dérivée met en évidence les changements rapides et permet d'améliorer les caractéristiques spectrophotométriques. Le développement de la THz-TDDS a connu des avancées limitées, ce qui motive ma recherche d'une méthode d'amélioration de la THz-TDDS. Par conséquent, un MEMS disponible dans le commerce est utilisé dans le trajet du faisceau THz pour moduler le faisceau THz. Bénéficiant des travaux antérieurs réalisés à l'ÉTS dans ce domaine spécifique, les objectifs de la recherche consistent à sélectionner un MEMS présentant de meilleures caractéristiques et à améliorer les fonctions de modulation. La première étape consiste à prouver la fonctionnalité dérivée de cette installation THz par une vérification mathématique et une simulation. Quatre matériaux sont étudiés pour valider les performances spectroscopiques du THz-TDDS, et les paramètres optiques, y compris l'indice de réfraction et le coefficient d'absorption pour chaque matériau, sont calculés. Les capacités spectroscopiques de ce dispositif sont démontrées en comparant les résultats obtenus avec un dispositif commercial très précis et avec la littérature disponible. L'étape finale consiste à étudier les sources d'erreur, à fournir des recommandations d'amélioration pour les perspectives de recherche futures et à suggérer la conception et l'application d'un réseau de MEMS dans l'imagerie THz.

L'un des objectifs de cette recherche est de démocratiser l'application des MEMS dans le domaine THz. Cependant, il existe un compromis entre certains paramètres, tels que la

reproductibilité et l'accessibilité financière, et un faible rapport signal/bruit (RSB). En outre, toutes les installations de recherche disposant de systèmes avancés similaires, tels que le laser femtoseconde disponible dans le laboratoire THz de l'ÉTS, peuvent bénéficier de cette approche d'utilisation d'un MEMS commercial, et diverses applications nouvelles peuvent être envisagées.

Cette thèse débute par l'exposition de l'introduction et des éléments centraux de la recherche. Le premier chapitre présente le contexte et l'analyse de la littérature pour situer cette recherche et montrer la pertinence de la solution proposée en réponse aux lacunes de la recherche. Ce chapitre présente la méthodologie et les résultats. Le troisième chapitre aborde les sources d'erreur, et enfin, le dernier chapitre fournit des recommandations pour d'autres options MEMS, des améliorations, des progrès et des leçons apprises.

Mots-clés: THz-TDS, THz-TDDS, modulation de faisceau, MEMS, indice de réfraction, coefficient d'absorption

Terahertz time-domain derivative spectroscopy using a MEMS

Behnoosh MESKOOB

ABSTRACT

The Terahertz (THz) domain, with frequencies spanning from 0.1 to 10 THz, between microwave and infrared bands, bridges the gap between the electronics and photonics worlds. Historically, this part of the electromagnetic (EM) spectrum was known as the “terahertz gap” due to complexities in generating and detecting THz waves. In the past decades, considering the advancements in ultrafast lasers and coherent generation and detection methods, the potential of this unique wave has been revealed. The low energy of THz wave makes it suitable for non-ionizing and non-destructive applications by penetrating non-polar and non-metallic materials. THz time-domain spectroscopy (THz-TDS) is a robust tool that benefits from THz wave features for numerous applications, from material characterization to pharmaceutical applications, communications, semiconductor device quality control, and imaging. This tool provides information about the electrical field's transient nature that can help obtain the signal's amplitude and phase.

An innovative approach to improve the THz-TDS is to add a modulator in the system and obtain THz time-domain derivative spectroscopy (THz-TDDS). The derivative function highlights the rapid changes and helps improve spectrophotometric features. There have been limited advancements in THz-TDDS development, which motivates my research to investigate an enhancement method for THz-TDDS. Therefore, a commercially off-the-shelf MEMS is used in the THz beam path to modulate the THz beam. Benefiting from previous work done at ÉTS in this specific field, the research goals are selecting a MEMS with better characteristics and improving the modulation features. The first step includes proving the derivative functionality of this THz setup with mathematical verification and simulation. Four materials are studied to validate the spectroscopic performance of the THz-TDDS, and the optical parameters, including refractive index and absorption coefficient for each material, are calculated. Comparing the results of this setup against a commercial and highly accurate device and comparing it with the available literature, the spectroscopic capabilities of this setup are proven. The final step is to investigate and scrutinize the error sources, provide recommendations for improvement for future research prospects, and suggest the design and application of an array of MEMS in THz imaging.

One of the goals of this research is to expand the use of MEMS in THz applications. However, there is a trade-off between some parameters, such as reproducibility and affordability, and low signal-to-noise ratio (SNR). Moreover, all research facilities with similar advanced systems, such as the femtosecond laser available at the TeraÉTS THz lab, can benefit from this approach of utilizing a commercial MEMS, and various novel applications can be envisioned.

This thesis begins by outlining its essential research objectives and framework. The first chapter provides the background and literature review to place this research and show the relevance of the proposed solution in response to the research gaps. It also details the methodology employed and the corresponding experimental results. The third chapter discusses the sources of error and their impact on the results, and finally, the last chapter provides recommendations for future works and lessons learned. Finally, the Annexes will provide the simulation and Matlab scripts utilized in this thesis.

Keywords: THz-TDS, THz-TDDS, beam modulation, MEMS, refractive index, absorption coefficient

TABLE OF CONTENTS

Page

LIST OF TABLES

LIST OF FIGURES

Page

LIST OF ABBREVIATIONS

EM	Electromagnetic
THz-TDS	Terahertz time domain spectroscopy
THz-TDDS	Terahertz time domain derivative spectroscopy
MEMS	Microelectromechanical system
SNR	Signal to noise ratio
SPI	Single pixel imaging
CS	Compressed sensing
EOS	Electro-optic sampling
OR	Optical rectification
PCA	Photoconductive antenna
LT-GaAs	Low temperature grown Galium Arsenide
SI-GaAs	Semi-insulating GaAs
ZnTe	Zinc Telluride
LiNbO3	Lithium Niobate
DR	Dynamic range
RMS	Root mean square
FT	Fourier transform
FFT	Fast Fourier transform
PCS	photoconductive sampling
ECG	Electrocardiogram
DS	Derivative spectroscopy
DTDS	Differential time domain spectroscopy

DMD	Digital micromirror device
IR	Infrared
THz-QCLa	Terahertz quantum cascade laser
PRD	Period jitter
TIE	Time interval error jitter
CtoC	Cycle to cycle jitter
RJ	Random jitter
BUJ	Bounded uncorrelated jitter
DDJ	Data-dependent jitter
DCD	Duty cycle distortion
ISI	Inter-symbol interference
STD	Standard deviation
PDF	Probability density function
PMUT	Piezoelectric micromachined ultrasonic transducer
PM	Piezoelectric michromachined
MD	Modulating device
LIA	Lock-in amplifier
LPF	Low-pass filter
BPF	Band-pass filter
RC	Resistor-capacitor
TPC	Total power control
Yb	Ytterbium

Tx	Transmitter (Emitter)
Rx	Receiver (Detector)
TPX	Polymethylpentene
PSD	Power spectral density
psd	phase-sensitive detection
RIN	Relative intensity noise
CEO	Carrier envelope offset
DFT	Discrete Fourier transform
GUI	Graphical user interface
FDTD	Finite-difference time-domain

LIST OF SYMBOLS

THz	Terahertz
$\bar{E}$	Mean magnitude of amplitude
S_E	Standard deviation of amplitude
E_{max}	Maximum magnitude of amplitude
N_{rms}	RMS of noise floor
j_n^{PRD}	Periodic jitter
j_n^{TIE}	Time interval error jitter
j_n^{CtoC}	Cycle to cycle jitter
$\theta(t)$	Phase noise
j^{PHS}	Phase jitter
$f_{RJ}(\Delta t)$	PDF of Random jitter
μ_{RJ}	Mean of random jitter
${\sigma_{RJ}}^2$	Variance of random jitter
τ	Period
$n(\omega)$	Refractive index
$\varphi(\omega)$	Phase difference between reference and material signal
$\alpha(\omega)$	Absorption coefficient
$T(\omega)$	Transmission
S_y^{DS}	Double-sided PSD
S_y^f	Single-sided PSD

INTRODUCTION

Background and motivation

Terahertz (THz) technology covers the techniques and applications in the electromagnetic (EM) spectrum within the frequency range from 0.1 to 10 THz, situated between microwaves and infrared (Pacheco-Peña, 2021). The particular features of THz waves make them especially attractive for non-invasive applications and spectroscopic studies, including sensing. Unlike X-rays, THz radiation is non-ionizing and thus safe to be applied to biological samples (Jepsen et al., 2011). It retains the advantages of X-rays in penetration into non-polar and non-metallic materials, such as clothes, plastics, and biological tissues, opening perspectives for applications in security screening, medical imaging, and material characterization (Dragoman & Dragoman, 2004; Jepsen et al., 2011).

Terahertz time-domain spectroscopy (THz-TDS)(Ghann & Uddin, 2017) has revolutionized the approach toward the analysis of materials at a molecular level and has provided significant insights into molecular and rotational vibrations and intermolecular interactions (Dragoman & Dragoman, 2004; King et al., 2013; Pawar et al., 2013). This technique is of paramount importance in studying biological tissues (King et al., 2013), semiconductors (Jepsen et al., 2011), and chemical compositions with resonances in the terahertz frequency regime (Pawar et al., 2013). One of the significant challenges in THz spectroscopy is signal-to-noise ratio (SNR) enhancement, usually limited by sources and detectors or environmental conditions like humidity (Naftaly, 2013; Naftaly & Dudley, 2009).

Application of microelectromechanical systems (MEMS) within terahertz systems (Akalin & Treizebré, 2006; Anwar et al., 2009; Cox et al., 2009; Dragoman & Dragoman, 2004) represents a novel solution for many application or integration challenges, including beam modulation (Amirkhan, Robichaud, et al., 2020) and noise reduction (Amirkhan et al., 2021). The small size and precise control of MEMS devices provide new ways of dynamic modulation of THz beams (Amirkhan, Gratuze, et al., 2020; Amirkhan, Robichaud, et al., 2020; Amirkhan

et al., 2021) and extend their adaptability and configuration in THz imaging systems (Béliveau, 2022a). However, employing MEMS in such systems introduces jitter, phase noise, and fluctuations in the THz signal, which can degrade the SNR.

Problem statement

This thesis addresses a challenge in terahertz spectroscopy, focusing primarily on the issues related to signal quality, noise, and setup complexity. I discuss improving the spectroscopy technique by incorporating MEMS-based beam modulation. The focus is on utilizing MEMS in THz-TDS and understanding the impact of MEMS jitter on the SNR. Despite the advances in THz spectroscopy, limited research has explored the challenges of utilizing MEMS in spectroscopy and discussed how MEMS-induced jitter impacts SNR in practical THz applications.

Research objectives

- To investigate the use of MEMS to modulate THz beams and understand how jitter impacts SNR in THz spectroscopy to help improve future implementations.
- Develop the experimental setup of THz-TDDS and validate the results using a commercial system (Toptica TeraFlash Pro), verifying the results with established literature results for the refractive index and absorption coefficient of the four materials (glucose, lactose, maltose, and fructose).
- Propose necessary features for the modulating device to enhance spectroscopy performance and overall system functionality.
- For future work, propose to utilize an array of MEMS in imaging to reduce complexity and increase functional parameters such as power loss and speed.

Hypothesis

Incorporating a commercially available modulating device (MEMS) into the THz-TDS framework to achieve THz-TDDS will provide enhanced spectroscopic capabilities compared to conventional THz-TDS. Significantly, MEMS utilization is hypothesized to improve the signal quality and sensitivity to subtle spectral features through the derivative functionality,

enable the determination of materials' optical parameters that correspond to measurements with a commercial setup and literature, and provide an accessible approach that can be extended to design MEMS arrays for advanced applications such as THz imaging, ultimately broadening the scope and applicability of MEMS in THz technology and applications.

Contribution

The outcome of this thesis provides the foundation for improving the THz imaging methods and gives insight into the utilization of MEMS in THz technologies. To the best of our knowledge, this is the first time that MEMS-induced jitter and phase noise have been investigated in the context of THz spectroscopy.
The results will be published in a journal, and one article has already been published in a conference as follows:

- Journal article: To be submitted

Meskoob B., Gratuze M., Gandubert G., Ropagnol X., Nabki F., and Blanchard F.: "Terahertz time-domain derivative spectroscopy using a piezo speaker as a modulator", to be submitted at IOP.

- Conference article:

Meskoob, B., Gratuze, M., Gandubert, G., Ropagnol, X., Nabki, F., & Blanchard, F. (2024, July). Terahertz Time-Domain Derivative Spectroscopy of Fructose using a MEMS Piezo Speaker. In Novel Optical Materials and Applications (pp. NoW3H-3). Optica Publishing Group. [One of the best student papers' finalists]

Thesis structure

The thesis structure, headlines, and the content of each chapter are briefly presented here:
Introduction: The first chapter provides a general overview of the thesis by presenting the research background, problem statement, objectives, hypothesis, and thesis structure.
Chapter 1- Literature Review: Fundamental topics discussed in this thesis will be explained to provide the necessary information. The topics include the current state of research in THz technology, spectroscopy, MEMS-based beam modulation, and jitter.

Chapter 2- Methodology and results: The experimental setup is explained in detail, measurement and validation methodology are presented, and the results are given. The experimental results obtained by the THz-TDDS are verified by doing the same measurements using a commercial THz-TDS system. The underlying causes of discrepancies will be investigated in the next chapter.

Chapter 3- Phase Noise, Jitter, and SNR: The most impactful sources of error caused by the modulating device are the phase noise, jitter, and their effects on the SNR. These parameters are explained mathematically, providing the foundation for simulations. The simulation results explain the discrepancies observed in the previous chapter. Furthermore, the performance of this modulating device is compared with the previous research in terms of SNR and quality factor.

Conclusion and recommendations: Finally, the conclusions are drawn, and recommendations for the continuation of this project are presented. Valuable lessons have been learned during this research, which will be shared with the readers, and future goals are discussed as well.

CHAPTER 1

LITERATURE REVIEW

In this chapter, I will present the literature review on the key topics discussed in the thesis, provide the necessary background and information about the subject, and place my research within the existing literature.

1.1 Overview of the terahertz technology

The terahertz frequency range is between the microwaves and the infrared part of the electromagnetic spectrum. As a growing area of scientific research and technological progress, this range includes frequencies from 0. 1 THz to 10 THz with wavelengths ranging from approximately 3 mm to 30 µm, from 3.33 cm^{-1} to 333.56 cm^{-1} wavenumber, and 413 µeV to 41.3 meV photon energy (Ghann & Uddin, 2017; Pawar et al., 2013). Thanks to the use of coherent emission and detection methods, terahertz radiation is well known for its short pulse durations, generally in the picosecond range, enabling high temporal resolution and spectral bandwidth. (Pawar et al., 2013). This field is expected to cater for a wide range of advanced applications such as security (H.-B. Liu et al., 2007), biomedical (Sun et al., 2017), non-destructive characterization (Nsengiyumva et al., 2023), and communications (Song & Nagatsuma, 2011). Figure 1.1 presents the definition of the THz band (Nagatsuma, 2011).

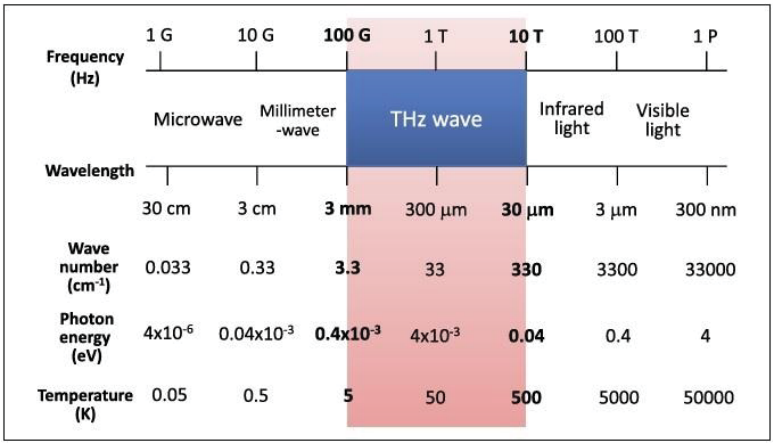

Figure 1.1 THz band definition
Taken from (Nagatsuma, 2011, p.1131)

1.2 Generation and detection

The advancements in ultrafast lasers and coherent generation and detection methods have enabled significant advancements across various fields (Bogue, 2018). Photoconductive antennas (PCA), commonly constructed using Low-Temperature Grown GaAs (LT-GaAs) or Semi-Insulating GaAs (SI-GaAs), harness the photocurrent produced in a semiconductor material by rapid laser pulses to create THz waves (Tani et al., 2002). Optical rectification (OR) benefits from crystals (Gordon et al., 2006), like Zink Telluride (ZnTe) (D. Li & Ma, 2008) or Lithium Niobate ($LiNbO_3$) (Hirori et al., 2011), that possess a second-order nonlinear optical susceptibility. When a femtosecond laser pulse passes through a nonlinear medium, an induced polarization results from the charge displacement in the medium. This second-order polarization describes the optical rectification. When the group velocity of the laser pulse and the phase velocity of the generated THz pulse are the same in the crystal, an efficient THz generation can be achieved (Nuss & Orenstein, 2007).

When it comes to detection methods of THz signals, electro-optic sampling (EOS) (Jepsen et al., 2011) utilizes the Pockels effect to gauge the THz field through monitoring changes in the polarization of an ultrafast laser probe pulse (Wu & Zhang, 1995). As another example, optical heterodyne allows for the detection of the THz field by converting the signal to a lower, intermediate frequency (down-converting) that can be easily measured (Lin & Jarrahi, 2020).

1.2.1 Photoconductive antenna for generation and detection

A typical PCA consists of two electrodes deposited on a semiconductor. These electrodes are biased by a voltage. A femtosecond pulse laser focuses between the two electrodes. It generates a THz pulse, as shown in Figure 1.2, where an optical pulse with $\hbar\omega$ energy makes contact with the antenna substrate between the two electrodes, which are supplied by DC voltage. When the photons of the laser pulse have higher energy than the semiconductor bandgap, they can generate free electrons. Therefore, pairs of holes and electrons or charge carriers move from the semiconductor's valence band to its conduction band, and shortly, the semiconductor changes from an insulator to a conductor. The polarization field accelerates the free charge

carrier in one direction and generates the photocurrent. The THz pulse is obtained by the variations in the photocurrent. A transient current is generated between the electrodes fed with the bias voltage. The electric field of the THz pulse is proportional to the derivative of this photocurrent as $E_{THz}(t) \propto \frac{dj(t)}{dt}$. The shape and length of the PCA electrodes are essential parameters to shape the diffraction pattern of the emitted waves. Figure 1.2 presents a photoconductive switch for THz generation (Jepsen et al., 2011). In this thesis, the detector utilized is a TeraVil free-space THz emitter based on GaAs photoconductive material with parallel strip line conductors. This emitter is suitable for the photon energy of the 800 nm pump beam laser with relatively low intensity but with high cost of antenna.

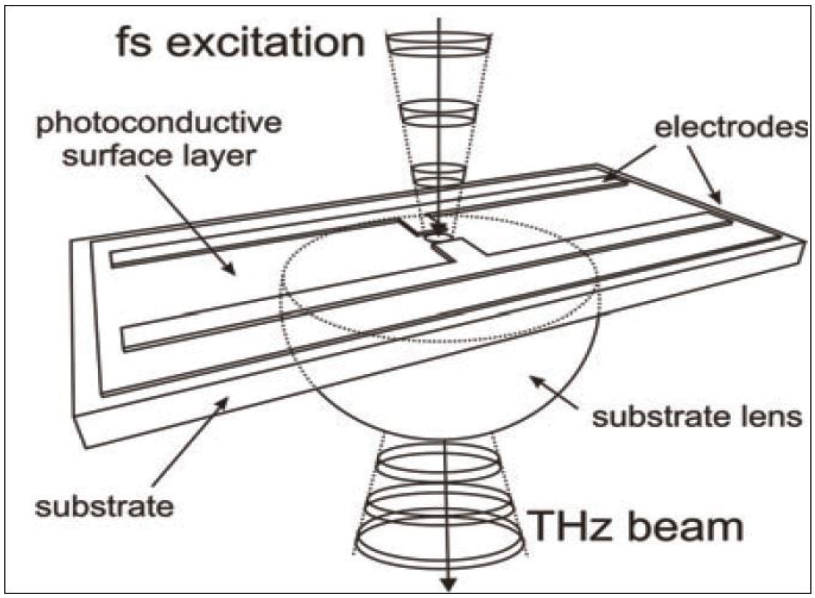

Figure 1.2 Generation of THz pulse by photoconductive switch
Taken from (Jepsen et al., 2011, p.126)

Similar to generation, the THz pulse detection can be done by PCA without biasing the antenna. The probe laser is focused on the antenna and makes the semiconductor substrate conducive for the laser pulse duration. When the arrival of the optical probe beam is matched with the arrival of the THz pulse, the photocurrent is generated between the antenna electrodes, which is linearly proportional to the amplitude of the THz electric field. Thus, the THz signal is acquired (Jepsen et al., 2011). For this thesis, a Batop bowtie PCA (bPCA-100-05-10-800)

is utilized as the detector (Rx). Figure 1.3 presents the microscopic image of the bowtie electrode of the Batop detector.

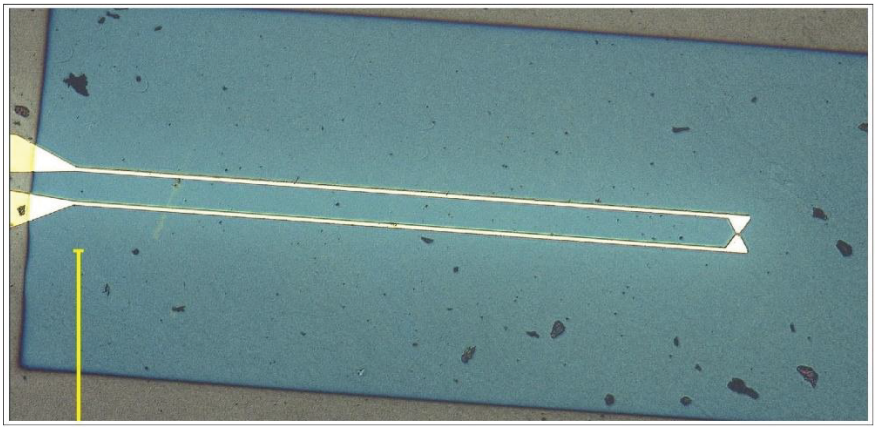

Figure 1.3 Microscopic view of the Batop PCA detector

1.2.2 Parameters and features

Terahertz technology has attracted the interest of researchers and engineers due to its distinctive features and application in spectroscopy, imaging, and high-speed wireless communications (Petrov et al., 2016). In addition to the features mentioned earlier, THz technology has been highly beneficial for assessing materials without causing harm or altering their composition and, allowing the examination of structures and identifying defects in a non-destructive manner (Wietzke et al., 2010). A powerful method that has drawn interest is THz time-domain spectroscopy (THz-TDS) (Jepsen et al., 2011).

Key indicators and figures of merit for THz technology include sensitivity, resolution, dynamic range, and signal-to-noise ratio (SNR) (Jepsen et al., 2011; Withayachumnankul & Naftaly, 2013). Sensitivity is crucial for detecting weak signals, while resolution determines the ability to distinguish between closely spaced spectral features. Dynamic range refers to the range of signal amplitudes that can be accurately measured (Withayachumnankul & Naftaly, 2013). These figures of merit are critical for ensuring the reliability and accuracy of measurements in the THz domain.

The importance of sensitivity is in its role in detecting weak signals effectively. It is commonly assessed by signal strength and is impacted by factors like SNR, detector responsivity, and resolution (Bogue, 2018; Withayachumnankul & Naftaly, 2013).

The resolution of a THz system refers to its capacity to differentiate between different frequencies or wavelengths of THz radiation and the ability to resolve closely spaced spectral lines (Neu & Schmuttenmaer, 2018). The signal-to-noise ratio and the dynamic range (DR) of a system (in frequency domain) have the following definitions (Withayachumnankul & Naftaly, 2013):

$$SNR = \frac{mean\ magnitude\ of\ THz\ signal\ amplitude}{standard\ deviation\ of\ THz\ signal\ amplitude} = \frac{\bar{E}}{S_E} \tag{1.1}$$

$$DR = \frac{maximum\ magnitude\ of\ amplitude}{RMS\ of\ noise\ floor} = \frac{E_{max}}{N_{rms}} \tag{1.2}$$

S_E is the standard deviation, and RMS is the root mean square (Naftaly & Dudley, 2009; Withayachumnankul & Naftaly, 2013).

SNR and DR offer complementary perspectives on how a system performs; SNR shows the slightest signal change that can be detected, while DR reveals the largest measurable signal change possible within a system's operation range. When it comes to TDS systems, to evaluate the SNR and DR in either a time domain or the spectrum obtained via Fourier transform (FT), the noise found in the time domain trace is directly derived from the measurement data. Therefore, the SNR and DR should be calculated according to the nature of the measurement being performed. SNR and DR are different for spectral or temporal data and depend on frequency (Naftaly & Dudley, 2009; Withayachumnankul & Naftaly, 2013).

1.3 Terahertz time-domain spectroscopy

Terahertz time-domain spectroscopy (THz-TDS), a cutting-edge approach with applications in THz sensing and imaging fields, has recently gained attention. This technique allows for the measurement of both the phase and amplitude of THz pulses over time (Jepsen et al., 2011).

The frequency-dependent optical properties of materials can be studied by applying the Fourier transform to the time-domain measurement data (Jepsen et al., 2011). THz-TDS technique permits the characterization of parameters such as transmission, refractive index, and absorption coefficients for materials such as biological samples, pharmaceutical products, and chemical compounds (Bogue, 2018; Jepsen et al., 2011; Roux et al., 2014). For instance, (Y. Liu et al., 2019) utilized THz-TDS to obtain the characteristics of amino acids, explaining information about their movements and interactions between molecules.

1.3.1 Advantages of THz-TDS

- Fast dynamic processes can be observed with high temporal resolution.
- With coherent generation and detection, b oth amplitude and phase information can be directly measured.
- A wide range of materials, including liquids, gases, and solids, can be studied (Jepsen et al., 2011).

1.3.2 Disadvantages of THz-TDS

- Time domain measurements are highly susceptible to noise, complicating data interpretation (Duvillaret et al., 2000).
- Careful calibration and signal processing techniques are required to ensure accurate results (Withayachumnankul & Naftaly, 2013).

Knowing the potential of THz-TDS and considering the shortcomings, one viable improvement path would be time-domain derivative spectroscopy.

1.4 Terahertz time-domain derivative spectroscopy

THz-TDS is a powerful technique but suffers from some limitations. One key shortcoming is that broad, dominating peaks can obscure subtle spectral features, making it difficult to distinguish fine structural or compositional details. In addition, slight variations in refractive index or absorption coefficients may not stand out clearly against the overall signal. Noise and

baseline fluctuations further complicate the extraction of weak resonances. Therefore, The development of THz time-domain derivative spectroscopy (THz-TDDS) is recommended, which would further extend the capabilities of THz-TDS features, as highlighted by (Amirkhan et al., 2021). This technique is built upon the conventional THz-TDS framework by introducing an additional step: the differentiation of the time-domain signal, either numerically or through hardware implementation. The advantages of THz-TDDS are improved SNR (Amirkhan et al., 2021), resolution enhancement of spectral features (Klein & Dratz, 1968), identification of overlapping spectral lines (Collier & Singleton, 1957), and subtle absorption change detection (Karpinska, 2004). Several researches have been conducted to dive into its applications and study the spectral characteristics of various materials.

The derivative is a mathematical function used to determine signal change rate in several applications, such as mathematical modeling of complex products, design optimization, and manufacturing (Yan, 2014). One of the applications is in analyzing electrocardiogram (ECG). One way to use the derivative of an ECG signal in a cardiac cycle is to recognize when the QRS complex begins (Langner & Geselowitz, 1962). By highlighting where changes occur (inflection points) and how fast they happen in the ECG signal data points over time, the derivative function can provide information that helps identify different heart conditions (Arzeno et al., 2006).

In the spectroscopic studies, across frequency ranges like infrared to THz bands, several methods and applications are being explored. An example would be the study by (Collier & Singleton, 1957) that emphasizes the benefits of utilizing derivative function in infrared spectroscopy, specifically the application of derivatives in complex mixtures, providing better efficiency in the quantitative investigation of substances compared to conventional techniques. The researchers also pointed out shortcomings due to absorption overlap in optical density measurements, which led to inaccurate results. Using a derivative approach, they could address challenges by enabling independent evaluations of elements, even in complex mixtures.

In another study (Klein & Dratz, 1968), derivative spectroscopy has significantly improved the clarity of absorption spectra readings. They highlight the importance of derivation in unveiling details not easily seen in absorption spectra by showcasing examples such as examining

bacteriochlorophyll protein complexes and studying ethylbenzene properties. The article presents electronic differentiation methods to create derivative spectra from electrical signal-generating devices where the signals are proportional to the absorption, which is effective with the cost of precise calibration. The obstacles related to noise in derivative spectra are discussed. The trade-off is mentioned on how, despite having a lower signal-to-noise ratio compared with the absorption spectra, the better resolution outweighs the drawbacks if appropriately addressed.

Historically investigating this field (Stauffer & Sakai, 1968) offers an extensive analysis of the derivative spectroscopy method and highlights its benefits compared to traditional spectroscopy approaches initially introduced by (Giese & French, 1955). This paper discusses how derivative spectroscopy can enhance the detectability of overlapping spectral lines. Research by (Collier & Singleton, 1957) discusses the background theories on these methods and presents the mathematical principles supporting derivative spectroscopy. The constraints of conventional approaches are mentioned, which are addressed by (Stauffer & Sakai, 1968) through formulating a transfer function for derivative spectroscopy. Both studies emphasize the significance of grasping the mathematical foundations to enhance the spectral analysis. The instrumental aspects of spectroscopy are investigated by (Pemsler, 1957), emphasizing the design and operation of spectrometers in detail. Comparing various spectrometer designs shows how progress in instrumentation can enhance the performance of derivative spectroscopy.

To address the constraints of spectroscopic approaches, focusing on the first and second order of derivative for the absorption spectra (Smith, 1963) can enhance the resolution. Furthermore, (Bonfiglioli & Brovetto, 1964) show the mathematical calculations emphasizing the dependence of spectroscopic performance on the main design parameters to manage noise impact and enhance SNR.

More recent research (Karpinska, 2004) offers an overview of the application and progress of derivative spectrophotometry (DS). It covers a range of fields, such as pharmaceutical research and inorganic analysis. The research highlights the application of spectrophotometry in pharmaceutical analysis due to its effectiveness in identifying the primary components of

drugs, even when accompanied by additional ingredients. Specifically, second-order derivative spectrophotometry is utilized to concurrently detect different elements in medicinal and food samples. While mentioning the benefits, it discusses the drawbacks to consider, such as challenges with reproducibility and the dependence of results on instrumental parameters such as scan speed. The lack of robustness in the techniques and the absence of optimization protocols must be overcome to improve the techniques' credibility. (Jiang et al., 2000) present a novel differential time-domain spectroscopy (DTDS) to explore a method for measuring the dielectric constant of thin films in the GHz to THz range– a technique essential for contemporary semiconductor applications. Their solution provides better performance in terms of noise reduction and SNR enhancement compared with traditional TDS approaches.

There are some methods of achieving the time domain derivative spectroscopy in the THz domain, such as using metallic transmission grating (Filin et al., 2001), ring resonators (Xie et al., 2020), and MEMS (Amirkhan et al., 2021).

A novel approach to the differentiation of light waves is introduced by (Filin et al., 2001) through metallic transmission gratings, which provide the first order of derivative of the waveform by subwavelength period gratings based on diffraction principles that make it scale-independent and can be extended beyond THz frequencies. In another method, high-quality factor on-chip silicon ring resonators are designed by (Xie et al., 2020) for the temporal first-order derivative of the lower THz frequencies supported by design and experimental results. This research is introduced as an approach to manipulating and re-shaping the THz pulse with communication and data processing applications. Recently, (Amirkhan et al., 2021) developed a THz time-domain derivative spectrometer that provides information for up to 4 orders of derivatives with the capability to enhance SNR. The shortcoming of their work is in the recovery of lower frequencies.

The above references pinpoint the approaches, advantages, applications, and importance of time-domain derivative spectroscopy. The modulation of the THz beam will be discussed in the next section.

1.5 Terahertz beam modulation

The derivative function can be utilized to manipulate the THz beam for various purposes and applications. This involves modifying parameters such as amplitude, phase, polarization, or spatial distribution. Different methods are available to modulate the THz beam. In one such method, a spatial light modulator such as a digital micromirror device (DMD) can be incorporated to shape the THz beam profile for imaging applications (Zanotto, 2022). Modulation methods can potentially improve the performance of THz-TDS systems or introduce measurement methods. By incorporating THz beam modulation into the THz-TDS setup, further control over the THz radiation can be gained.

The utilization of THz wave manipulation can be extended beyond THz-TDS, for instance, in advanced signal processing within THz communication systems, as discussed by (Balistreri et al., 2021). Their research highlights the importance of incorporating a tapered two-wire waveguide (TTWWG). The TTWWG reshaped an input THz pulse into its first-order time integral waveform by propagating toward the subwavelength output. The findings of this research lead to the realization of a THz time integrator device, tackling problems of broadband THz pulses.

Moreover, the THz beam path can be modulated using MEMS devices, which can make controlled alterations to the THz signal path (Amirkhan, Robichaud, et al., 2020). The following section will explore how MEMS technology can be harnessed to manipulate THz beams for various applications. More concisely, in this research, following the steps taken by (Amirkhan et al., 2021; Amirkhan, Robichaud, et al., 2020), I benefit from MEMS utilization in the THz beam path as a differentiator to manipulate the THz pulse. The up-and-down movement of MEMS and its metallic surface act as a moving mirror in the THz signal path by causing a delay in the time/path of the THz signal, thus differentiating the signal and obtaining THz-TDDS functionality.

1.6 MEMS in THz systems

Microelectromechanical systems are miniaturized devices that integrate mechanical and electrical components on a single chip. MEMS usually consist of sensors, actuators, and control circuitry to precisely manage and control physical phenomena at micro or nano scales (Mahalik, 2008). MEMS has become a technology that provides efficient and low-cost components for incorporation into RF and microwave systems (Dubuc et al., 2004) and even THz systems (Oberhammer, 2018).

MEMS technology can be integrated into THz-based technologies. For instance, THz detectors based on MEMS resonators provide better response times and increased sensitivity compared to traditional thermal sensors (C. Li et al., 2023). Furthermore, a MEMS converter can utilize metasurface structures to achieve THz to infrared (IR) band conversion based on absorption and emission selective control for THz imaging applications (Alves et al., 2018). MEMS tuner technology allows for realizing THz quantum cascade lasers (THz QCLa) for reproducible and robust tunable coherent THz source applications (Han et al., 2014). Combining MEMS with THZ metamaterials brings benefits in terms of performance and manufacturability that are essential for the progress of THz technologies (Pitchappa et al., 2021). The adjustability of MEMS devices supports the progress of cutting-edge THz communication systems that enable advanced 6th-generation communication (Xu et al., 2022).

MEMS reflectors (Figure 1.4) are designed to steer THz beams and dynamically control the direction of THz waves in a reflect array (Schmittf et al., 2021). Furthermore, MEMS biomaterial sensors operating in THz frequencies coupled with metamaterial absorbers have demonstrated close to total absorption of particular THz frequencies. This research paves the way for highly sensitive functionality for THz imaging applications (Alves et al., 2012). By improving the resonant absorption, MEMS devices can improve the sensitivity for real-time THz imaging systems (Alves et al., 2014).

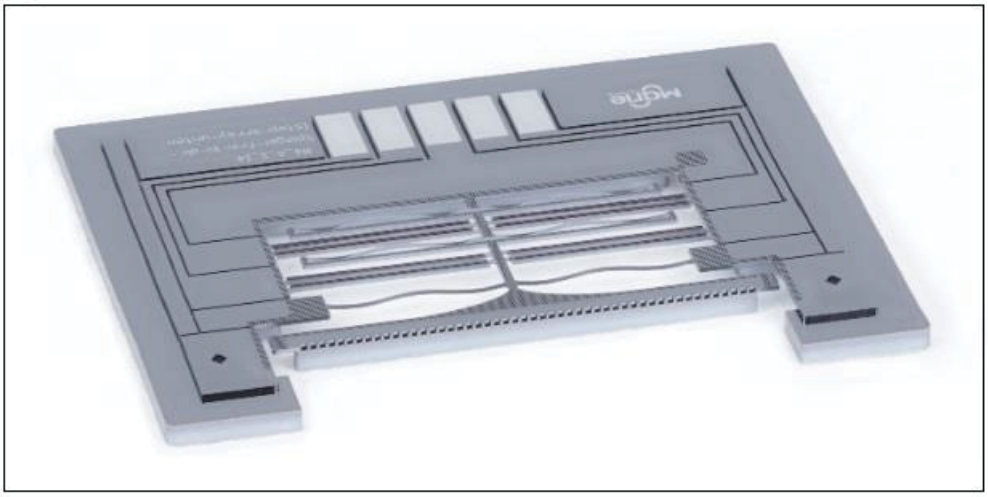

Figure 1.4 A designed and fabricated stack of reflector system
Taken from (Schmitt et al., 2021)

1.6.1 MEMS drawbacks

The most prominent drawback of integrating MEMS in the THz system observed during this research is the jitter and derived phase noise. This problem can be tackled by custom-designing the MEMS. However, this research aimed at utilizing a commercial MEMS, which, compared to previous research by (Amirkhan, Robichaud, et al., 2020), has higher movement inaccuracy, thus higher jitter, and lower SNR. In the next section, jitter will be introduced, and the impact of jitter on THz spectroscopy will be discussed in more detail.

1.7 Jitters, MEMS, and THz system

To fully comprehend the effects of jitter in THz spectroscopy, it is essential to grasp the essence of jitter in signals beyond its applications.

1.7.1 Introduction to jitter

Jitter typically indicates the slight, relatively fast variations in timing or amplitude of a signal with respect to the ideal signal. This can introduce some uncertainty over the position or value of the signal. Figure 1.5 illustrates a signal with jitter (without noise) compared with its ideal

signal. The dashed line represents the ideal signal, while the solid line depicts the signal with jitter (Anthonys, 2022).

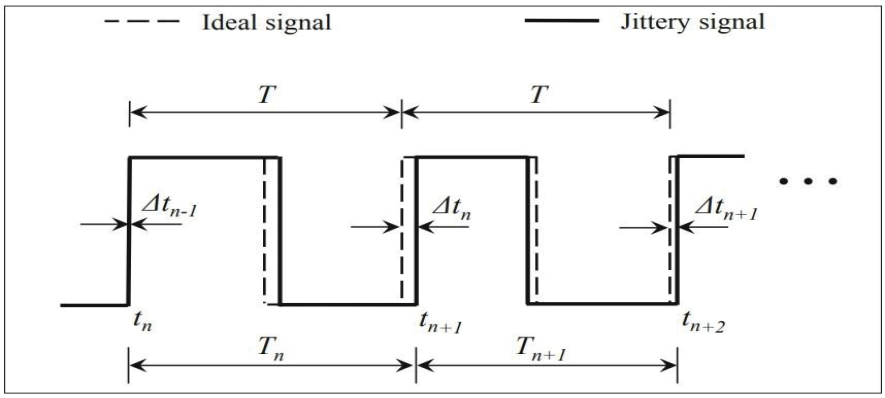

Figure 1.5 Clock-like signal with jitter compared to an ideal signal
Taken from (Anthonys, 2022)

There are different types of jitter, including period, time interval error, cycle-to-cycle, and phase jitter. A brief description about them are presented here.

Period Jitter (PRD): j_n^{PRD} is the difference in time between the measured and the theoretical ideal clock cycle periods. It is challenging to measure the ideal clock cycle precisely; hence, utilizing the average period is advised for practical purposes. Calculating the average period jitter for the *n*th cycle involves considering the period of the ideal signal *T* (Anthonys, 2022, p.56):

$$j_n^{PRD} = T_n - T = t_{n+1} - t_n - T \tag{1.3}$$

Where j_n^{PRD} represents the period jitter of the *n*th cycle, *n* is the index, and T_n is the nth signal cycle.

The time interval error jitter (TIE): TIE refers to the discrepancy between the clock edge time of an idea and jittery signals for every active clock edge that occurs (whether it is a rising or falling edge). The difference between the timing of the *n*th signal event t_n and its ideal presence in time denoted as $\Delta t_n = j_n^{TIE}$ is described as (Anthonys, 2022, p.57):

$$j_n^{TIE} = \Delta t_n = T_n + \Delta t_{n-1} - T = t_{n+1} - t_n + \Delta t_{n-1} - T \tag{1.4}$$

where Δt_{n-1} represents the discrepancy in the signal (n-1)th timing event tn-1 .

Cycle-to-cycle jitter (CtoC): It refers to the time variance between consecutive clock periods. It is primarily utilized to assess the functionality of a phase-locked loop (PLL). This measurement technique focuses on PLL clock recovery dynamics rather than long-term frequency variations. The cycle-to-cycle jitter, for the nth cycle, denoted as j_n^{CtoC}, is determined using the formula (where |.| is the absolute value) (Anthonys, 2022, p.57):

$$\begin{aligned} j_n^{CtoC} &= |T_{n+1} - T_n| = |t_{n+2} - t_{n+1} - (t_{n+1} - t_n)| \\ &= |t_{n+2} - 2t_{n+1} + t_n| \end{aligned} \tag{1.5}$$

Phase Jitter: With a non-standard approach, phase jitter can be modeled by a phase-modulated sine wave, including a phase noise $\theta(t)$ (Anthonys, 2022, p.58):

$$s(t) = \sin\big(2\pi f t + \theta(t)\big) = \sin\left(2\pi f\left(t + \frac{\theta(t)}{2\pi f}\right)\right) \tag{1.6}$$

Therefore, the phase jitter is formulated as (Anthonys, 2022, p.58)

$$j^{PHS} = \frac{\theta(t)}{2\pi f} \tag{1.7}$$

Based on the formulation provided above, it is evident that a mutual impact and correlation exists between jitter, phase noise ($\theta(t)$), and phase jitter for frequency *f*.

There are two main types of jitter: random (referred to as RJ) or non-deterministic and deterministic jitter, as presented in Figure 1.6. The jitters explained above are deterministic.

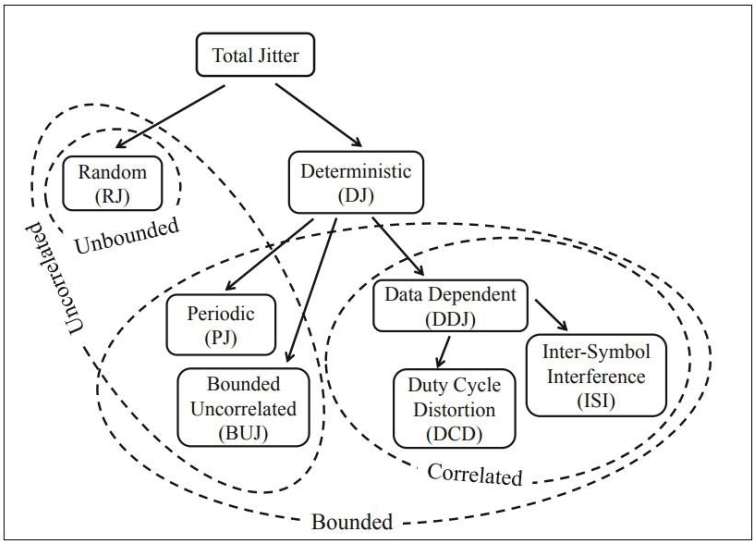

Figure 1.6 Jitter categorization
Taken from (Anthonys, 2022, p.59)

The deterministic jitter is due to known processes and is linearly additive with a predictable function. It can be defined by its peak-to-peak value. Various types of deterministic jitter include bounded uncorrelated (BUJ), periodic (PJ), data-dependent (DDJ), including duty cycle distortion (DCD), and jitter symbol interference (ISI). For the conciseness of this thesis, only random jitter will be discussed, as I hypothesize that the jitter caused by MEMS is random and not deterministic. Deterministic jitter is often observed in digital signal processes.

The random jitter is commonly caused by one of the different types of noise, like flicker noise (also known as $1/f$ noise), shot noise, or thermal noise, among other high-order noise types. It usually follows a Gaussian distribution and can be described through a probability density function (PDF):

$$f_{RJ}(\Delta t) = \frac{1}{\sigma_{RJ}\sqrt{2\pi}}\ exp\left\{-\frac{1}{2}\left(\frac{\Delta t - \mu_{RJ}}{\sigma_{RJ}}\right)^2\right\} \tag{1.8}$$

Here, the parameters μ_{RJ} and ${\sigma_{RJ}}^2$ represent the mean and variance of the random jitter, respectively. The jitter can be described by either its RMS value or standard deviation (STD)

with time $\epsilon(t)$ as the random process over time with the PDF of $f_{RJ}(\Delta t)$ as follows (Anthonys, 2022, p.59):

$$\Delta t^{RJ}(t) = \epsilon(t) \quad (1.9)$$

Additionally, other types of higher-order random jitter processes are characterized by a typical form of $f^{-\alpha}$. This is considered unbounded, as the PDF does not reach zero unless the jitter Δt approaches infinity. When $\alpha = 0$, it represents Gaussian or white jitter; if $\alpha = 1$, it signifies flick. If $\alpha = 2$, it denotes integrated white jitter (Anthonys, 2022; Da Dalt & Sheikholeslami, 2018).

1.7.2 MEMS jitter sources

In the field of MEMS, jitter can root from a variety of sources, such as:

Thermal Noise: Temperature fluctuations can affect the mechanical characteristics of MEMS devices and lead to time variations (Da Dalt & Sheikholeslami, 2018).

Mechanical noise: The stability of MEMS components can be disturbed by external vibrations, leading to timing inaccuracies (Mahdavi et al., 2015).

Electrical Noise: Fluctuations in the power supply or substrate or interferences from other electronic devices may lead to electrical noise (C. W. Zhang & Forbes, 2003).

Process Variations: Jitter can be caused by performance variations due to fabrication inconsistencies in MEMS (Y. Huang et al., 2012).

Phase Noise: It refers to the instabilities in the oscillation frequency of the device. These fluctuations can be affected by factors like vibrations or electromagnetic interference (Mahdavi et al., 2015).

1.7.3 Impact of MEMS jitter on THz signals

As will be explained in Chapter 2, a lock-in amplifier is a critical part of THz pulse detection. It helps to find the signal in a noisy background and filter the noise, and the resultant output DC signal in the time domain is the THz signal of interest. In order to benefit from the functionality of the lock-in amplifier (refer to Chapter 2, section 2.3), a reference signal is needed to lock into it, and the measured signal will be compared with it to be in phase with reference and filter out the noise. When the THz emitter modulates the THz beam, the lock-in amplifier latches onto this modulation frequency. In the case of using an external modulating segment (typically a chopper, but in the case of this research, MEMS acts as the modulator) to modulate the THz beam path, the lock-in will latch on the oscillating frequency of the MEMS. If MEMS has any inaccuracies, such as jitter and phase noise, the lock-in reference will be faulty, thus impacting the integrity and quality of the detected measured signal. Therefore, it is essential to recognize the MEMS jitter and phase noise to understand how it affects the detected THz signal in THz-TDS. The main effects can be named as:

Phase Noise: Jitter may cause phase shifts in the THz signal and can result in inaccuracies when measuring the optical properties of materials. The phase noise can distort the temporal profile of the THz pulse, which complicates the determination of material characteristics (Duvillaret et al., 2000). Furthermore, the mechanical vibrations generate phase noise during THz electric field measurements. This interference could create uncertainties in the THz signal detection, especially when the electric field strength is sufficient to induce substantial phase changes, thus leading to SNR degradation (Sharma et al., 2013).

Amplitude Fluctuations: THz signal amplitude variations caused by jitter can decrease SNR and can obstruct the characterization of materials by obscuring the true signal (Duvillaret et al., 2000).

1.7.4 MEMS jitter reduction techniques

To enhance the SNR in THz spectroscopy, various methods can be utilized to decrease the MEMS jitter:

Temperature Control: Maintaining temperature settings and reconfigurability (Pitchappa et al., 2021) is crucial for controlling thermal noise and minimizing jitter effects (Da Dalt & Sheikholeslami, 2018).

Power Supply Filtering: Opting for high-quality power supplies with filtering can help minimize electrical interference that often leads to jitter issues.

Optimized Design: Creating MEMS devices with lower motional resistance, increasing quality factors, and using materials and geometries that are less prone to process variations can effectively reduce jitter issues (Mahdavi et al., 2015).

Signal Processing Techniques: Cutting-edge methods in software algorithms can be utilized to mitigate distortions caused by jitter and improve the SNR of THz spectroscopic measurements (Nakagawa et al., 2023).

For THz imaging applications where an array of MEMS can be utilized, the potential crosstalk between each MEMS pixel can cause deterministic jitter. This crosstalk results from accidentally coupling the magnetic or electric field with the neighbor conductor carrying a signal (Béliveau, 2022). This unwanted component will be added to the reference signal, and its bias will vary, which can be determined by the interference signal power (Da Dalt & Sheikholeslami, 2018).

In the following chapters, I will analyze the jitter for the MEMS and present the data. The MATLAB script used to calculate the jitter is presented in Annex IV.

1.7.5 Disadvantages and limitations of MEMS in THz

Besides the advantages of using MEMS in THz spectroscopy, the current developments face some challenges. Integrating low-frequency electronics, such as lock-in amplifiers, in the THz detection process can be an advantage in spectroscopic applications. Although the primary function of a lock-in amplifier is to detect a weak signal with a noisy background (Kloos, 2018), the signal needs minimum requirements to be detected. Furthermore, a lock-in amplifier requires a periodic reference to lock on its frequency, multiply it with the signal to be detected, passing the periodic oscillation of MEMS, provide the reference frequency for lock-in to detect the signal through a low-pass filter, and then the signal can be detected (Kloos, 2018). The oscillatory behavior of a MEMS (which acts like an oscillating mirror) provides that reference frequency for the lock-in. The detection will be challenging if this oscillation amplitude is in the nm scale or if the oscillation frequency is in the MHz range (Amirkhan, Robichaud, et al., 2020). Thus, designing or selecting a suitable MEMS is necessary. If the MEMS has complex movements (Amirkhan, Robichaud, et al., 2020), the signal recovery in lower frequencies will be difficult. Furthermore, suppose an array of MEMS is utilized to modulate the THz beam. In that case, the array shall function without cross-talk between each pixel in the array. Otherwise, the detection and signal recovery will not be straightforward (Amirkhan, Robichaud, et al., 2020). However, the technical aspects of designing such an array of MEMS need special considerations such as avoiding crosstalk, programming each pixel separately, and controlling it to create pixelated light patterns, size optimization, fabrication, and integration, to name a few. Another critical point is the reproducibility of the project. Both (Amirkhan, Robichaud, et al., 2020; Amirkhan et al., 2021) are uniquely custom-designed MEMS that are not accessible publicly. Thus, selecting a commercial MEMS with desirable performance, uniform movement, and high quality factor is recommended.

1.8 Conclusion

In this chapter, I conducted a literature review on the relevant topics. Different topics, such as THz technology, time-domain spectroscopy, derivative functionality, MEMS, and their applications in the THz field, were presented. Knowing the gaps and drawbacks, I propose

implementing MEMS as a THz beam modulator. This will convert a conventional THz-TDS to THz-TDDS with better performance. Learning from previous research in this specific field (Amirkhan, Robichaud, et al., 2020; Amirkhan et al., 2021), and in order to have better control over the amplitude and resonance frequency of the MEMS, jitter control, and reproducibility, I propose utilizing a commercially available piezoelectric device. This will expand the accessibility of MEMS in THz technology and diversify the applications.

The commercial piezoelectric MEMS speaker will be presented and characterized in the next chapter. Then, I will use this speaker to modulate the THz beam and verify the functionality of this novel THz-TDDS by obtaining the optical parameters of four materials. The results are validated by conducting the same measurement using a commercial setup (Toptica TeraFlash Pro) and available literature. The steps, methodology, and results are presented in Chapter 2. An extensive discussion of jitter, phase noise, and SNR is provided in Chapter 3. Finally, the discussion and potential improvements will be presented in Conclusions and Recommendations.

CHAPTER 2

METHODOLOGY AND RESULTS

2.1 Introduction

In this chapter, I will present the THz setup, lock-in function, and piezoelectric MEMS Speaker to lay the fundamentals for THz-TDDS setup and functionality by studying four materials (glucose, lactose, maltose, and fructose). Using the measured time-domain data and employing the Fast Fourier Transform (FFT), the optical parameters of these materials will be calculated. The results are weighed against a commercial THz-TDS tool (TeraFlash pro from Toptica) and available literature to verify the functionality of the THz-TDDS. This is in continuation to the research conducted by (Amirkhan et al., 2021) and (Béliveau, 2022).

2.2 Modulating device

As mentioned in Chapter 1, using MEMS as a differentiator in the path of the THz beam can convert the THz-TDS to THz-TDDS setup (Amirkhan et al., 2021), as seen in Figure 2.1. This figure presents the array of piezoelectric micromachined ultrasonic transducers (PMUT). Although this differentiator could obtain the first-order derivative of the THz beam with 4 THz bandwidth, there were measurement difficulties. Challenges of this project were the low oscillation amplitude (±500 nm) and high oscillation frequency (1.38 MHz), which made the detection by lock-in amplifier difficult. Crosstalk between each cell made the array control more complicated, and only 3.4% of the THz beam size was covered by PMUT's entire active area. The sensitivity and detection process was improved by integrating a piezoelectric micromachined (PM) device, as shown in Figure 2.2.

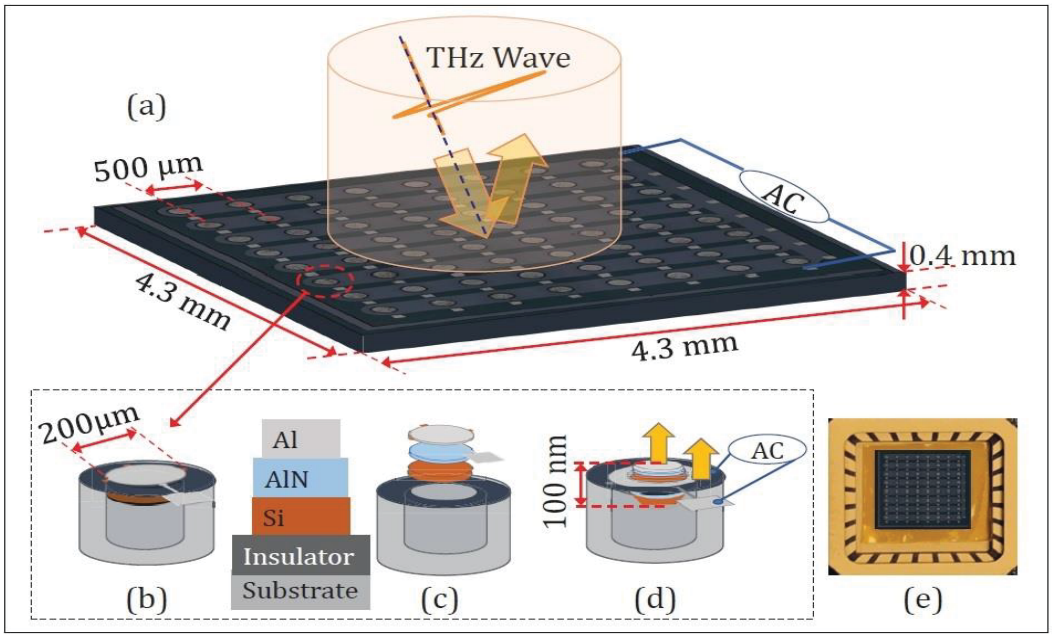

Figure 2.1 (a) PMUT array, (b) unit cell, (c) constituent materials and layers, (d) oscillatory response to triggering voltage, and (e) the array installed on a gold leadless chip carrier (LCC) package to be utilized in THz setup
Taken from(Amirkhan, Robichaud, et al., 2020)

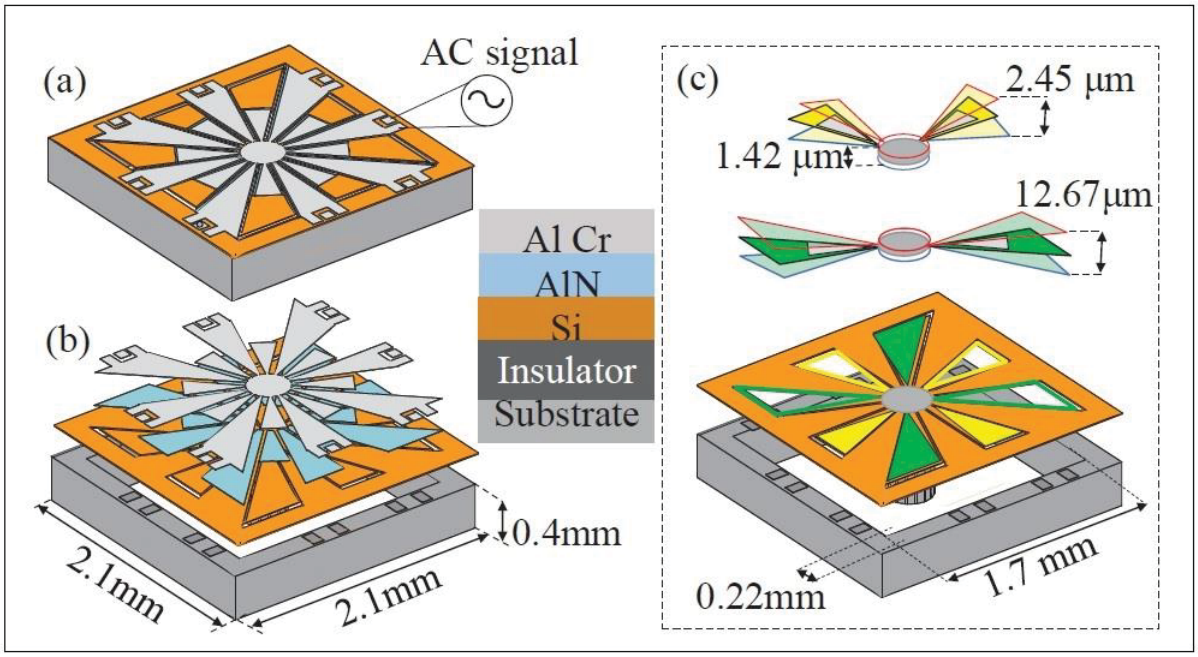

Figure 2.2 (a) PM device, (b) showing various layers and composing materials, (c) the exploded design of different areas and their motion amplitudes
Taken from (Amirkhan, 2021)

This improved design provided up to four orders of signal derivatives with a maximum 12.67 µm oscillation at 10.82 kHz. Although this PM achieved considerable results, it did not recover the signal in lower frequencies (lower than 0.8 THz) due to the complex movement of the PM. Thus, using a MEMS with 2D uniform movement is recommended.

Considering the challenges in previous work, as mentioned earlier, the integration of a MEMS with uniform movement, kHz oscillation frequency, and µm oscillation amplitude is envisioned. Thus, a piezoelectric MEMS Speaker (APS2509S-T-R) (Mouser Electronics, 2024) as a modulating device (MD) is proposed for this research. This MD, as shown in Figure 2.3, has a total surface area of 234 mm^2 (13 mm × 18 mm), a maximum total displacement of 16 µm at 1.1 kHz when excited with a sinusoidal signal, and peak-to-peak voltage of 20 V. From the point of view of the THz beam, the MD acts as a mirror with uniform movement. The mode-shape of the MD, obtained by Vibrometer, can be seen in Figure 2.4 (a) up and (b) down, emphasizing the uniform movement of this MEMS.

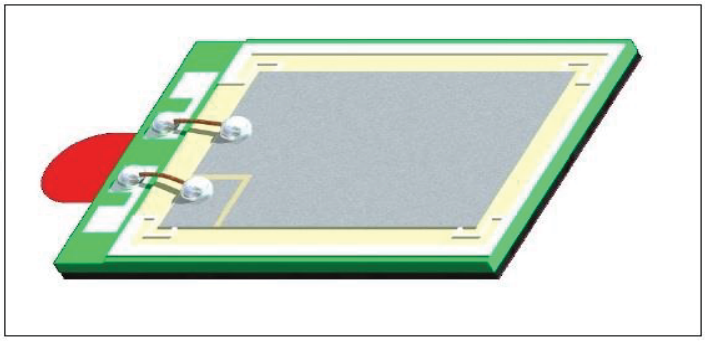

Figure 2.3 Piezo MEMS speaker as modulating device
Taken from (Mouser Electronics, 2024)

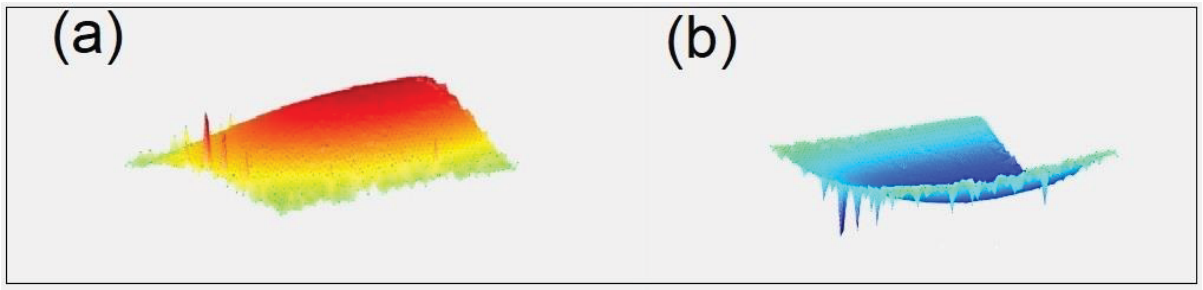

Figure 2.4 (a) Up and (b) down mode-shape showing the uniform movement of MD

As a speaker, this MD can oscillate in a broad frequency range of 200 Hz to 20 kHz. Based on Vibrometer analysis, the highest oscillation amplitudes can be obtained at 1.1, 3, and 10 kHz. Therefore, these frequencies were examined in the THz-TDS setup to investigate if any of these frequencies can provide the derivative functionality. Before explaining the THz-TDS setup, the functionality of the lock-in amplifier will be explained in the next section, and this explanation will be used to understand how THz-TDS collects data.

2.3 Lock-in amplifier

A lock-in amplifier (LIA) can detect and amplify weak signals with a noisy background at a specific periodic reference frequency to improve the signal-to-noise ratio. It comprises a multiplier, a low-pass filter (LPF), or an integrator (to block the AC part) with its center frequency on the reference frequency and a phase shifter. In the next step, the LIA will average the detector's reading by locking on a known reference frequency (in typical applications, this is the chopper frequency). The output voltage is the DC part without noise, proportional to the amplitude of the input signal (detected signal) and the cosine of its phase (Kloos, 2018). Figure 2.5 presents the internal configuration of a lock-in amplifier (*The Lock-In Amplifier: Noise Reduction and Phase Sensitive Detection*, n.d.).

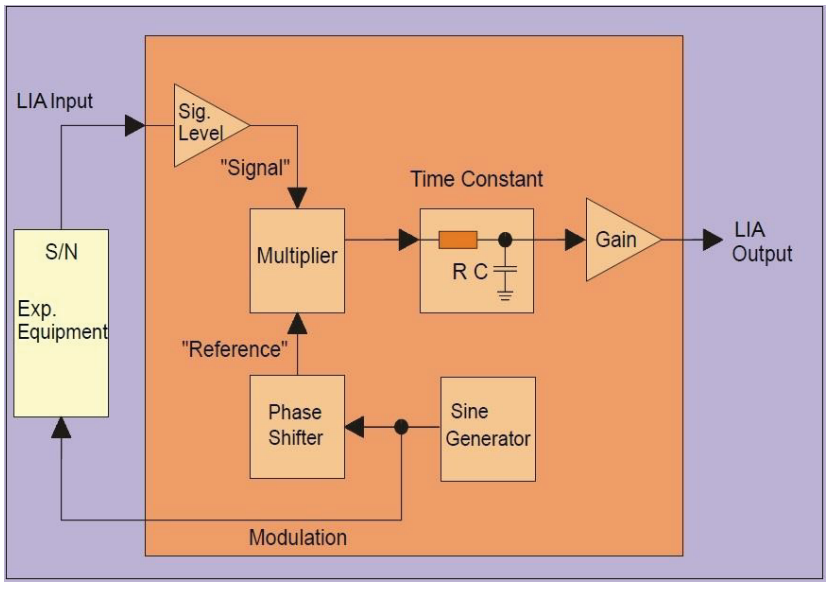

Figure 2.5 The internal structure of a lock-in amplifier
Taken from (*The Lock-In Amplifier: Noise Reduction and Phase Sensitive Detection*, n.d.)

The frequency of the low-pass filter, or inversely its period τ, will be determined as a function of the acquisition time at each position of the delay line movement. To obtain a stable reading from the amplifier, the integration time constant τ must be at least three times less than the time between each movement of the delay line to allow the acquisition capacitor (in the resistor-capacitor (RC) filter) to charge and avoid broadening the sharp features of the THz wave (Neu & Schmuttenmaer, 2018). Lock-in amplifier has the capability to detect higher orders of derivative directly, which made the research by (Amirkhan et al., 2021) possible, as four orders of derivative were detected in their measurements.

2.4 Derivative functionality of THz setup

To test the feasibility of differentiating the THz signal with such an MD, a pump-probe THz-TDS system using a PCA as emitter (TeraVil Ltd.) and Batop bowtie PCA (bPCA-100-05-10-800) as the detector has been designed as shown in Figure 2.6. The Chameleon Discovery NX with total power control (TPC) femtosecond Ytterbium (Yb) oscillator laser (Coherent Inc.) pumps both emitter (Tx) and detector (Rx) PCAs with a tunable output of 800 nm laser pulse, 100 fs pulse duration at 80 MHz repetition rate, average power of 10 mW for both emitter and detector.

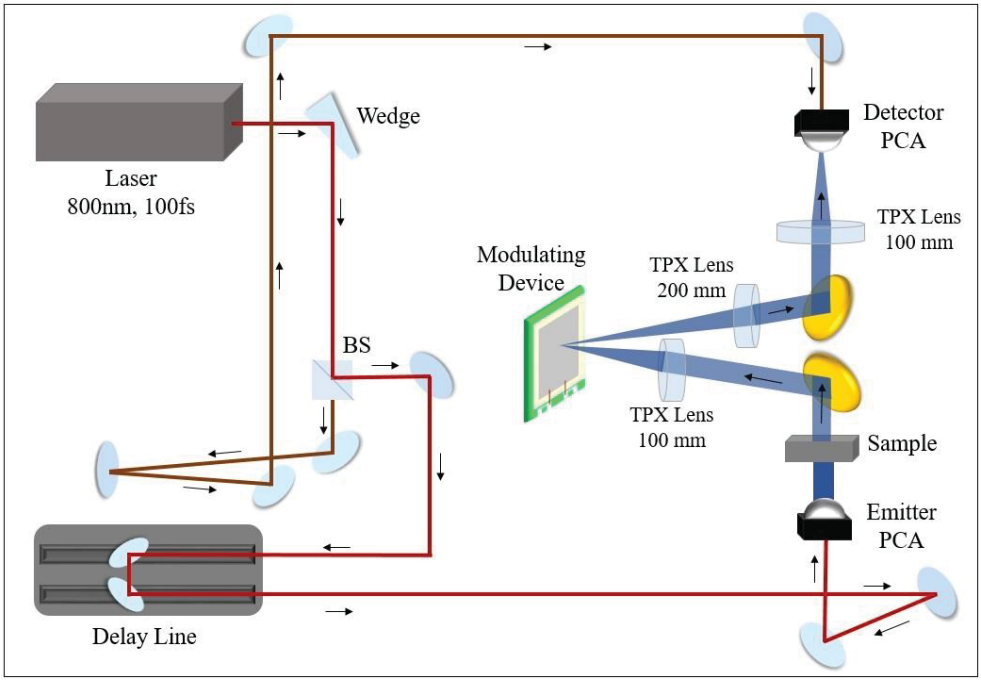

Figure 2.6 THz-TDS pump-probe configuration

Figure 2.7 shows the THz path emphasizing the LIA functionality to detect the reference and modulated signals. Here, the sample is removed only to detect the THz pulse without doing spectroscopy.

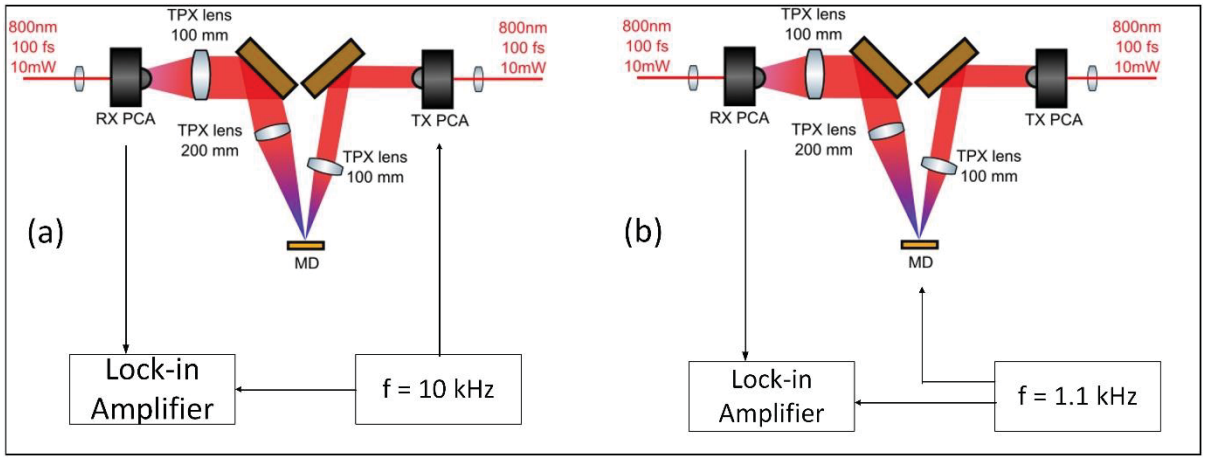

Figure 2.7 THz-TDS experimental setup, (a) when the LIA locks on the emitter's modulation frequency (MD is off and the reference signal is measured), and (b) when the LIA locks on the MD's oscillation frequency (MD is on and the derivative signal is obtained)

Figure 2.7 presents the reflective geometry of the experimental setup. The gold-coated flat mirror and a TPX (Polymethylpentene) lens direct and focus the THz beam on the MD. The

MD is precisely at the focal point of the TPX lens, and the angle of incidence on the MD is approximately 10 degrees deviated from being perpendicular. Another TPX lens collimates the reflected THz signal and is then reflected by the second gold-coated flat mirror, and the third TPX lens with a focal length of 100 mm focuses the beam on the 5 μm gap distance of the Batop PCA. The hemispherical silicon lens of Batop is placed 75mm away from the focal point of the third TPX lens. The lock-in amplifier from Zurich Instruments detects the signal.

This lock-in will latch on the PCA Tx modulation frequency with a repetition frequency of 10 kHz and biased with 40v to give us the reference signal when the MD is not excited and is at rest mode, thus acting like a fixed mirror (Figure 2.7(a)). When the emitter is not modulating and by exciting the MD at its resonance frequency (1.1 kHz), the lock-in will latch on this frequency to obtain the derivative signal (Figure 2.7(b)).

The supplying voltage and the oscillation frequency of the MD affect its oscillation amplitude and, thus, provide proportional amplitude changes of the detected THz derivative signal. The frequency response of the MD is not flat; hence, the amplitude of the oscillation of the MD will vary based on the frequency of operation. To find the correct resonance frequency, based on the measurements by the Vibrometer, as mentioned earlier, frequencies of 1.1, 3, and 10 kHz are tested. The results are shown in Figure 2.8 for the time domain (a), zoomed-in (b), and frequency domain (c).

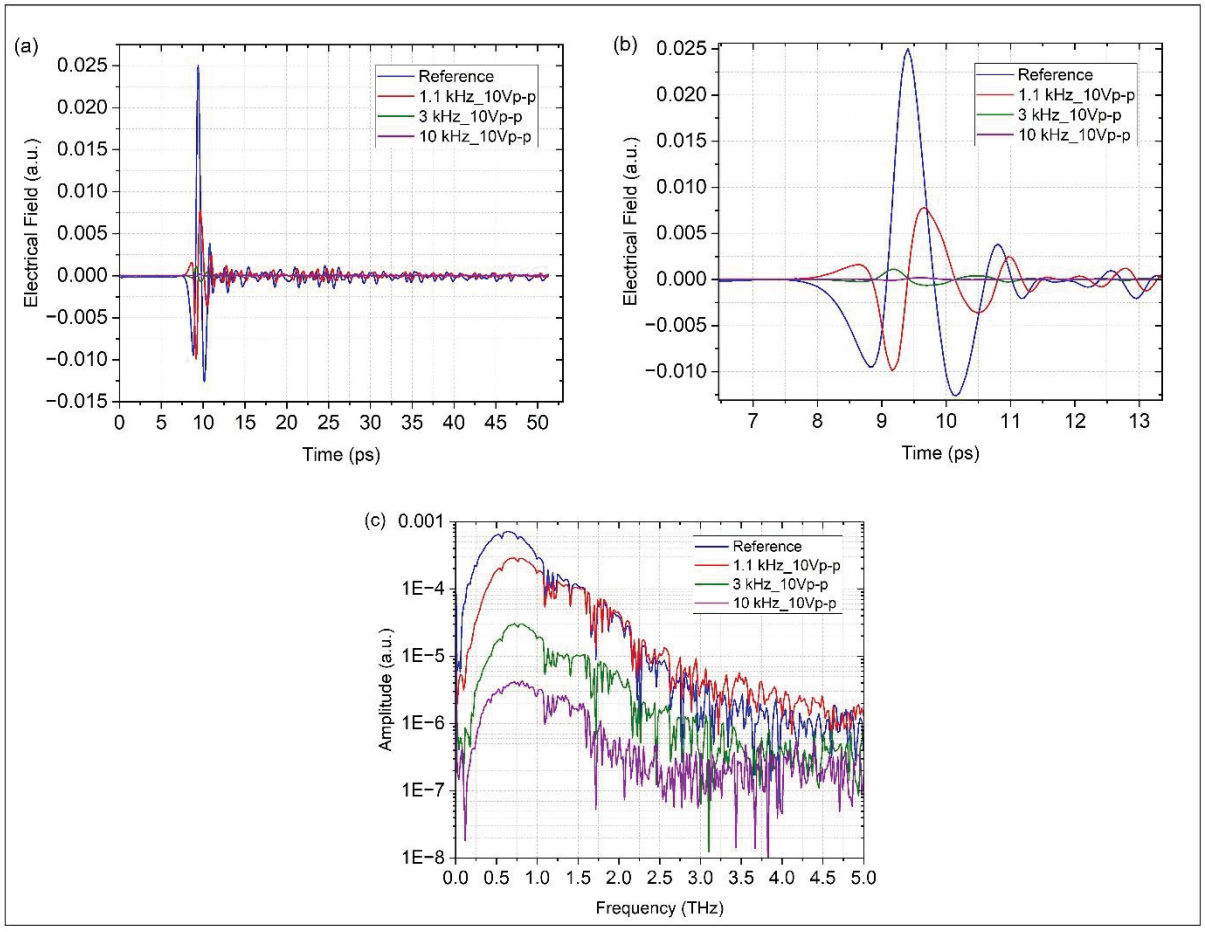

Figure 2.8 Oscillation frequency selection based on derivative functionality (a) in the time domain, (b) zoomed-in to show the derivative, and (c) their spectra

As shown in Figure 2.8 (b) in the time domain, the inflection points of the reference signal correspond to the maxima (minima) of the MD signal at 1.1 kHz. Thus, this frequency is chosen for the THz-TDDS that provides the derivative response.

Besides the resonance frequency, the amplitude selection is also essential. The piezo speaker has the capability to be supplied by up to 30 V_{p-p}. Due to limitations in the function generator device available in the lab, the amplitude of up to 20 V_{p-p} was tested. The results for various amplitude values can be seen in Figure 2.9.

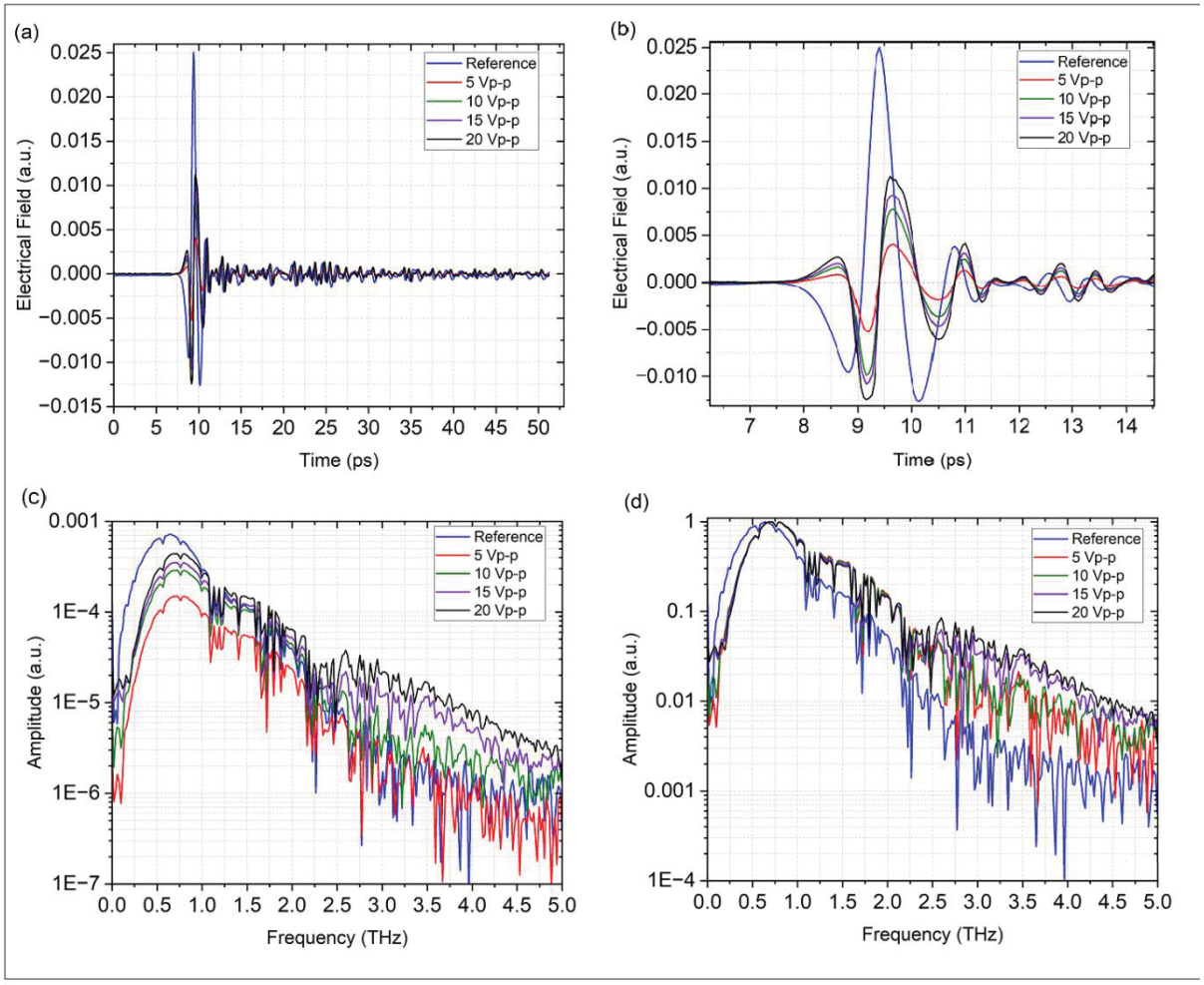

Figure 2.9 Amplitude comparison at 1.1 kHz oscillation frequency for (a) time-domain, (b) zoomed-in time domain, (c) amplitude spectra, and (d) normalized amplitude spectra

It is noteworthy that, as seen in Figures 2.9 (c-d), the SNR at $Vp{-}p$=20v has the lowest SNR but the highest amplitude in the time domain, making it easier to detect but challenging for optical parameter calculations. It is a trade-off, and other factors relevant to Nyquist theorem, should be considered for amplitude value selection.

Based on the THz detection requirements and the results presented in Figures 2.8 and 2.9, the differential functionality can be achieved with activation of MD at 1.1 kHz and 20 V_{p-p}voltage. This is according to the measurement results and to respect the Nyquist theorem (Coutaz et al., 2018, p.600) and maintain the THz signal's high-frequency components; therefore, the phase shift should be two times smaller than the sampling time. Thus, for an oscillation amplitude of

less than 16 µm, the spectral content from 0 to 3.5 THz would be the same as the reference signal; hence, the derivative functionality will not be obtained.

When the lock-in locks on the oscillation frequency of the MD, the detected THz signal equals the difference of the electric field from the shift caused by the path length time variation introduced by the peak-to-peak oscillation amplitude of the MD (Figure 2.10). The maximum displacement of MD at 1.1 kHz is 16 µm.

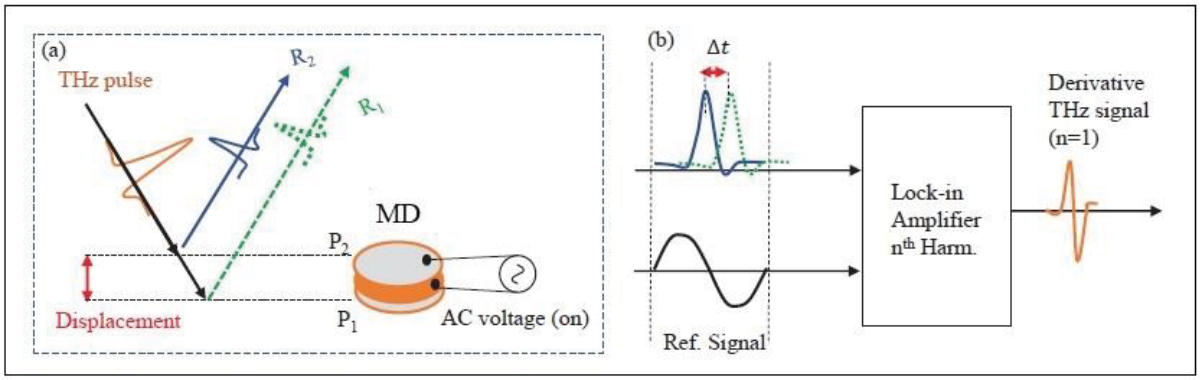

Figure 2.10 (a) The functional principle of MD in THz beam path and modulating the THz beam by up and down movement, (b) the way that LIA detects the modulated THz beam with the reference and detected signals
Taken from (Amirkhan, 2021)

Thus, the MD motion induces a differential signal response that causes variation in the THz electrical field ΔE, which can be mathematically expressed by the following formula, described as the electric field slope at a given time *t* (Amirkhan et al., 2021):

$$m = \lim_{t \to 0} m(t) = \lim_{t \to 0} \frac{f(t) - f(t_0)}{t - t_0} \approx \frac{\Delta E}{\Delta t} \tag{2.1}$$

Figure 2.11(a) presents the time domain THz pulse of the reference signal (blue) when MD is off and acts like a mirror and when the MD is activated and modulating the THz beam (derivative signal in red). Figure 2.11(b) is zoomed in to emphasize the derivative functionality.

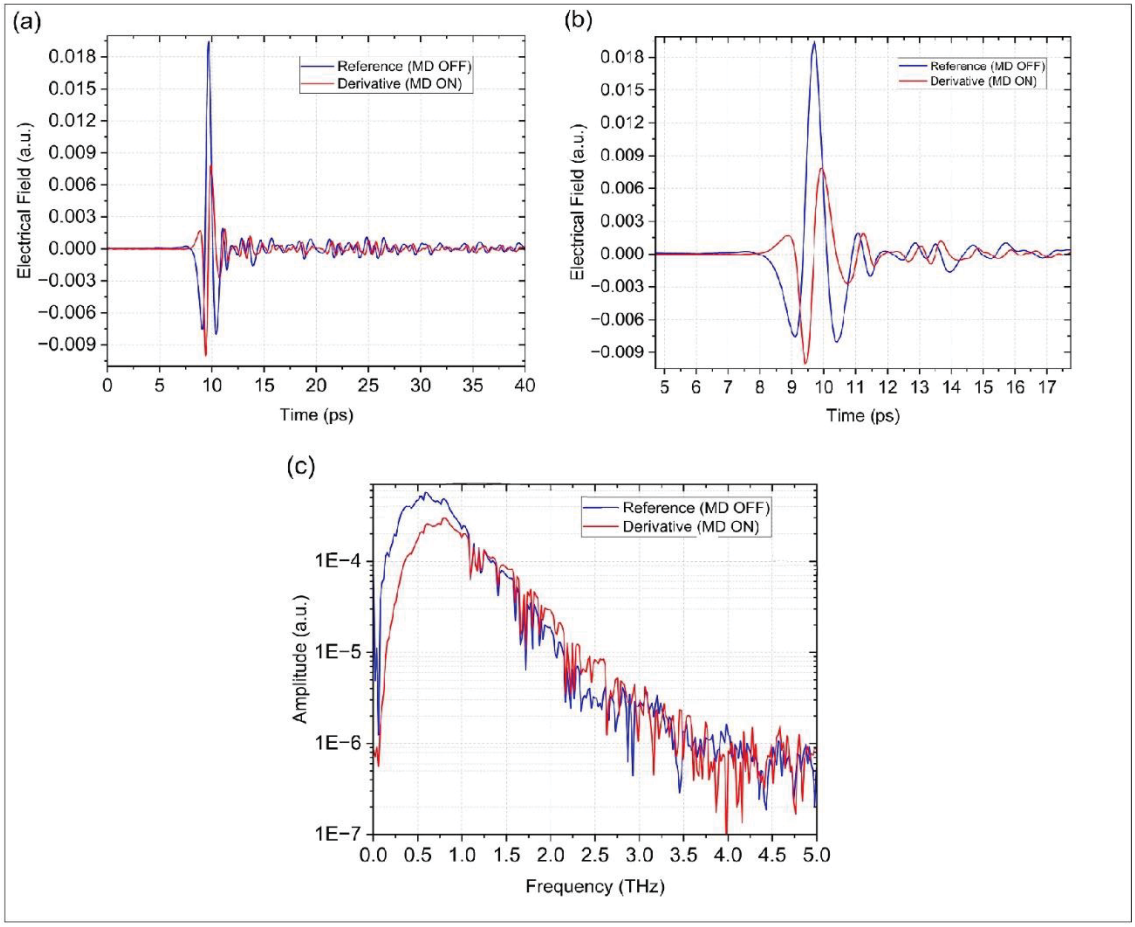

Figure 2.11 The detected signal in (a) the time domain and (b) the enlarged region to emphasize the derivative functionality, (c) spectra- The reference is in blue and derivative signal is in red

Figure 2.11(c) shows their respective spectra, with bandwidth from 0 to 3.5. The shift to higher frequencies in the spectrum of the derivative signal is visible, as expected by the derivative function. Furthermore, in the time-domain profile (Figure 2.11(b)), it can be observed that the maxima points of the reference signal (blue) correspond to the inflection points of the detected signal (red), which corresponds to the first-order derivative of the reference, and can be proven mathematically, as shown in Figure 2.12.

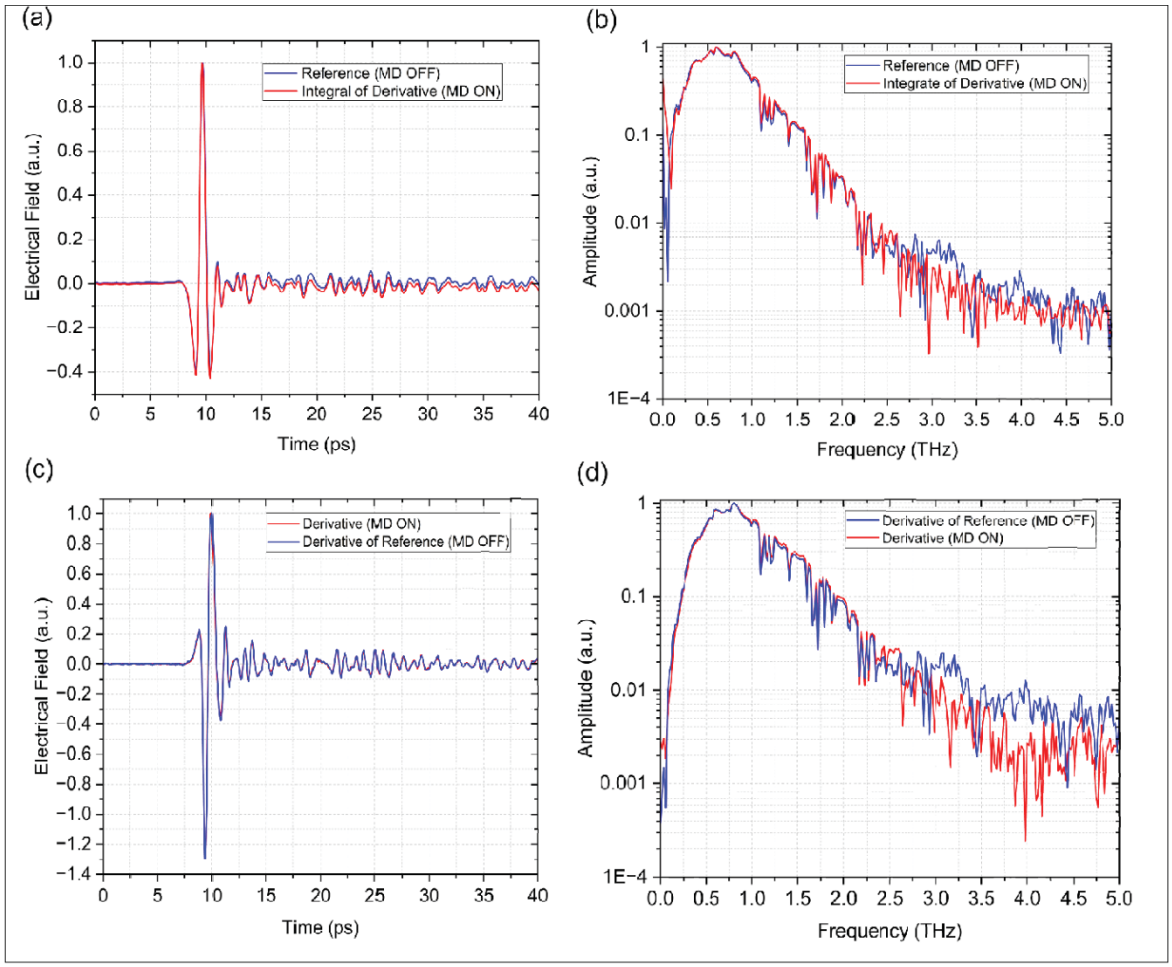

Figure 2.12 Time domain electrical field of the (a) calculated derivative signal and reference, (b) their spectra, (c) differentiated reference signal and derivative signal, and (d) their spectra in the frequency domain

In Figure 2.12, the normalized time domain and FFT results are obtained from the measurement results, and the measured data is compared with the mathematical calculation of derivative and integral functions to recover the signal. As Figure 2.12(a) presents, taking the derivative signal's integral corresponds to the reference signal. The same applies to applying the differentiation function on the reference, which matches the measured derivative signal in Figure 2.12(c). This is valid for both the time domain and frequency domain of the measured data (Figure 2.12(b) and (d)). In Figure 2.12(b) and (d), the poor agreement of results below 100 GHz and mismatch after 2.5 THz are observed, which hints that the system cannot resolve very low or very high frequencies. The comparison between the measurement and the

mathematical calculation (differentiation/integration) proves that this setup with activated MD has derivative functionality and can be implemented as a THz-TDDS setup.

A similar process was followed by simulation using Lumerical Software. The results are presented in Annex I. The next step is to validate the spectroscopy functionality of the THz-TDDS setup by testing four different pellets: glucose, lactose, maltose, and fructose.

2.5 THz-TDDS setup

In order to verify the THz-TDDS setup functionality, four materials are placed in the setup and the optical parameters can be calculated by analyzing the measurement data. Then, the same measurements are performed with a commercial THz time-domain spectrometer (TeraFlash Pro from Toptica). In the THz-TDDS setup, a pellet of each sample is placed after the Tx PCA in the THz path, as shown in Figure 2.13, which is the experimental setup. Each pellet weighs 300mg and has a 12 mm diameter. The thickness is 2.14 mm for glucose, 2.17 mm for fructose, 2.00 mm for maltose, and 2.15 mm for lactose. The materials are presented in Figure 2.14.

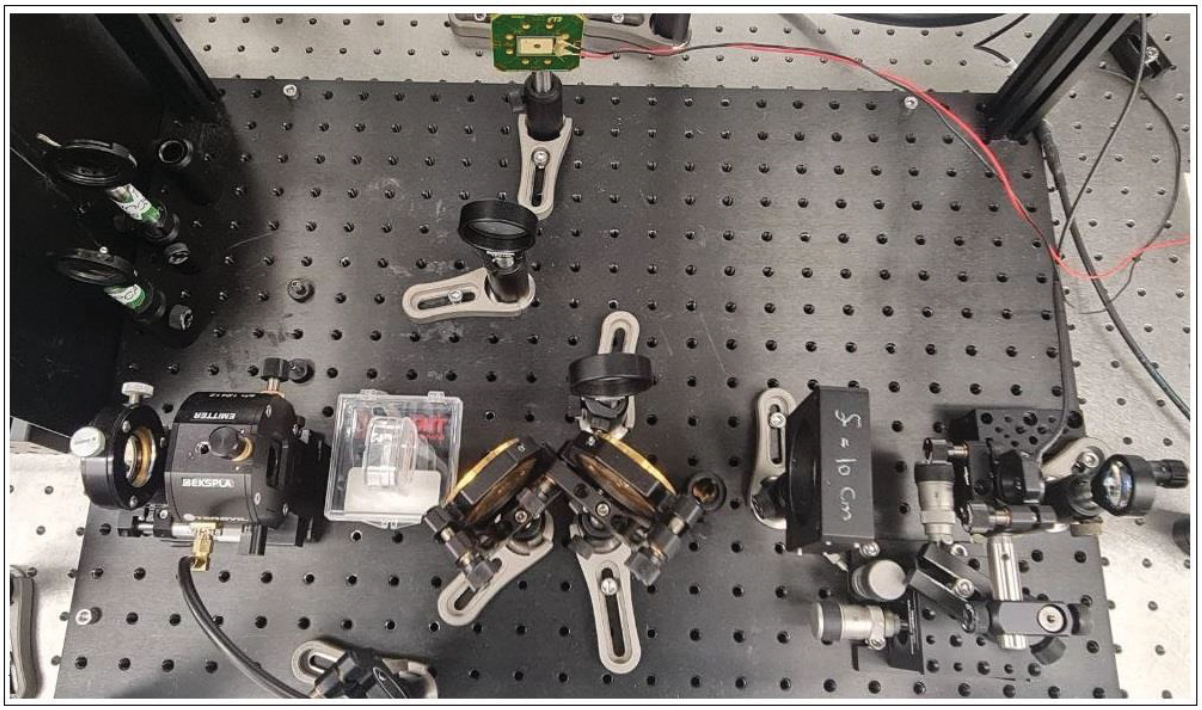

Figure 2.13 Experimental setup of THz-TDDS

Figure 2.14 Materials to be tested
with THz-TDDS setup

Figure 2.15 presents the time domain and spectra of the measurements by the THz-TDDS setup (a and b) and Teraflash (c and d) for reference signal and glucose measurements. The TeraFlash results are obtained with 150 ps of range, 100 averages, and a beam width of 1.6 mm, with a frequency resolution of 6.66 GHz. The results of the THz-TDDS setup are 51.2 ps of range (one scan) and a frequency resolution of 19.52 GHz.

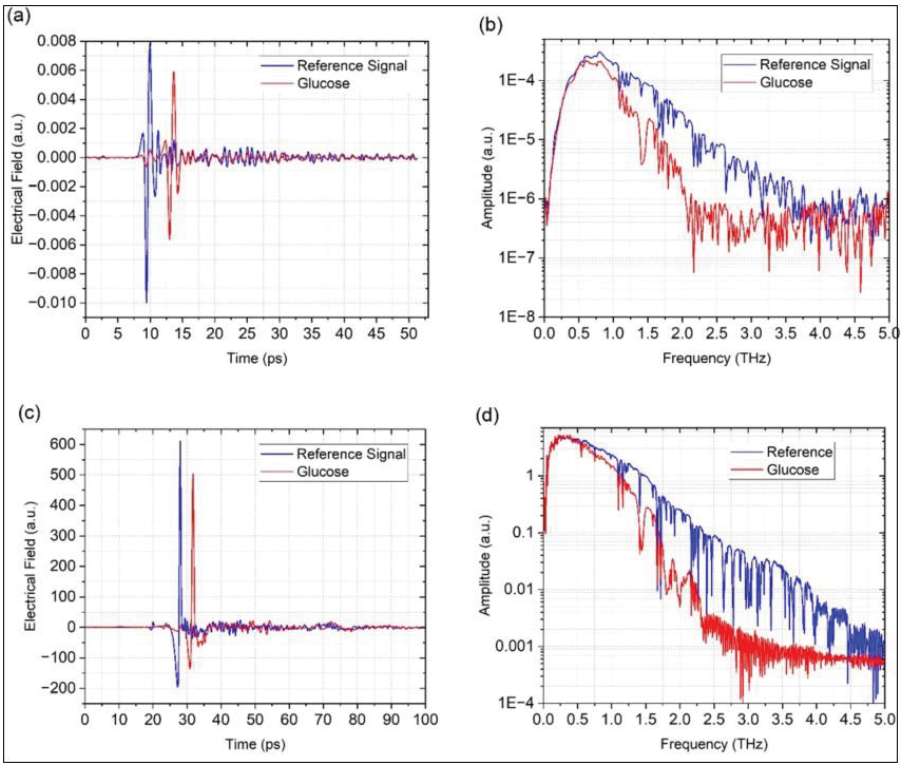

Figure 2.15 Time domain and spectra of glucose obtained by
(a and b) THz-TDDS setup and (c and d) TeraFlash

The impact of water vapor in the air at frequencies such as 1.097, 1.401, 1.718, 1.762, 1.919, 2.198, and 2.453 THz (Cui et al., 2015) can be observed. The same measurement was done for fructose, maltose, and lactose. Their time domain and spectra can be seen in Figure 2.17. After applying the Fourier transform on the time-domain measurement and obtaining the frequency domain data, the refractive index and absorption coefficient are calculated for both measurement systems using the following equations (equations 2.2 and 2.3, respectively)(Jepsen et al., 2011, p.133):

$$n(\omega) = 1 + \frac{\varphi(\omega).c}{\omega.d} \tag{2.2}$$

$$\alpha(\omega) = -\frac{2}{d}\ln\left(\frac{(n+1)^2}{4n}\right)T(\omega) \tag{2.3}$$

where $\varphi(\omega)$ is the difference between the reference and material's phase values, c is the speed of light in vacuum, d is the material thickness, $T(\omega)$ is the transmission (division of samples amplitude over reference's amplitude)(Jepsen et al., 2011). The refractive index presents the THz wave propagation through the material, while the absorption coefficient signifies how much THz wave energy is absorbed by the material. The uncertainties and errors in phase directly affect the refractive index accuracy, and transmission and refraction impact the absorption coefficient calculation (Neu & Schmuttenmaer, 2018). Figures 2.16(a) and (b) show the refractive index and absorption coefficient plots of glucose.

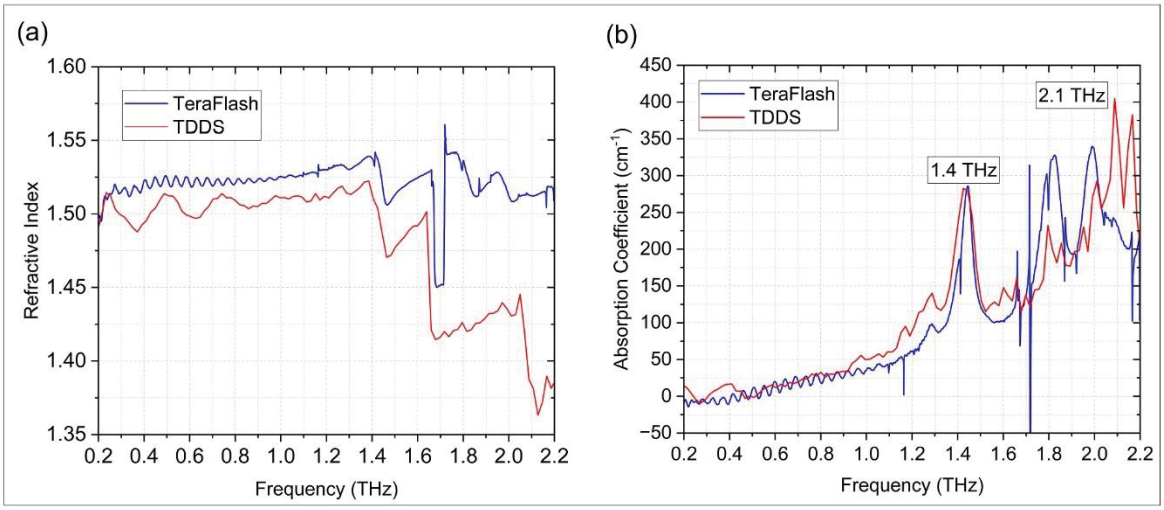

Figure 2.16 (a) Refractive index and (b) absorption coefficient of glucose measured by the THz-TDDS setup (red) and TeraFlash (blue)

Figure 2.16 (b) shows that the glucose absorption peaks are around 1.4 and 2.1 THz. The inaccuracy of measuring the absorption frequencies with the TDDS setup and TeraFlash, compared with the given data and previous research (Da Silva et al., 2022; H. Huang et al., 2022), is due to the water vapor, and the intrinsic jitter of the MD. The next section will discuss jitter and its impact on the SNR. The same process is repeated for the other materials, and their optical parameters are presented in Figure 2.17(c-d) for fructose, (e-f) for maltose, and (g-h) for lactose, for their refractive index and absorption coefficient, respectively. A noticeable deduction for the absorption coefficient in Figures 2.16 and 2.17 is the agreement of values at each material's signature absorption frequency peaks, which are best for glucose, fructose, and lactose. At the same time, the result is not desirable for maltose. At higher frequencies, the SNR of the pellet data is lower than the reference, and the discrepancy becomes visible (Y. Zhang et al., 2016).

Possible errors in the refractive index and absorption coefficient frequency peaks can be caused by three primary sources: the THz beam, the pellet structure, and the oscillating MD. The impacting parameters for the uncertainties due to the THz beam are frequency-dependent beam shape variations (beam divergence, beam waist at the focal point, and Rayleigh length). The uncertainties caused by the pellet comprise the angle of the incident THz beam on each pellet (Y. Zhang et al., 2016), unevenness of the surface of the pellets and parallelism, scattering and inhomogeneity of the material (Withayachumnankul et al., 2008), Christiansen effect (Franz et al., 2008), and any uncertainty in the phase difference between the reference and the sample pellet measurement (Fischer, 2005). Finally, the impact of the MD modulating the THz beam can reduce SNR due to jitter and phase noise. Further fault parameters include water vapor and other mechanical inaccuracies, such as the jitter of the mechanical delay stage and the mechanical vibration of the system (Y. Zhang et al., 2016).

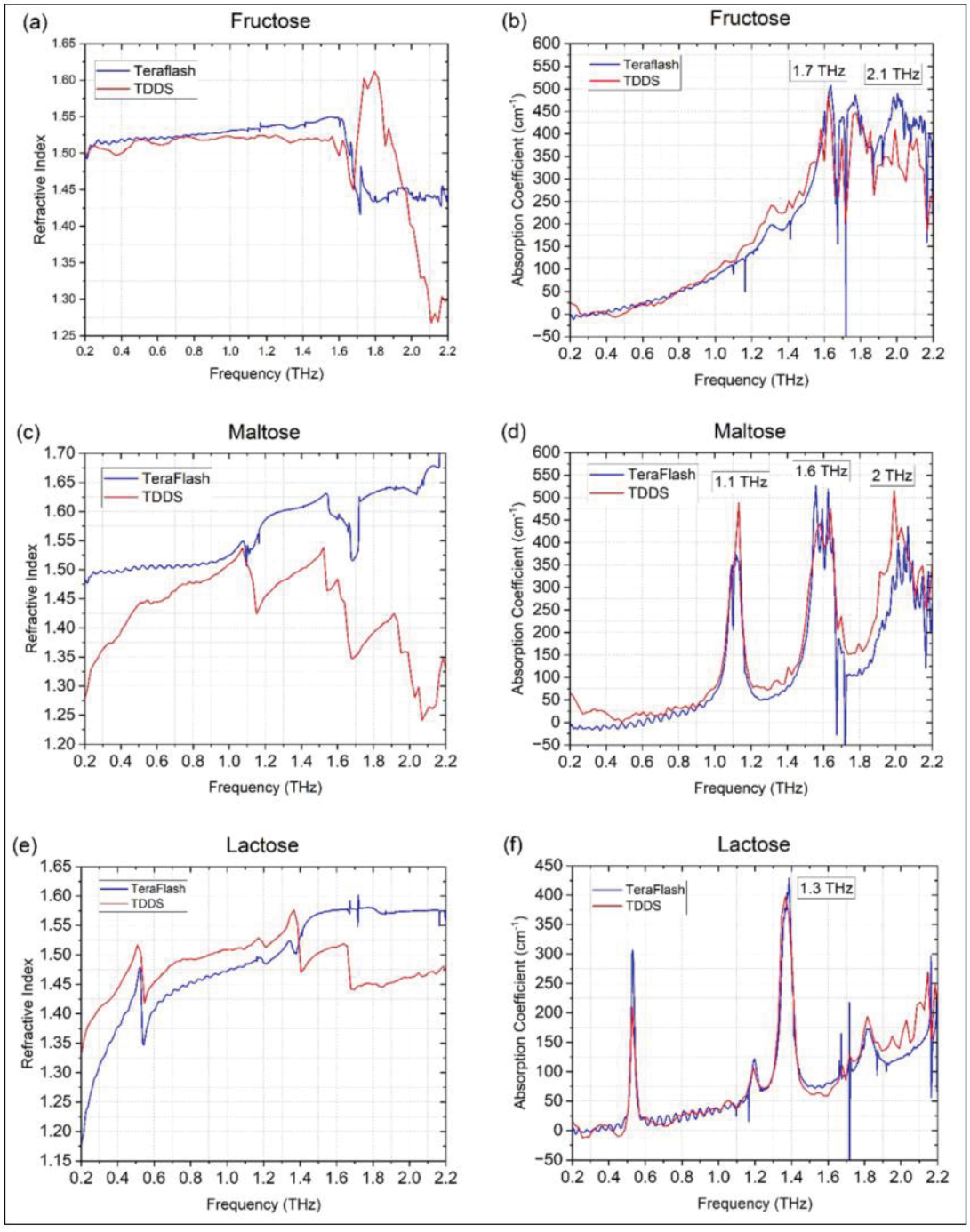

Figure 2.17 The refractive index (left) and absorption coefficient (right) for fructose, lactose, and maltose

It is noteworthy to mention that TeraFlash has better frequency resolution, more number of averaging, higher range, and better SNR compared to THz-TDDS. As discussed, the THz-TDDS setup cannot resolve frequencies lower than 100 GHz and higher than 2.5 THz, affecting the phase values and, therefore, the optical parameters. Aside from the setup-dependent factors, each material's features, such as grain size and structure, can affect the THz phase velocity passing through the material. Benefiting from the Christiansen effect (Franz et al., 2008) for grained powders (each pellet is a compressed form of powder), some refractive index discrepancies can be understood and corrected, which is out of the scope of this thesis. The most prominent source of error in THz-TDDS arises from the intrinsic jitter and resulting phase noise of the MD, which will be discussed and formulated in the next chapter.

2.6 Conclusion

In this chapter, the experimental setup of THz-TDDS and results, as well as verification with a commercial THz-TDS system, are presented, and the performance of the THz-TDDS setup is verified. The cause of discrepancies in the optical parameters will be discussed in the next chapter.

CHAPTER 3

JITTER, PHASE NOISE, AND SNR

3.1 Introduction

Two critical parameters in a noisy oscillator are phase noise and jitter. In the frequency domain, phase noise is the noise spectrum around an oscillator's oscillation frequency (Pulikkoonattu, 2007). Jitter typically indicates the slight, relatively fast variations in the timing of an oscillator period or signal amplitude with respect to the ideal signal. This can introduce some uncertainty over the position or value of the signal (Anthonys, 2022). [Note: To explain jitter and phase noise, these concepts are explained in the context of an oscillator. The principles are expandable to MD, PM, and THz-TDS, which makes it applicable to this thesis.]

3.2 Phase noise

The spectrum of an ideal sinusoidal oscillator with a frequency of f_0 is in the shape of a delta function centered at $-f_0$ and $+f_0$, but in practice, they have spread or leakage of spectral energy around their carrier frequency, which looks like unwanted phase modulated, which is called the phase noise. The example is shown in Figure 3.1.

3.2.1 Phase noise formulation

A carrier signal of a receiver ideally should be equal to the transmitter's carrier $v_0 \cos(\omega_0 t)$. However, in practice, it can be characterized as [Note: all equations in sections from 3.2.1 until 3.2.5 are taken from (Pulikkoonattu, 2007)]:

$$v(t) = v_0\big(1 + \alpha(t)\big)\cos\big(\omega_0 t + \emptyset(t)\big) \tag{3.1}$$

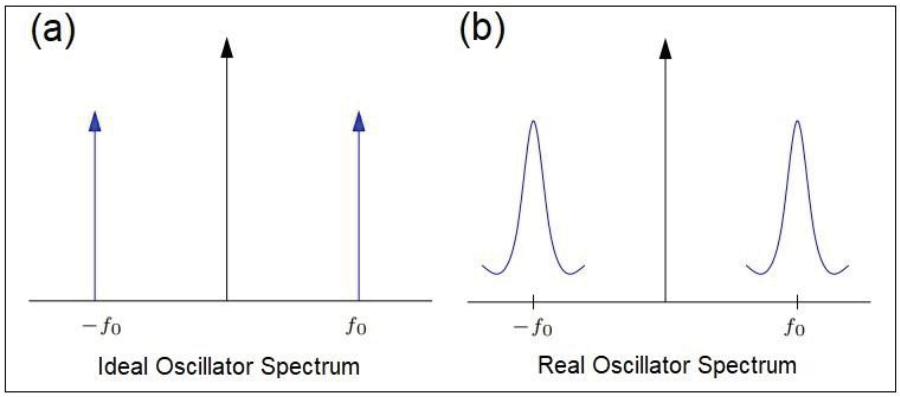

Figure 3.1 Oscillator spectrum, (a) ideal oscillator spectrum as delta function, and (b) an actual oscillator with energy leakage around the oscillation frequency in a two-sided power spectrum
Taken from (Pulikkoonattu, 2007)

Where $\omega_0 = 2\pi f_0$ and $\alpha(t)$ is amplitude noise, $\emptyset(t)$ is phase noise, which can have both random and deterministic segments. The deterministic part is related to supply voltage, output impedance, temperature variations, and other factors, while the random part can be described by power spectral density (PSD). For a broadband signal, it is necessary to look at the PSD as it gives the power per frequency band. The instant frequency of $v(t)$ is:

$$f(t) = \frac{1}{2\pi}\frac{d}{dt}[2\pi f_0 + \emptyset(t)] \tag{3.2}$$

Moreover, the fractional frequency is described as follows:

$$y(t) = \frac{\Delta f(t) = [f(t) - f_0]}{f_0} = \frac{1}{2\pi f_0}\frac{d\emptyset(t)}{dt} \tag{3.3}$$

Where $\emptyset(t)$ and $y(t)$ are considered stationary, their autocorrelation function $R_y(\tau)$ is:

$$R_y(\tau) = \langle y(t), y(t-\tau)\rangle \tag{3.4}$$

Thus, the double-sided PSD or S_y^{DS} is the result of the Fourier transform on $R_y(\tau)$:

$$S_y^{DS}(f) = \int_{-\infty}^{+\infty} R_y(\tau)e^{-j2\pi f\tau}d\tau \tag{3.5}$$

Which gives the single-sided PDS or S_y^f as:

$$S_y(f) = \begin{cases} 2S_y^{DS}(f), & f \geq 0 \\ 0, & f < 0 \end{cases} \tag{3.6}$$

3.2.2 Phase noise power spectral density

The power spectrum of instant frequency change is equivalent to the power spectral density of the phase noise $\emptyset(t)$ by having $S_\emptyset(f) = \frac{f_0^2}{f^2} S_y(f)$. Thus, the calculation of the autocorrelation of $\emptyset(t)$ is presented as:

$$R_\emptyset(\tau) = \langle \emptyset(t), \emptyset(t-\tau) \rangle \tag{3.7}$$

After Fourier transform calculation, the double-sided PSD or $S_\emptyset^{DS}(f)$ is obtained:

$$S_\emptyset^{DS}(f) = \int_{-\infty}^{+\infty} R_\emptyset(\tau) e^{-j2\pi f\tau} d\tau \tag{3.8}$$

The single-sided presentation $S_\emptyset(f)$ or $S(f)$ is calculated as:

$$S(f) = \begin{cases} 2S_\emptyset^{DS}(f), & f \geq 0 \\ 0, & f < 0 \end{cases} \tag{3.9}$$

Mathematically, the phase noise PSD is described by the power law:

$$S(f) = \sum_{n \geq 0, n \in \mathbb{R}} h_n f^n \tag{3.10}$$

The phase noise PSD generally represents a piecewise exponential function in relation to the offset frequency from the oscillator's central frequency. Considering the specified power measured (in dBc/Hz) at the bandwidth of 1Hz at the corner frequencies of phase noise PSD, the slopes can be obtained. The PSD form of the simplified random phase noise derived from Equation (3.10) for three corner frequencies is formulated as:

$$S(f) = \begin{cases} b, & f_3 \le f \\ \frac{c}{f}, & f_2 \le f \le f_3 \\ \frac{d}{f^2}, & f_1 \le f \le f_2 \end{cases} \tag{3.11}$$

In Equation (3.11), *b*, *c*, and *d* are constants representing the noise power coefficients for each process. In Equation (3.10), if *n=0*, it represents *b*, or white phase noise, which is frequency-independent due to thermal noise. If *n=-1*, the $^{c}/_{f}$ presents Flicker phase noise arising from imperfections in the device. Finally, if *n=-2*, the $^{d}/_{f^2}$ segment represents white frequency noise due to random processes like shot noise. Figure 3.2 presents the phase noise PSD and the slopes for each corner frequency. The phase noise PSD has a dBc unit (dB carrier). The simplified form of random phase noise PSD can be modeled as piecewise in dB, where each segment has a different slope.

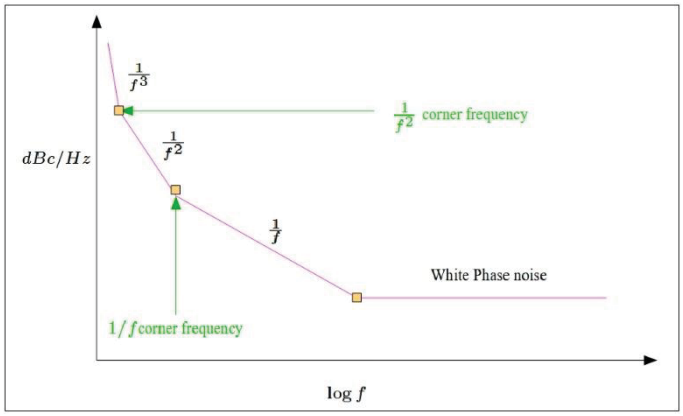

Figure 3.2 PSD of phase noise, as piecewise linear
on logarithmic x-axis
Taken from (Pulikkoonattu, 2007)

As presented later in this chapter, Figures 3.10, 3.13, and 3.14 have benefited from Equation (3.10) and follow the simplified phase noise PSD shown in Figure 3.2. The simplified form of phase noise PSD (Equation 3.11) does not apply to MD, as other noise sources influence it.

3.2.3 Phase noise in the time domain

The fractional frequency offset $y(t)$ variance (as a result of phase noise) is defined as:

$$\sigma^2(\tau) = \langle y^{-2} \rangle = \frac{1}{\tau^2} \langle \left[\int_{t_k-\tau}^{t_k} y(t)dt \right]^2 \rangle \tag{3.12}$$

The variance here is calculated over a short period $[-\tau, 0]$, where τ is an integer multiple of $1/f_0$. To filter with a rectangular window function $h(t) \in [-\tau, 0]$ and by averaging over τ gives the following description for variance:

$$\sigma^2(\tau) = \langle \left[\int_{-\infty}^{+\infty} y(u)h(t-u)du \right]^2 \rangle \tag{3.13}$$

The rectangle window function is needed to pass through the power for the frequency that is being sampled. To facilitate the calculation, in the frequency domain, it can be calculated as:

$$\sigma^2(\tau) = \int_0^{\infty} S_y(f) \|H(f)\|^2 df \tag{3.14}$$

From Equation (3.6) $S_y(f)$ is the single-sideband phase noise PSD. Here $\|H(f)\|^2$ is the equivalent noise bandwidth of the rectangle window function, described as:

$$\|H(f)\|^2 = \left(\frac{\sin \pi\tau f}{\pi\tau f} \right)^2 \tag{3.15}$$

Note that the variance here is for the fractional frequency offset. As the time series is stationary, meaning, from a statistical point of view, the variance of the signal is the same regardless of where the rectangular window is applied.

3.2.4 Jitter

In digital systems, the clock is used for sampling and holding, which can happen either at the falling or rising edge when the clock signal's amplitude reaches a certain defined value. Noise is one of the reasons that would make the clock imperfect and affects the time interval between consecutive clocks by random jitter. Note that jitter can be deterministic or random. Figure 3.3 presents the concept of clock imperfection (Pulikkoonattu, 2007).

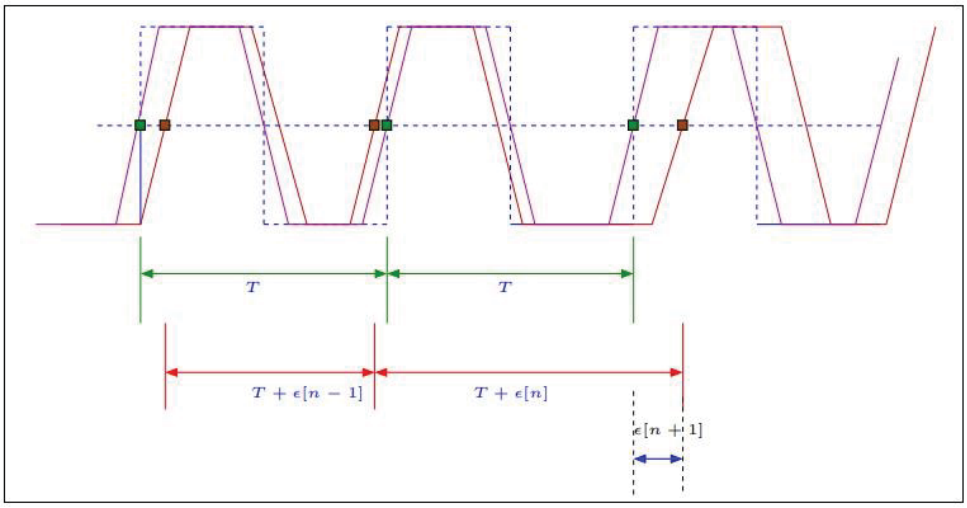

Figure 3.3 Sampling clock jitter, representing the random nature of jitter
Taken from (Pulikkoonattu, 2007)

3.2.5 Phase jitter

The phase jitter was initially and briefly presented in Chapter 1. The detailed calculation is presented here. The goal is to use the mathematical tools in time and frequency domains to explain the physical phenomena of MD jitter's impact on signal integrity and timing, which will impact the data obtained by THz-TDDS and the material characterization. Therefore, phase jitter mathematical representation is explained in this section. It is possible to calculate the phase variance $\sigma_{\emptyset}^2(\tau)$ and RMS phase jitter for phase noise $\emptyset(t)$ instead of time variance in instant frequency offset $y(t)$, which follows the same process.

$$\sigma_{\emptyset}^2(\tau) = \langle\overline{\emptyset^2}\rangle = \frac{1}{\tau^2}\langle\left[\int_{t_k-\tau}^{t_k} \emptyset(t)dt\right]^2\rangle \tag{3.16}$$

Thus, similarly the rectangle window function $h(t) \in [-\tau, 0]$ is applied,

$$\sigma_{\emptyset}^2(\tau) = \langle\left[\int_{-\infty}^{+\infty} \emptyset(u)h(t-u)du\right]^2\rangle \tag{3.17}$$

Using the Equations (3.14) and (3.15), it gives:

$$\sigma_{\emptyset}^2(\tau) = \int_0^{\infty} S(f)\left(\frac{\sin\pi\tau f}{\pi\tau f}\right)^2 df \tag{3.18}$$

Where $S(f)$ is the phase noise PSD and $\left(\frac{\sin\pi\tau f}{\pi\tau f}\right)^2$ is the equivalent noise bandwidth of the rectangle window function. Therefore, the phase jitter (RMS) J can be defined as:

$$J = \frac{\sigma_{\emptyset}}{2\pi f_0} \tag{3.19}$$

Here, $\sigma_{\emptyset}$ is the mean, and f_0 is the frequency being sampled. Combining the Equations (3.18) and (3.19) gives:

$$J = \frac{1}{2\pi f_0}\sqrt{\int_0^{\infty} S(f)\left(\frac{\sin\pi\tau f}{\pi\tau f}\right)^2 df} \tag{3.20}$$

The part $\left(\frac{\sin\pi\tau f}{\pi\tau f}\right)^2$ can be generally ignored as it is unity for $f_\tau \approx 0$. After this approximation, the RMS phase jitter for $S(f)$, the phase noise PSD, can be written as:

$$J = \frac{1}{2\pi f_0}\sqrt{\int_0^{\infty} S(f)df} \tag{3.21}$$

The RMS phase jitter depends on the square root of the phase noise PSD.

In the case of a THz pulse, where there is a very short-term event, if averaged across a long window, it can potentially get lost in the noise. That is why a lock-in amplifier is needed to

detect the signal in the noisy background. Interested readers can refer to Annex II to learn about the phase noise and jitter in THz-TDS.

3.3 Jitter, phase noise, and SNR calculation and simulation using MATLAB

To understand the impact of jitter on THz pulse, a Matlab script has been developed, which can be referred to in Annex III. Here, I create a reference (ideal) THz pulse and apply various values of jitter to see its impact on the time domain and spectra of the THz pulse. According to Equation (3.1), a sine wave with phase modulation (the phase modulation is the added jitter) is added to the ideal THz pulse. By changing the modulation index to 16 different values, 16 different jittered signals are compared with the ideal THz pulse to calculate their time domain and spectra and see the impact of the jitter on them. Finally, SNR is calculated based on the jitter severity to show its exponential decay relation. A Monte Carlo method with 10000 averaging provides robust SNR vs. jitter investigation results. Figure 3.4 presents the time domain THz pulse, and Figure 3.5 presents the spectra for reference and each jitter value applied to the signal. It also shows how jitter impacts frequencies below 100 GHz and above 3.4 THz, indicating how jitter affects very low and high frequencies.

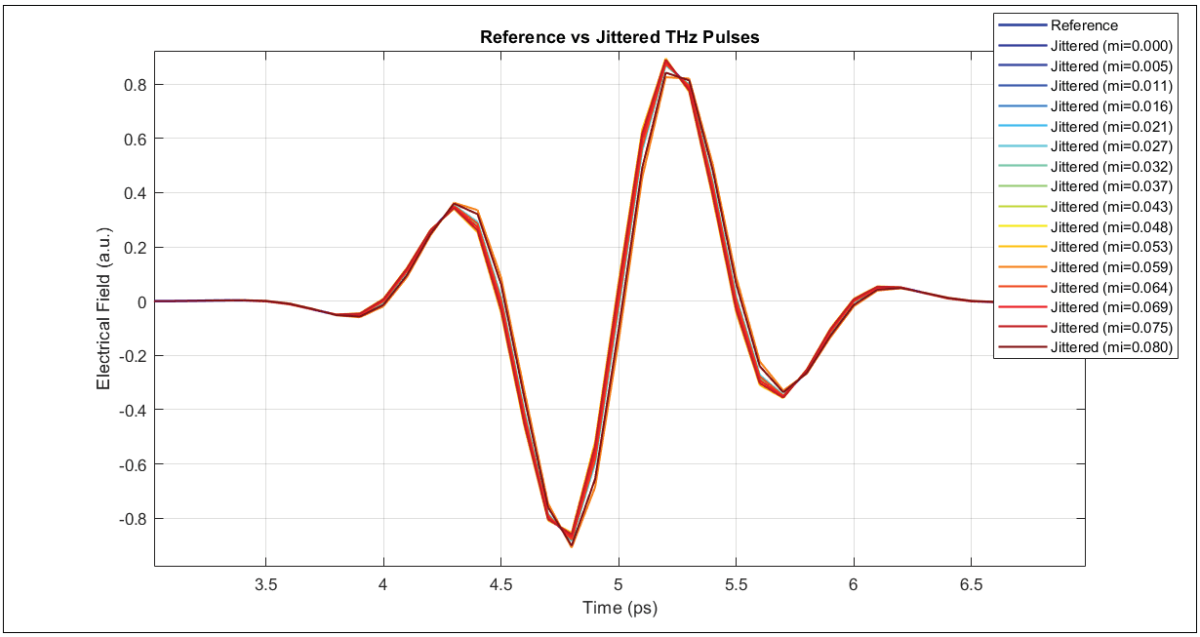

Figure 3.4 Impact of jitter on THz pulse in the time domain

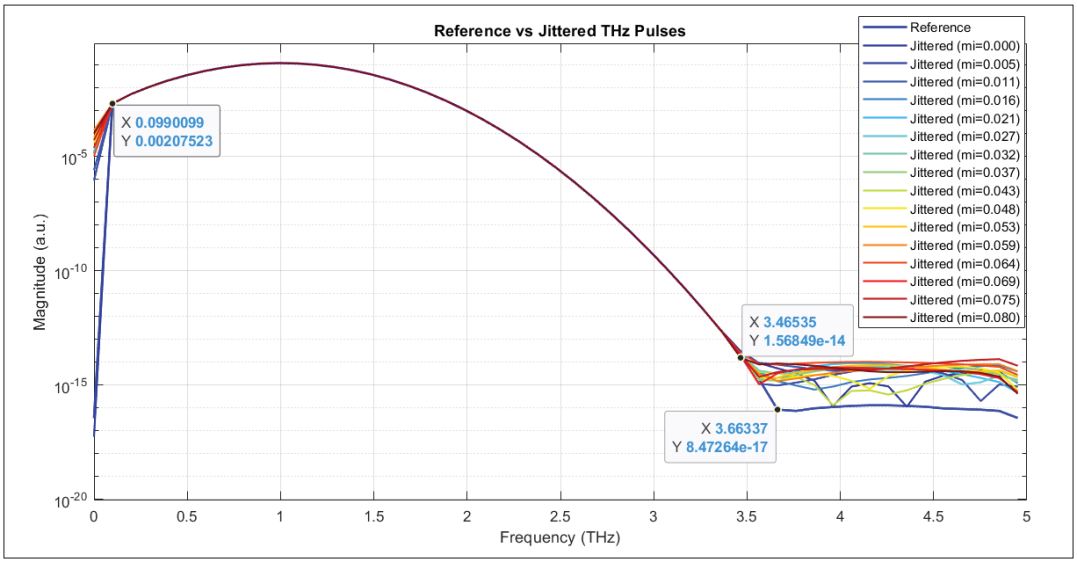

Figure 3.5 Impact of jitter on THz pulse spectra

Figure 3.6 shows the relation between SNR and jitter severity. With jitter severity increases, the SNR decays exponentially, highlighting the impact of jitter in the system. Therefore, jitter measurement, identification, and management are critical as they directly impact the refractive index calculations in low and high frequencies. The SNR seems to saturate with higher jitter values, meaning that the SNR variation is relatively low (approximately ± 40 dB) compared to lower values of jitter where SNR drops significantly.

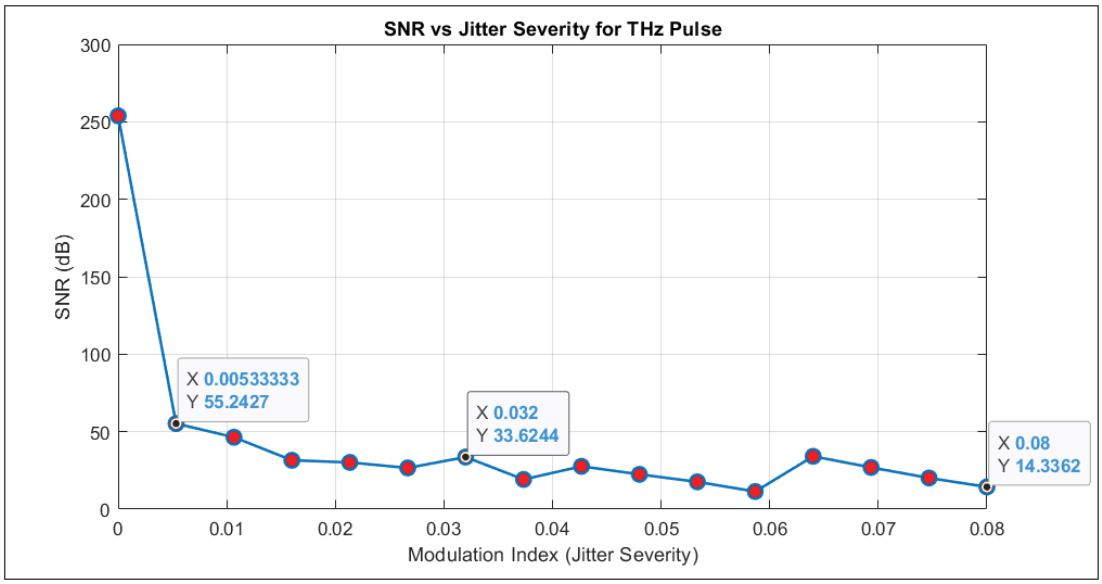

Figure 3.6 SNR vs. jitter severity

To simulate the jitter, phase noise, and SNR for MD, a Matlab script has been developed, which is presented in Annex IV. There are parameters to consider for this simulation that will be discussed here. The first step is to measure the oscillation of MD with a Vibrometer to find the frequency that gives the maximum oscillation amplitude and measure its magnitude at the resonance frequency. Then, from this dataset, the amplitude is calculated using FFT, and the magnitude in dB will be used for phase noise calculation. A set of parameters need to be defined to calculate the phase noise. The phase noise pre-defined function is:

>> PNMeasure = phaseNoiseMeasure(Xin,Yin,RBW,FrOffset,PlotOption,tag,Name,Value)

With the following parameters:

- Xin: positive real-time (sec) or frequency (Hz) vector- in this case, it is the frequency vector
- Yin: real signal value (v) or magnitude vector (dB)- in this case it is magnitude in dB
- RBW: the resolution bandwidth in the spectrum analysis, positive real scalar in Hz. It defines “the smallest positive frequency at which the frequency components of a signal can be resolved”- 1 Hz in this case

- FrOffset: Frequency offset values to calculate the phase noise at these points as a positive real vector in Hz- for the MEMS speaker, the set is [2.5 5 10 100 1000 2500 5000 10000] Hz
- PlotOption: to plot the phase noise and the power spectrum

One of the critical parameters is the resolution bandwidth, as the result rigorously changes with changing this parameter. The resolution bandwidth determines the window length using the Welch method in the spectral analysis. The requirement is to have the resolution bandwidth less than the lowest offset frequency value. In practice, the phase noise is measured by a spectrum analyzer. Resolution bandwidth is a measurement limitation that must be carefully assigned. The spectrum analyzer measures all the energy detected in the resolution bandwidth around each frequency point. As no resolution filter can provide a perfect out-of-band rejection, a signal in the rejection band might be powerful enough to affect the rejection filter and make the wrong measurement of the energy at each frequency point. This distortion can be very common in the lower offset frequencies for measuring the oscillator's phase noise. Figure 3.7 presents the explained concepts.

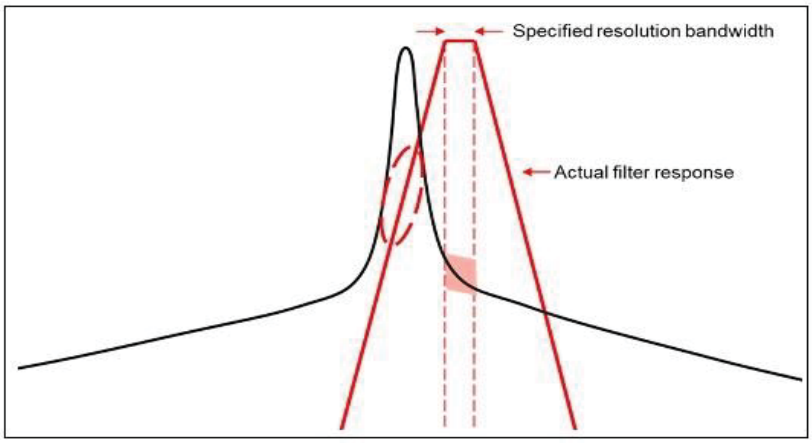

Figure 3.7 Resolution bandwidth impact on the signal energy
Taken from (*Phase Noise in Oscillators - MATLAB & Simulink*, 2024)

As shown in Figure 3.7, the red line shows the resolution filter and the desirable measurement in the resolution bandwidth is pink. Nevertheless, the resolution filter brings considerable

energy (out-of-band leakage) from the oscillator's primary signal to leak into the measurement result (shown with the red dashed oval), which gives more energy than the amount it should measure. At the expense of higher measurement time, the resolution bandwidth can be assigned to avoid the out-of-band leakage of energy. Consequently, the resolution bandwidth can affect the phase noise value, noise floor, and SNR.

An essential step for the calculations and simulations is calculating the phase noise for the function generator that feeds the MD and comparing it with its datasheet. This step provides a perspective on the scale of phase noise PSD for MD and to validate the calculation results. Initial calculations showed a 70 dB discrepancy between the measurement results for the function generator (Keysight 33600 Trueform Waveform Generator) and the information on the datasheet. This highlights the noise in the Vibrometer acquisition card, which is not explicitly designed for this functionality. In MEMS-relevant studies, jitter and phase noise are not common figures of merit. Therefore, this problem was not identified previously by the MEMS designers at ÉTS. By adding 70 dB compensation to the calculations, the phase noise value of the function generator matches the datasheet, and the calculated data for MD is validated. For the MD, the plots of power spectrum and phase noise can be seen in Figure 3.8. Phase noise PSD in dBc/Hz with linear frequency (x-axis) is presented in Figure 3.9. Then, in reference to Figure 3.2 and PSD Equation (3.11), Figure 3.10 presents the phase noise PSD with logarithmic frequency x-axis at each offset frequency. For all calculations and simulations, the resolution bandwidth is assigned as 1 (RBW=1).

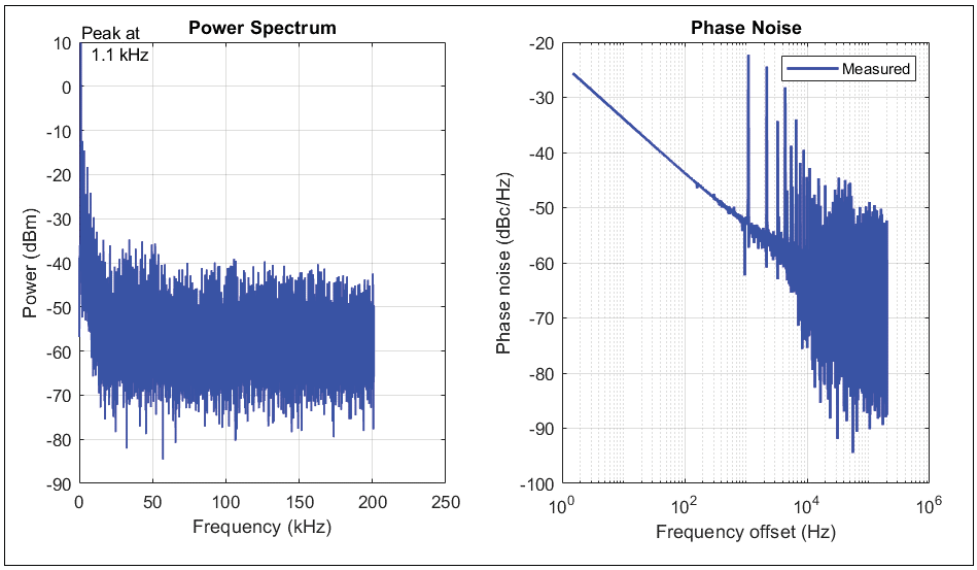

Figure 3.8 (left) Power spectrum (in dBm) and (right) phase noise (in dBc/Hz) with logarithmic frequency x-axis for MD

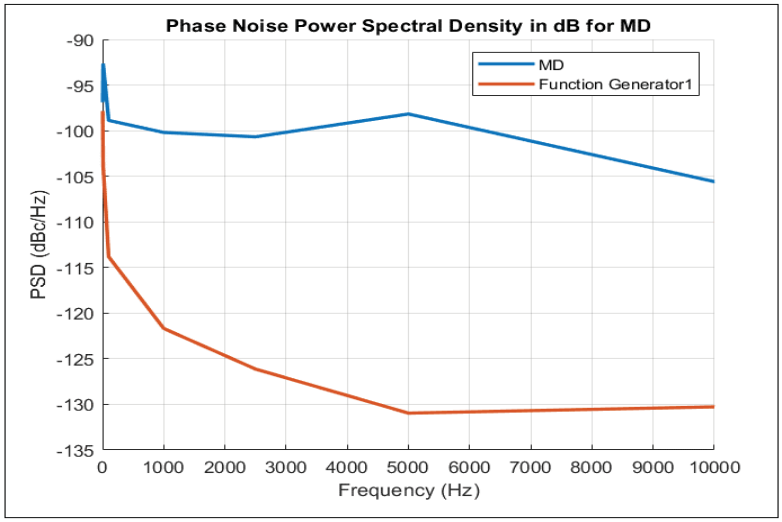

Figure 3.9 Phase noise PSD (in dBc/Hz) calculated for each offset frequency value (frequency in linear scale) for MD

In Figures 3.9 and 3.10, the phase noise PSD for the function generator is shown in orange, and the MD in blue.

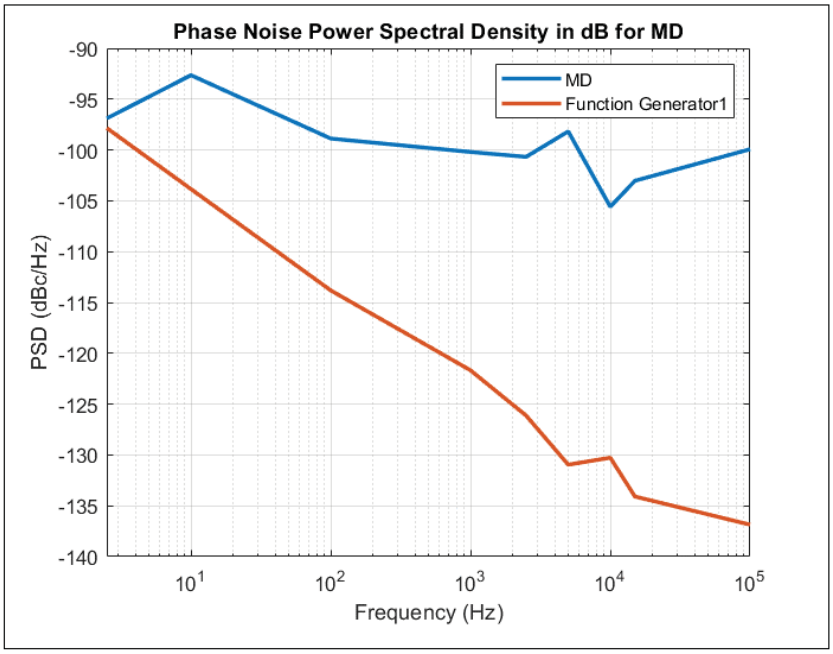

Figure 3.10 Phase noise PSD (in dBc/Hz) calculated for each offset frequency value for MD

Having the phase noise, the jitter can be calculated. The Matlab function is:

>>[Jrms_rad,Jrms_deg,Jrms_s]=phaseNoiseToJitter(FrOffset,PNMeasure,'Frequency',frequency)

The inputting parameters are:

- FrOffset: As discussed above, the offset frequencies are relative to the central frequency where the phase noise is calculated. It is a real value vector in Hz.
- PNMeasure: It is the phase noise power measured in the previous step at the specific frequency offset relative to the central frequency. It is calculated in 1 Hz bandwidth as a real value vector in dBc/Hz unit.
- Frequency: the signal frequency, which is the MD's resonant frequency (1.1 kHz). This parameter is needed to calculate the RMS phase jitter (in seconds). The output parameters (RMS phase jitter) can be converted to radians, degrees, or seconds.

The MD is driven by a function generator, feeding a sinusoidal wave with 20 Vp-p and 1.1 kHz frequency. Therefore, it is necessary to calculate the phase jitter of the function generator and MD to observe the scale of the jitter produced by the MD. The results are presented in Table 3.1.

Table 3.1 RMS phase jitter calculation results at f = 1.1 kHz

	Modulating device (MD)	**Function generator**
RMS phase jitter (rad)	3.8704×10^{-3}	1.2244×10^{-4}
RMS phase jitter (sec)	5.600×10^{-7}	1.7715×10^{-8}

Compared with the previous work (Amirkhan et al., 2021) using the PM device, the exact measurements (using a Vibrometer), calculations, and simulations are conducted. The results can be seen in Figures 3.11-3.13 and Table 3.2. The noise compensation for this measurement (as explained earlier) is 80 dB for PM.

Table 3.2 RMS phase jitter calculation results at f = 10.68 kHz

	PM (Amirkhan et al., 2021)	**Function generator**
RMS phase jitter (rad)	7.7046×10^{-4}	1.0852×10^{-4}
RMS phase jitter (sec)	1.1481×10^{-8}	1.6172×10^{-9}

Figure 3.11 shows PM's power spectrum and phase noise (Amirkhan et al., 2021).

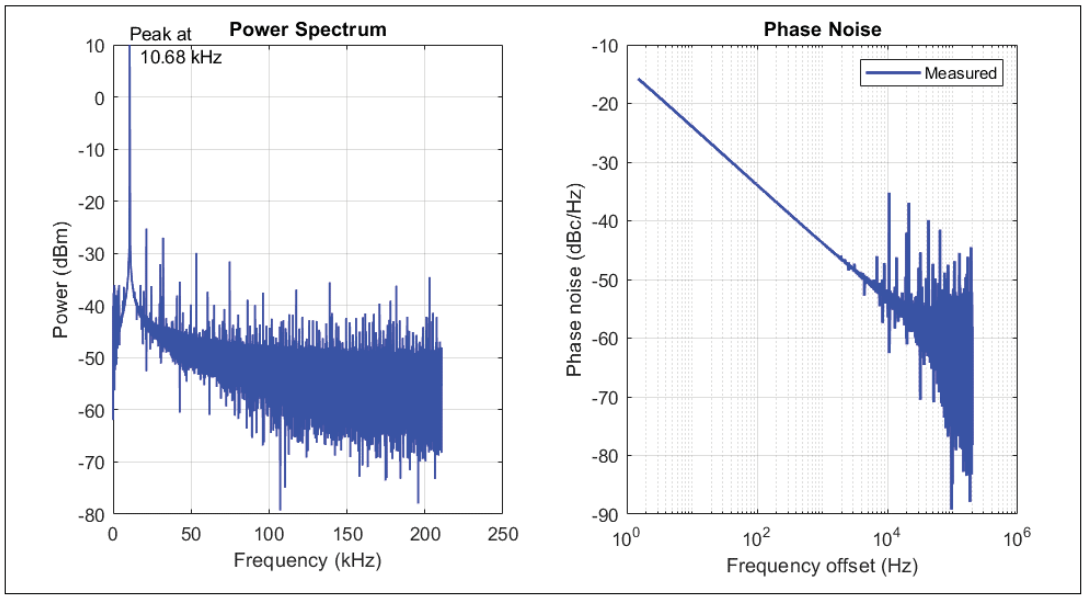

Figure 3.11 (left) Power spectrum (in dBm) and (right) phase noise (in dBc/Hz) with frequency (in logarithmic x-axis) for PM

Phase noise PSD for PM in linear frequency and logarithmic frequency x-axis are presented in Figures 3.12 and 3.13, respectively.

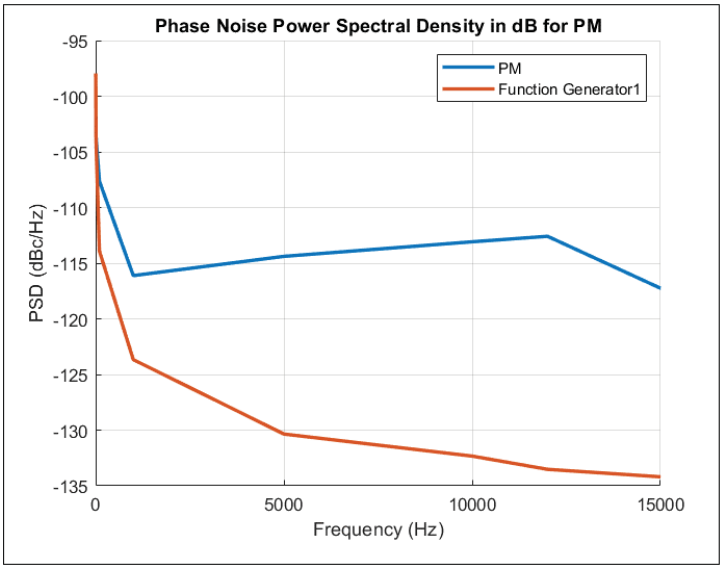

Figure 3.12 Phase noise power spectral density (in dBc/Hz) calculated for each offset frequency (frequency in linear scale) for PM

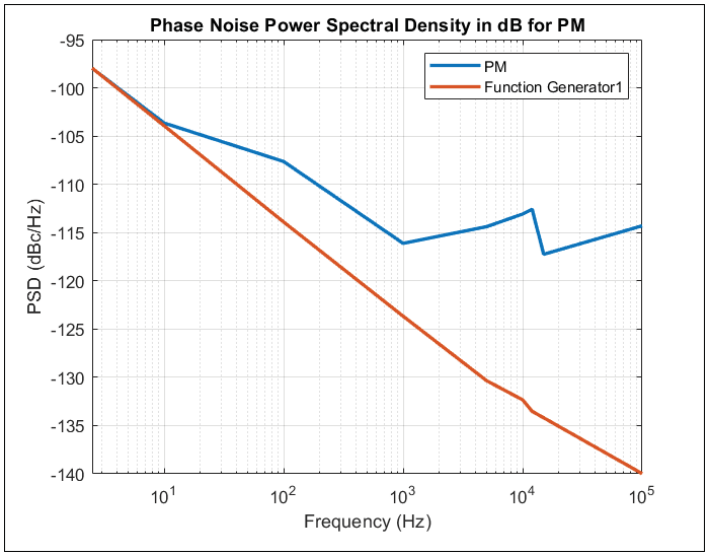

Figure 3.13 Phase noise PSD (in dBc/Hz) calculated for each offset frequency value (frequency in logarithmic scale) for PM

Figure 3.14 compares phase noise power spectral density for MD, PM, and the function generator. The higher phase jitter of MD results in 16 dB less power PSD at 1 kHz, therefore 14 dB less SNR as presented in Table 3.3.

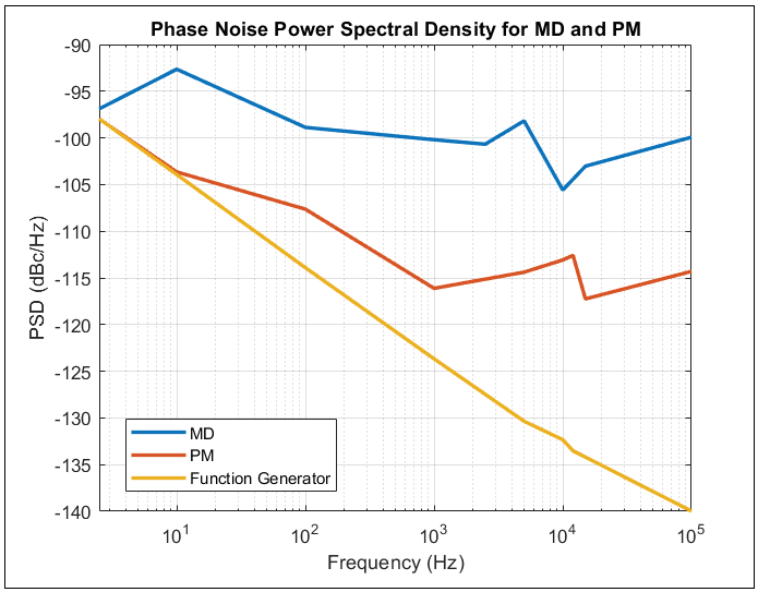

Figure 3.14 Phase noise PSD comparison for MD, PM, and function generator

For PM, noise types including $^1/_f$ and $^1/_{f^2}$ can be observed, which might be due to the noise in the system, while in the MD, various types of noise can recognized.

Table 3.3 SNR at measured phase jitter for MD and PM

	SNR (dB)
Average SNR at measured phase noise for MD ($3.8704 \times 10^{-3} rad$)	48.26
Average SNR at measured phase noise for PM ($7.7046 \times 10^{-4} rad$)	62.28

Figure 3.15 shows the relation between SNR and RMS phase jitter (rad). For this purpose, SNR is calculated for a range of multipliers of RMS phase jitter and plotted for both MD and PM. The relationship between jitter and SNR can involve integration over the entire bandwidth of interest. Phase variations increase leads to exponential decay of the SNR (Mittleman, 2003; Sharma et al., 2013). The relation between SNR and phase variations ($\Delta\emptyset$) due to phase noise can be approximated as (Sharma et al., 2013):

$$SNR \approx \frac{1}{\Delta\emptyset^2} \tag{3.22}$$

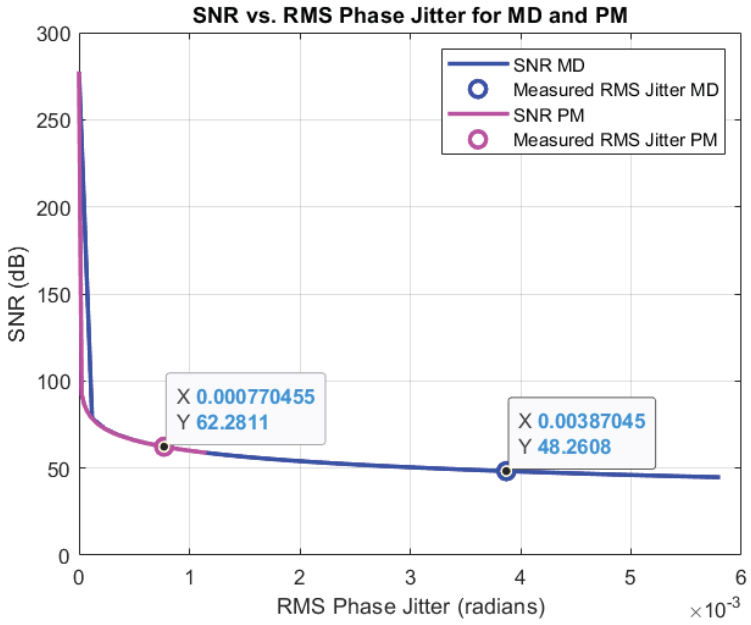

Figure 3.15 SNR vs. RMS phase jitter for MD and PM

The 14 dB difference of SNR between MD and PM is visible in Figure 3.15, emphasizing the negative impact of phase jitter on the SNR. To investigate how the lock-in amplifier's reference has been affected by the jitter from MD and PM, a Matlab script has been developed and presented in the next section.

3.4 MD jitter and its impact on the lock-in amplifier

As explained in Chapter 1, the lock-in amplifier is a critical part of THz-TDS detection that can find the signal in a noisy background and amplify it, as shown in Figure 3.16. It measures the amplitude and phase of a signal relative to a reference (Zurich Instruments, 2023).

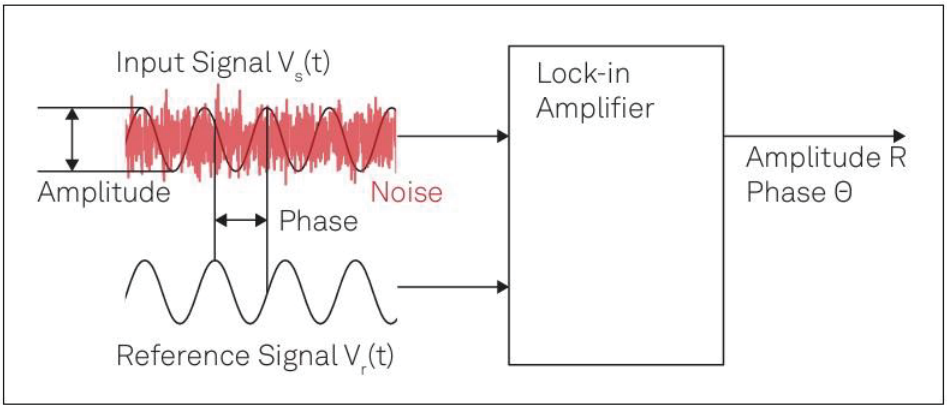

Figure 3.16 Lock-in amplifier functionality
Taken from (Zurich Instruments, 2023)

The lock-in measurement method is shown in Figure 3.17.

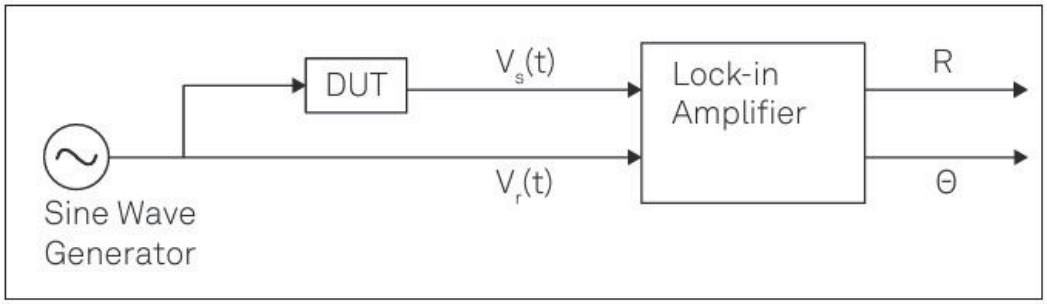

Figure 3.17 Lock-in measurement diagram, showing a sine wave to stimulate the device under test and provide the reference to the LIA
Taken from (Zurich Instruments, 2023)

It works based on the correlation function, where a very faint signal detected from the experiment *g(t)* with a time parameter δ ranging from 0 to ∞ that is superimposed with noise is correlated with the known or reference signal *f(t)* in an integration time of T as formulated below (*The Lock-In Amplifier: Noise Reduction and Phase Sensitive Detection*, n.d.):

$$R(\delta, T) = \frac{1}{T}\int_0^T f(t).\, g(t+\delta)dt \tag{3.23}$$

Here, *R* represents the correlation between g and f at time δ. This correlation function is not zero because there is a correlating non-zero *g(t)* signal from the experiment. In the simplest case of a sinusoidal reference and input signal (*The Lock-In Amplifier: Noise Reduction and Phase Sensitive Detection*, n.d.):

$$f_{ref}(t) = A_{ref}\sin(\omega_r + \emptyset_{ref}(t)) \tag{3.24}$$

$$g_{sig}(t) = A_{sig}\sin(\omega_s t + \emptyset_{sig}(t)) \tag{3.25}$$

The instantaneous phase difference or the measurement phase shift is $\Delta\emptyset = \emptyset_{sig}(t) - \emptyset_{ref}(t)$ that can vary randomly over time. Using the correlation function, the periodic electric signal content (buried in noise) can be detected. The autocorrelation function can be explained as (*The Lock-In Amplifier: Noise Reduction and Phase Sensitive Detection*, n.d.):

$$R(nT, \Delta\emptyset) = \frac{A_{ref}A_{sig}}{nT}\int_0^{nT} \sin(\omega_r t)\,.\sin(\omega_s t)\,dt \tag{3.26}$$

T is the period of the frequency reference frequency, and nT is the upper integral limit, n being a finite integer. After passing through the RC filter, the high-frequency term is filtered out if $\omega_r = \omega_s$, and the detected DC output stays (Kloos, 2018):

$$g_{DC}(t) = \frac{A_{ref}A_{sig}}{2}\cos(\Delta\emptyset(t)) \tag{3.27}$$

The detected DC output depends on $\cos(\Delta\emptyset(t)) = \cos(\emptyset_{sig} - \emptyset_{ref})$, which is affected by jitter. As a result, with the random fluctuations in $\cos\Delta\emptyset(t)$, the output will not be only a DC signal and DC part of output will vary, leading to amplitude noise or phase noise. If $\Delta\emptyset(t)$ has significant variance, the effective sensitivity of the measurement is reduced. Furthermore, with

unstable ΔØ, the phase shift identification between the measurement signal and the reference becomes challenging. Thus, the lock-in amplitude reading will not be optimal, impacting the SNR(Kloos, 2018). The MD's jitter raises the noise floor, and by reducing the accuracy of lock-in reading and compromising its narrowband detection, the signal filtering from noise will not be done accurately. To mitigate the impact of jitter, longer time constants or integration time can be implemented, which slows down the measurements. Finally, in phase-sensitive applications such as optical parameter characterization of materials, jitter causes significant errors and incorrect interpretations.

A Matlab script has been developed to model the impact of MD and PM on lock-in amplifier detection, as presented in Annex V. This script mimics the LIA functionality, mixing a reference signal from either MD or PM with an input THz pulse, passing through the LPF, and giving the output THz pulse. To study the impact of jitter, the phase noise of MD (and PM) is added to the reference signal, and 1000 THz input pulses are given as input (Figure 3.18). [Note: Only 10 out of 1000 pulses are plotted due to simulation processing limitations.]

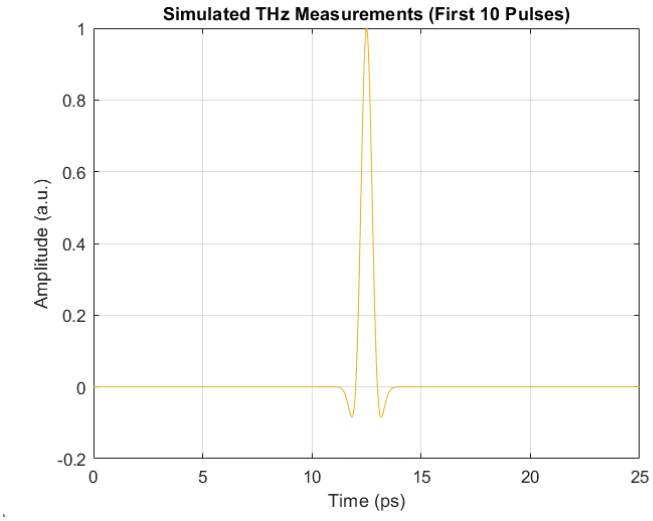

Figure 3.18 Simulated THz input pulses

After mixing the jittered reference with THz pulses (Figure 3.19), one point on each output is selected (the point is the same for all pulses) and plotted to show the impact of phase noise on the THz time domain pulse variations (Figures 3.20-3.21). Due to the higher phase noise of MD, the distribution of the points is five times higher compared with PM's phase noise impact on the THz time domain pulses (Figure 3.22).

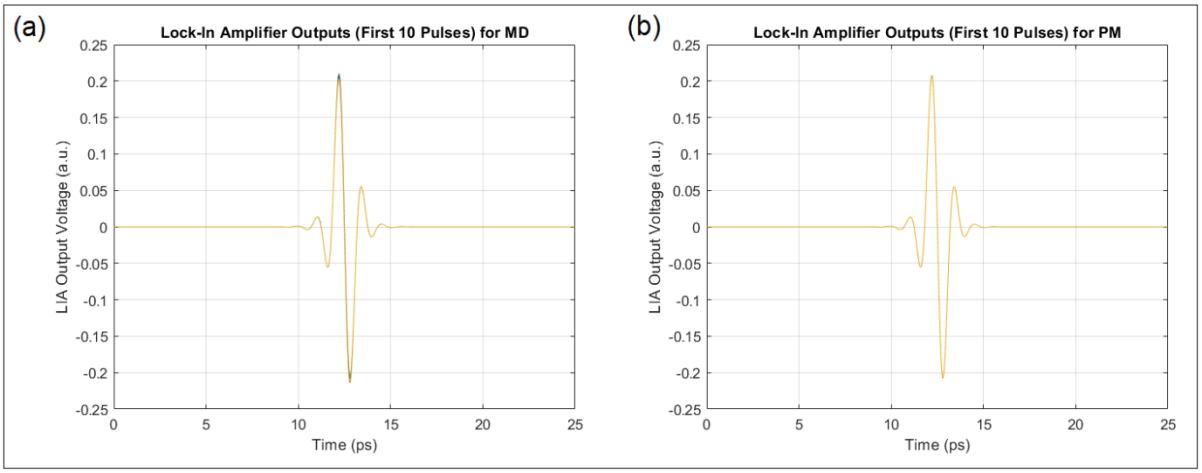

Figure 3.19 Lock-in amplifier outputs after mixing the input pulses with jittered references from (a) MD and (b) PM

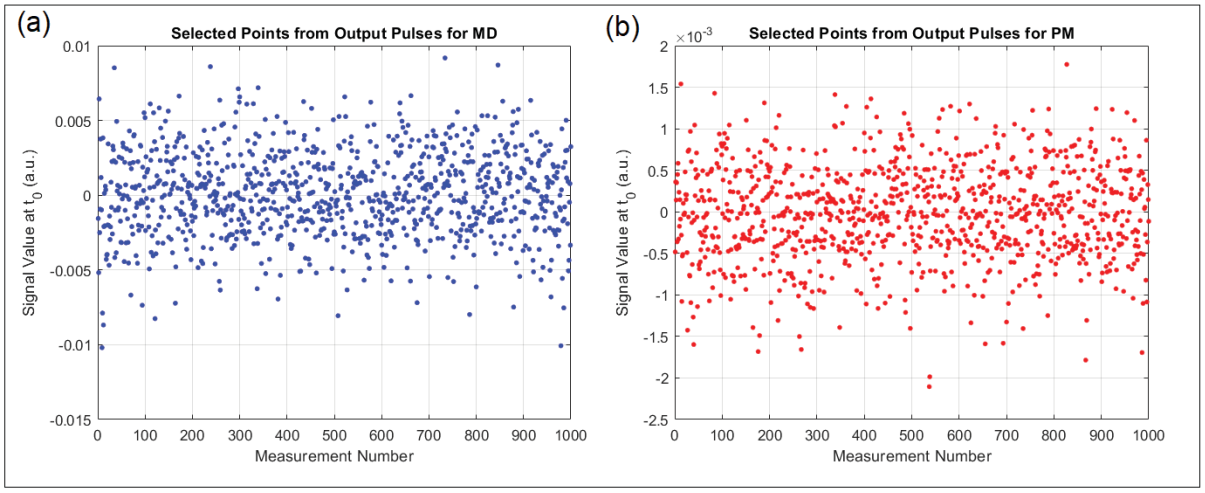

Figure 3.20 Plot of a selected point on THz input pulses mixed with jittered reference to show the impact of (a) MD's phase noise and (b) PM's phase noise

Finally, the SNR values for each of the LIA output pulses are calculated and averaged. Figure 3.22 presents the plot of SNR versus frequency, averaged for 1000 output pulses. The average calculated value shows 14 dB of SNR difference between MD and PM, highlighting the impact of MD’s higher phase noise and jitter on SNR deterioration. The calculated SNR results were presented in the previous section as well.

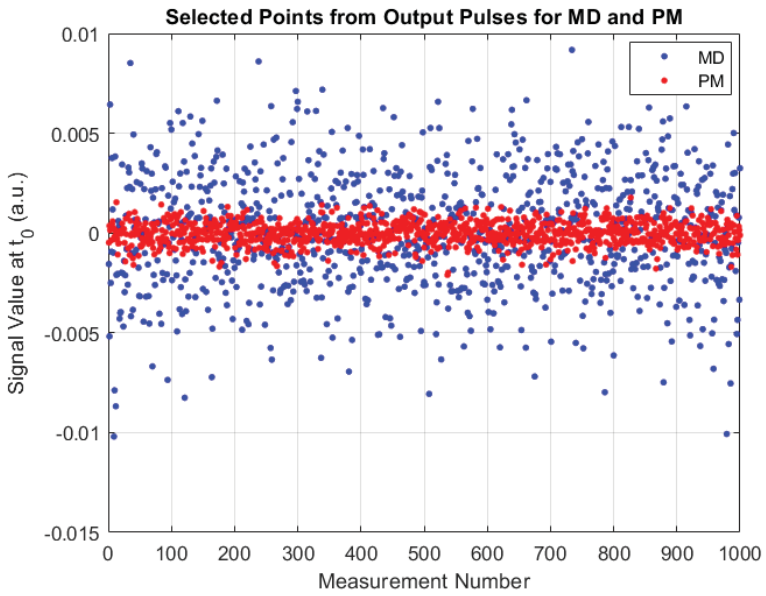

Figure 3.21 Comparing the scale of impact of MD's phase noise versus PM's phase noise on a selected point

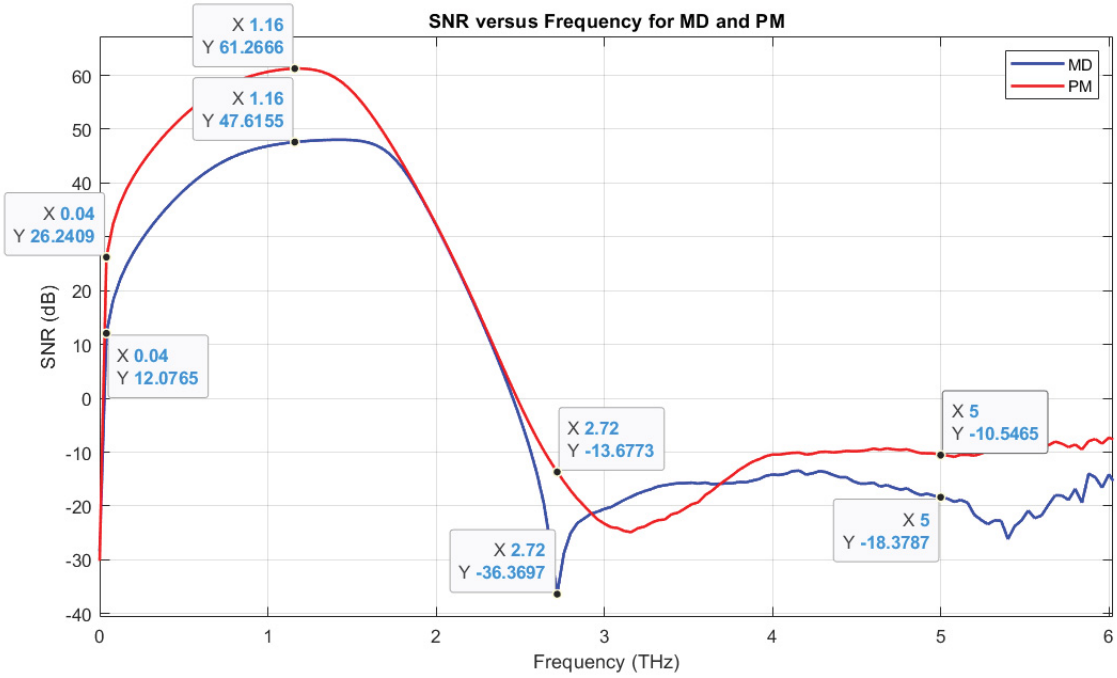

Figure 3.22 Noise in the frequency domain, highlighting the impact of MD's higher phase noise on SNR deterioration compared with PM's phase noise

Furthermore, to better visualize the impact of jitter and phase noise of both MD and PM on the THz pulse, the spectra of their experimental results are compared in Figures 3.23 and 3.24.

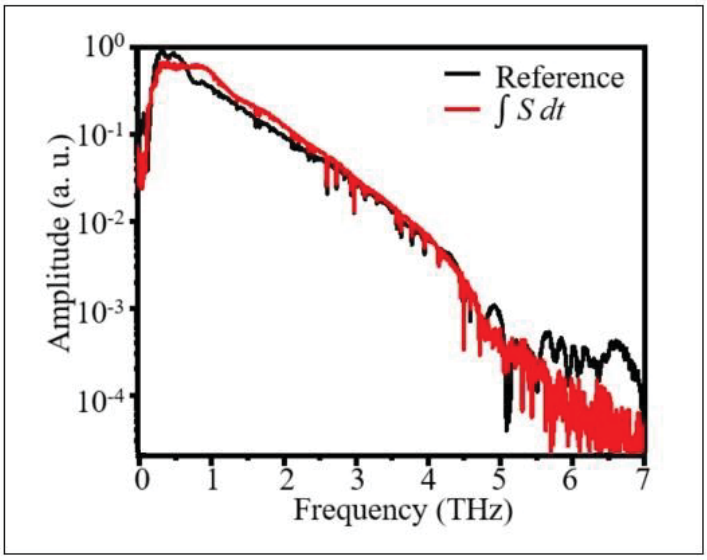

Figure 3.23 SNR improvement by integrating the derivative signal obtained from PM
Taken from (Amirkhan et al., 2021)

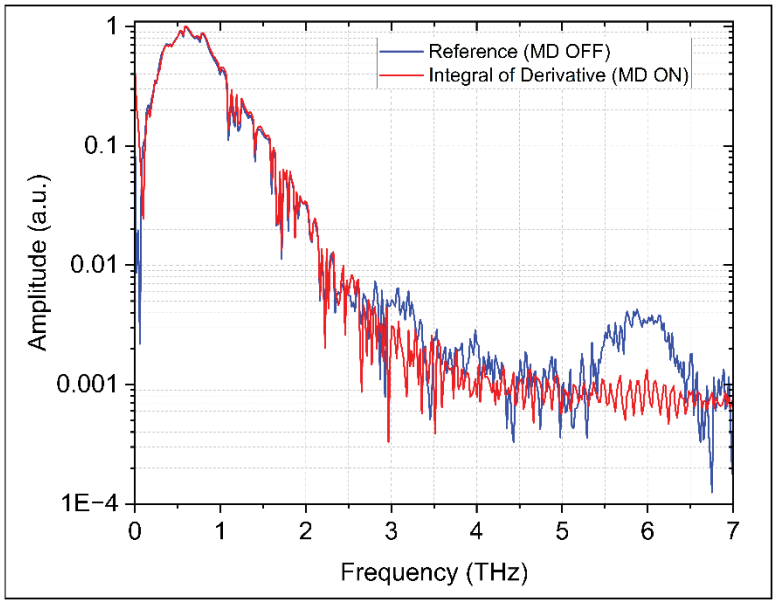

Figure 3.24 Integral of the derivative signal obtained from MD with much less SNR improvement

After integrating the derivative signal obtained from the excitation of MD and PM, it can be deduced that the SNR of the original signal is improved by PM (Amirkhan et al., 2021) as PM

has less jitter, while the SNR improvement by MD is less impactful due to its high jitter and phase noise.

3.5 Quality factor

The last parameter to evaluate the performance of MD versus PM is to calculate the quality factors of these two MEMS devices. The quality factor is dimensionless and shows how much energy is lost. It quantifies the sharpness of the resonance peak of the resonator and describes the damping of the oscillatory system. It can be formulated as (Bhugra & Piazza, 2017, p. 134):

$$Q = 2\pi \frac{peak\ energy\ stored}{energy\ dissipated\ per\ cycle} \tag{3.28}$$

As MEMS is considered as a resonator and is characterized by its frequency response, the alternative formulation based on the frequency response features is described as (Bhugra & Piazza, 2017, p. 134):

$$Q = \frac{f_0}{BW_{3dB}} \tag{3.29}$$

Where f_0 is the resonant frequency, and BW_{3dB} is the bandwidth where the amplitude is 3 dB less than the peak amplitude (Bhugra & Piazza, 2017). To compare the performance of MD and PM, a Matlab script is developed and presented in Annex VI, where the Q factors of both MEMS devices are calculated. Figures 3-25 and 3-26 present the frequency response of MD and PM, highlighting their peak amplitude and 3dB bandwidth, which helps with the calculation of the Q factor, as presented in Table 3.4. The results show that PM has a higher quality factor compared with MD.

Table 3.4 Quality factor calculation for MD and PM

	Resonance frequency (Hz)	3 dB bandwidth (Hz)	Quality factor
MD	1100.0977	0.4678	2351.44
PM	10679.9316	0.1560	68467.93

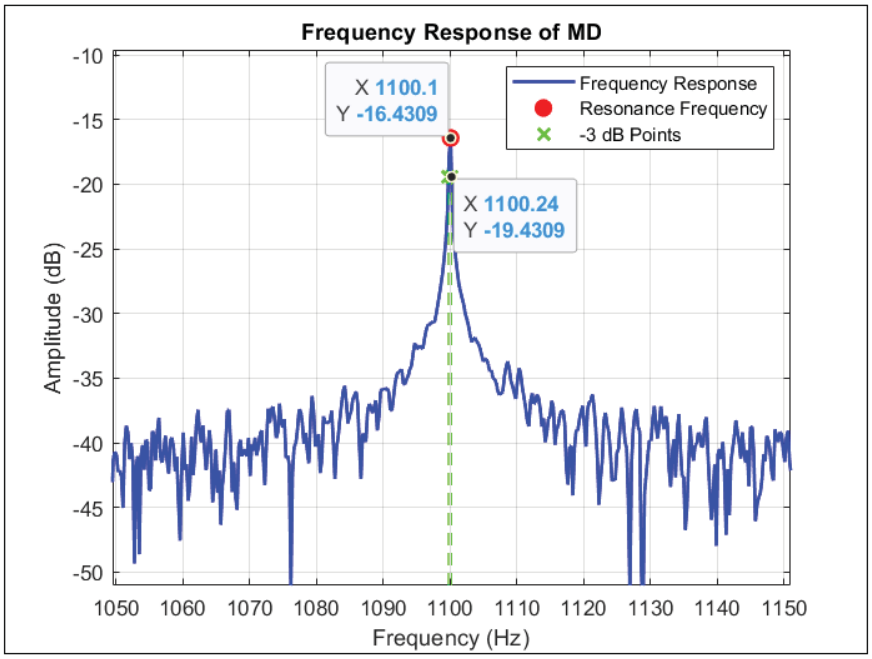

Figure 3.25 Frequency response of MD, showing its peak amplitude and 3dB bandwidth

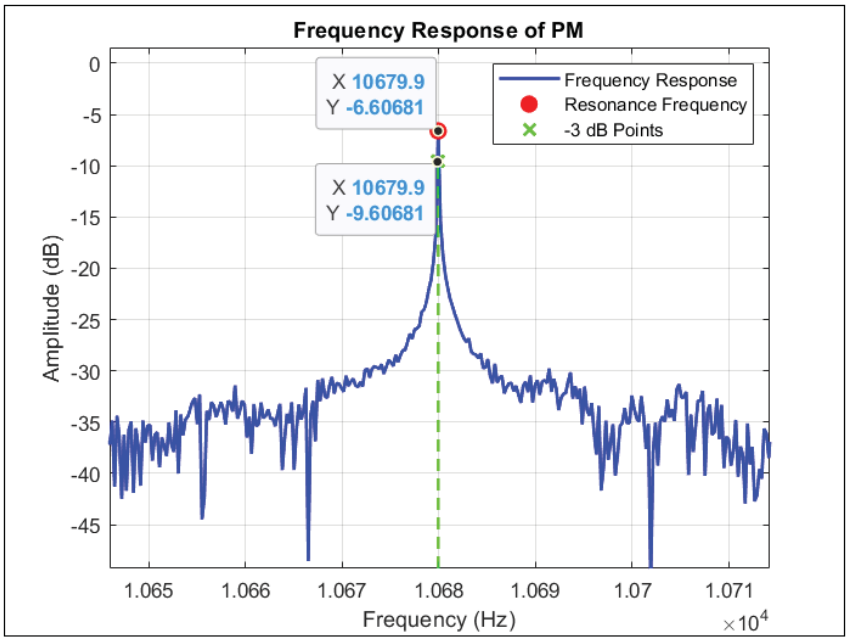

Figure 3.26 Frequency response of PM, showing its peak amplitude and 3dB bandwidth

Furthermore, based on the Leeson's equation (Equation 3.66)(*The Phase Noise Challenge Pacing the Race to 5G | 2019-11-10 | Microwave Journal*, 2019), higher quality factor means less phase noise, which corresponds to the previous calculations about MD and PM.

$$L(\Delta\omega) = 10\log\left[\frac{2FkT}{P_{sig}}\left(1+\left(\frac{f_0}{2Q\Delta f}\right)^2\right)\left(1+\frac{f_{corner}}{|\Delta f|}\right)\right] \tag{3.30}$$

Where $L(\Delta\omega)$ is phase noise in (dBc/Hz), F is a noise factor of the oscillator, k is the Boltzmann's constant, T is the absolute temperature in Kelvin, P_{sig} is signal power, f_{corner} is corner frequency, f_0 is the resonant frequency and Q is the quality factor.

Higher phase noise and jitter of MD is resulted from its lower quality factor.

3.6 Conclusion

This chapter explains the mathematical foundation of jitter, phase noise, and their relation with SNR. Then, these parameters and their impact on the THz beam are visualized using Matlab simulations and benefit from measurement data. The key finding is to understand the impact of the modulating device's jitter on the THz measurements and optical parameters. The discrepancies observed in the refractive index and absorption coefficient of materials, as presented in Chapter 2, can be explained by understanding the impact of MD's jitter as the THz beam modulator. Furthermore, the quality factor of MD and PM are calculated, and the relationship between phase noise, SNR, and quality factor is formulated. In the next chapter, the conclusions will be drawn, recommendations for future work will be provided, and the lessons learned will be shared to help continue this research.

CONCLUSION AND RECOMMENDATIONS

Conclusion

This thesis presents the concept of modulating the THz pulse using a commercial MEMS speaker (MD) by creating time-path difference in the THz beam path. The initial step is to characterize the MD, incorporate it in a pump-probe THz configuration, and verify its derivative functionality. Then, four material pellets are utilized to do THz time domain derivative spectroscopy. The results are compared against the existing literature and validated by conducting the same measurements using a commercial and highly accurate THz-TDS setup (TeraFlash Pro by Toptica). With the time-domain information from the spectroscopic setup (amplitude and phase) and applying the FFT, the frequency domain data is derived, which will be utilized to calculate the optical parameters, including the refractive index and absorption coefficient. The results present some discrepancies, which are sourced from the inaccurate behavior of the MD, due to the low quality factor, intrinsic jitter, and phase noise being added to the THz-TDDS setup. Therefore, it is crucial to characterize these sources of inaccuracies (phase variations) and figure out how they impact the SNR of the setup. It is observed that compared with the previous work (Amirkhan et al., 2021), MD has a higher oscillation amplitude (16 μm) and lower oscillation frequency (1.1 kHz), which makes it easy to detect with the lock-in amplifier. The strength of the PM (Amirkhan et al., 2021) was in being custom-designed, thus having less intrinsic jitter and higher quality factor, which resulted in 14 dB better SNR result. In addition, the integral of the derivative signal obtained by PM has better SNR compared with the reference signal, which makes it impactful in terms of SNR improvement. The strength of MD is in having a flat response over a wide range of frequencies from 0.2 to 2.2 THz, but it suffers from low SNR due to low quality factor, high jitter and phase noise caused by the inaccurate oscillation of the MD. This MD was selected to satisfy the purpose of utilizing MEMS in THz applications so that the modulating device can be easily accessible in a robust and reproducible THz setup. Knowing the weaknesses of this MD, recommendations will be presented for future work. The ultimate goal is finding a modulating device with uniform movement, flat response over a high-frequency range, resolving very low or high frequencies and having high SNR with lower jitter. If such a modulating device is to

be found commercially, and if the performance is desirable, an array of this modulating device can be designed and controlled. This array can be used in imaging applications, which can bring several benefits, such as diversity of pattern creation, easier control of the pixels in the array, simplicity of the imaging setup, and preserving the signal power. An imaging technique such as single-pixel imaging can significantly benefit from these features. In continuation to the previous efforts by (Amirkhan et al., 2021; Amirkhan, Robichaud, et al., 2020), this research was a step to pave the way for utilizing commercial MEMS in THz and identifying the critical parameters that need to be considered for the next steps, to develop a modulating array with application in THz imaging.

In this thesis, OriginPro software was utilized to create the THz wave figures using measurement data. In addition, Lumerical (Ansys) is used for finite-difference time-domain (FDTD) method simulation, as presented in Annex I.

Recommendations for future work

The modulating device that needs to be selected to modulate the THz beam and design an array for imaging applications is recommended to have the following features:

- Accessible in large quantities
- Each pixel in a few mm size so the integrated array will be in sub-cm size
- Oscillation frequency in kHz range (for easier detection by lock-in amplifier)
- Oscillation amplitude (peak-to-peak) in micrometer range (for easier detection by lock-in amplifier)
- High-quality factor and low jitter characteristics to avoid losing SNR
- Optimized design of the array to avoid cross-talk
- Optimized array control to provide efficient pattern shaping

A few candidate options, including (*AST0760MCTRQ*, 2024; *CPT-7502-65-SMT-TR Same Sky | Mouser*, 2024; *CPT-9019S-SMT-TR | Audio Transducers | Buzzers*, 2024) as shown in Figure-A.VII-1 (in Annex VII), were considered for future work. All of them are piezo buzzer transducers. Their technical specifications can be found in Table-A VII-1 (in Annex VII).

Using the Matlab script provided in Annex IV, the RMS phase jitter of these buzzers is calculated and presented in Table-A VII-2 (in Annex VII).

All of these buzzers have better RMS phase jitter compared with the MD. The next step would be to obtain their mode-shape using a Vibrometer to see if their oscillation movement is uniform and relatively flat. The one with the best oscillation mode-shape can be selected for testing in the THz-TDDS setup and to be integrated into an array for imaging purposes.

Future work

A team of PFE students, including Badr Terjani, Hanna amoud-Michel, Philippe Boivin, Raphael Desbiens, and a summer intern, Eliott Bardat, worked on designing the array of speakers and providing control on each pixel using the Matlab interface while avoiding the cross-talk. In the latest stage of their research, they used a buzzer (*AST0760MCTRQ*, 2024) and designed a printed circuit board (PCB) to connect and control the pixels and create arrays of 2×2, 4×4, and 6×6 pixels, as shown in Figure-A VII-2 (in Annex VII).

The next step of their project would be to control the matrix, starting from 2×2 and advancing to 6×6, providing the digital control over the graphical user interface (GUI) and optimizing the control and pattern shaping mechanism. Then, with a better modulating device (in terms of size, performance, and integration), a sizable array can be developed to be incorporated in the THz beam path and test the modulating functionality.

The references (Bardat, 2024; Terjani et al., 2023) are recommended for reading to learn about this project.

Lessons learned

Here are a few technical lessons I learned during the process.

- Importance of highly accurate and robust alignment and checking the alignment every time.

- Checking the input power for the emitter and detector and comply with the nominal range of them.
- Importance of correct and robust placement of the sample in the THz beam path to avoid unwanted movements, tilts, and variations.
- Importance of averaging in gaining better results. If more scans are needed, it should be done even if it is time-consuming.
- Clear file naming, which will save time and energy in identifying the results later
- Doing all measurements in one day continuously because each day, the operational and environmental parameters can change
- Time management
- Files management
- Using the purge box can enhance the results by removing the water vapor
- Understanding the settings of the lock-in amplifier. Generally, understanding how lock-in amplifier works and its incredible and strong features can help a lot.

ANNEX I

SIMULATION RESULTS

Lumerical ANSYS FDTD software is used to simulate and verify the derivative functionality of MD in THz setup. An object with the same material and dimensions as the MD is placed. Other simulation parameters are selected to mimic the THz setup. The following parameters and conditions are set for the simulation.

- Material: Aluminum (CRC)
- Material size: 1.8 mm x 1.8 mm
- Material thickness: 150 µm
- Source distance: 2500 µm
- Monitor distance: 3000 µm
- Material displacement: ± 8 µm (totally 16 µm)
- Mesh, FDTD, Source size: 1.8 mm x 1.3 mm
- Source: Gaussian
- Frequency range: 0.1 THz < f < 3 THz
- Wavelength range: 99.9 µm < λ < 2997.9 µm

Figure-A I-1 shows the simulation setup and configurations in different axes views.

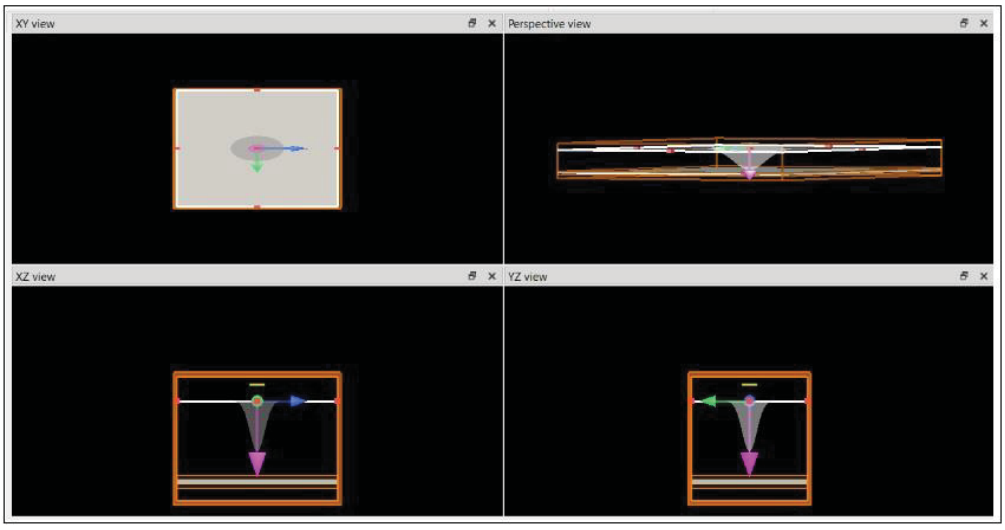

Figure-A I-1 Lumerical simulation setup and configuration

Figure-A I-2 presents the time-domain result. It shows that with a total displacement of 16 µm, the resultant signal is the derivative signal of the reference. To reach this simulation proof, the first reference is obtained at position z=0 (blue). Then, the material is placed at z_1= -8 µm and z_2=+8 µm. The difference in the result is calculated as $\Delta z = z_2 - z_1 = 16\,\mu m$ (shown in Figure with red).

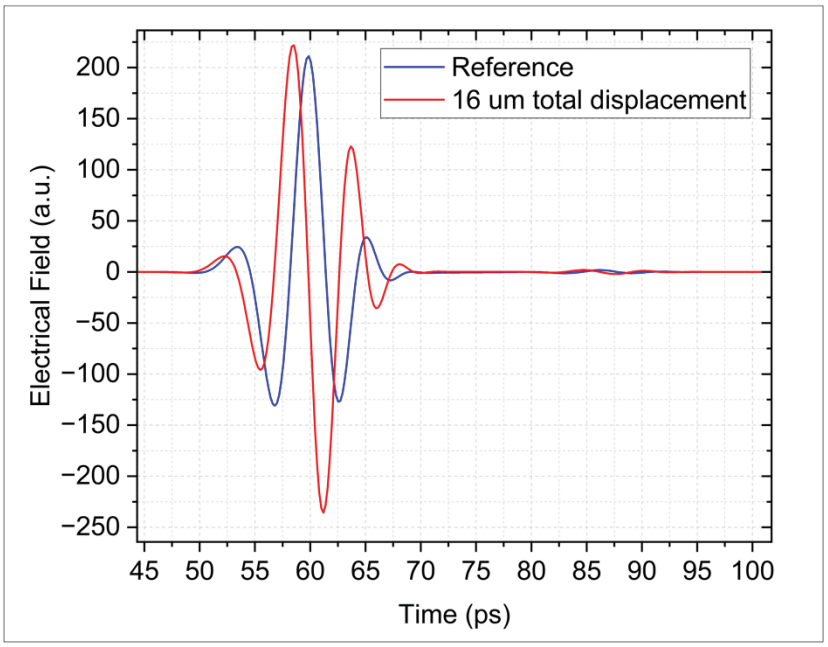

Figure-A I-2 Reference and derivative signal simulation

In the next step, the mathematical verification is done. When the reference is derivated and compared with the derivative signal, the derivative signal is integrated and compared with the reference. The results are presented in Figures-A I-3 and A I-4.

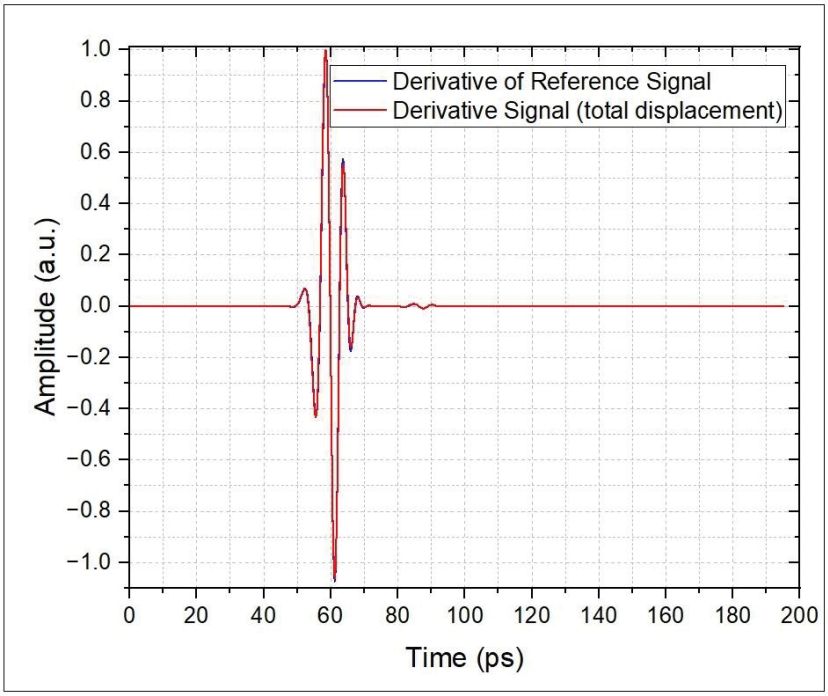

Figure-A I-3 Simulation proof by comparing the derivative of the reference with the derivative signal

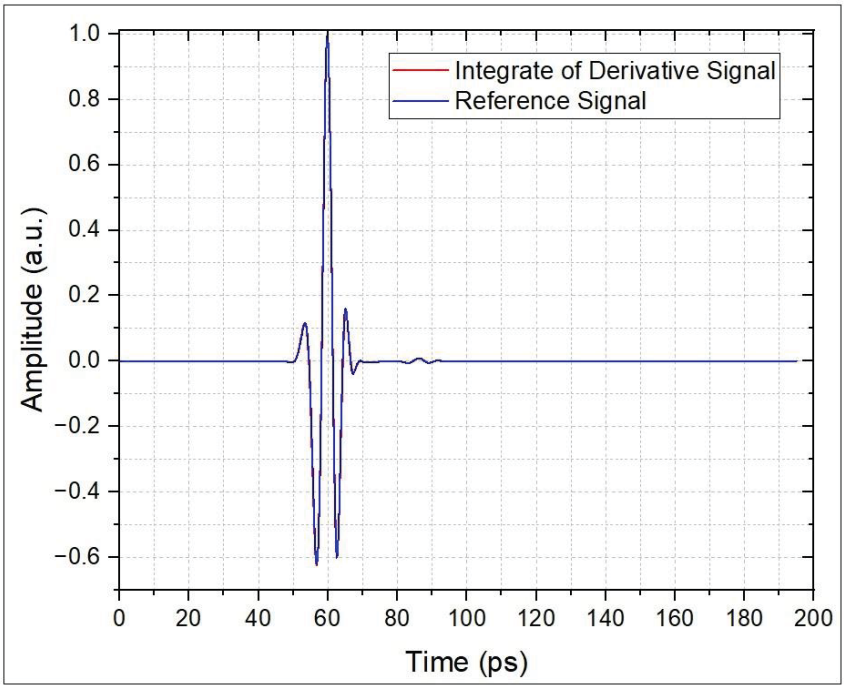

Figure-A I-4 Simulation proof by comparing the integral of the derivative signal with the reference

The same simulation results are transformed to the frequency domain by applying FFT, as shown in Figures-A I-5 and A I-6. This proves the point that if a mirror moves 16 µm in the THz beam path with the specific setup configuration and parameters, this movement can create changes in the time and path of the THz beam such that it modulates the THz beam.

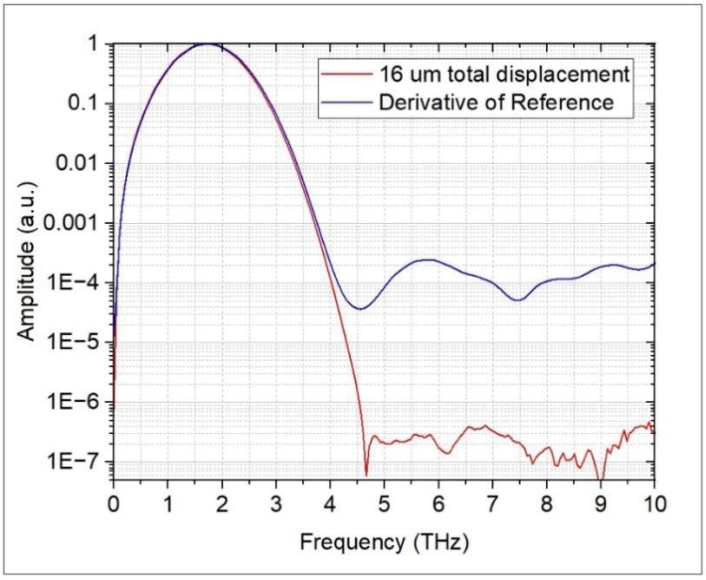

Figure-A I-5 Frequency domain comparison between the derivative signal and the derivation of the reference signal

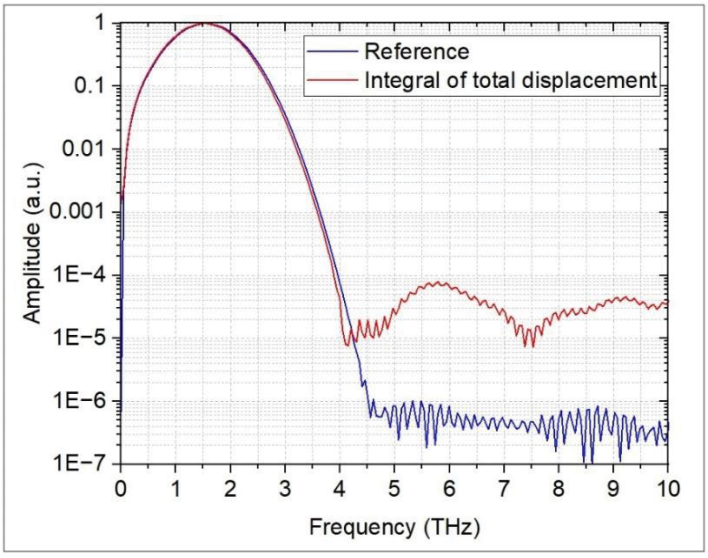

Figure-A I-6 Frequency domain comparison between the reference and the integral of the derivative signal

ANNEX II

PHASE NOISE AND JITTER IN THZ-TDS

In a THz-TDS setup, various sources of error and uncertainties affect the data and results. The measured electrical signal $S_{meas}(x)$ as a function of position *x* of the delay line is obtained by the detector. The random errors can be caused by equipment sensitivity, noise, or inaccurate definitions. Any *i* measurement of a signal can be written as [Note: all equations in this section are taken from (Coutaz et al., 2018)]:

$$S_{meas,i}(x) = S(x) + \Delta S_i(x) \tag{II.1}$$

Where $\Delta S_i(x)$ is the error as a difference between the obtained and expected true values. The best experimental estimation of the signal can be achieved by calculating the mean $\overline{S_{meas}(x)}$ of a set of measurements $S_{meas,i}(x)$ with I as the total number of measurements:

$$\overline{S_{meas}(x)} = \frac{1}{I}\sum_{i=1}^{1} S_{meas,i}(x) = S(x) + \frac{1}{I}\sum_{i=1}^{1} \Delta S_i(x) = S(x) + \overline{\Delta S(x)} \tag{II.2}$$

Based on the random nature of uncertainty in measurements, the uncertainty's mean value will approach zero by increasing the number of I measurements. Therefore,

$$\overline{\Delta S(x)}_{I\to\infty} \to 0 \quad \Rightarrow \overline{S_{meas}(x)}_{I\to\infty} = S(x) \tag{II.3}$$

The noise can be presented by its standard deviation explanation $\sigma(x)$ as:

$$\sigma^2(x) = \frac{1}{I}\sum_{i=1}^{1}(S_{meas,i}(x) - \overline{S_{meas}(x)})^2 = \frac{1}{I}\sum_{i=1}^{1}(\Delta S_i(x))^2 = \overline{\Delta S^2(x)} \tag{II.4}$$

If $\sigma(x) \ll S(x,)$ then,

$$S_{meas}(x) = S(x) \pm \sigma(x) \tag{II.5}$$

In contrast to random errors, systematic errors cannot be improved by averaging the signals obtained from numerous measurements (Pulikkoonattu, 2007). Systematic errors will not be explained in detail for the sake of conciseness of this thesis.

In THz-TDS, the determination of complex refractive index $\tilde{n}(\omega) = n(\omega) - jk(\omega)$ can be affected by some error sources such as:

- If the uncertainty is propagated in $S(x)$ in a way that $S(x) \pm \Delta S(x)$ should be considered instead of $S(x)$, there will be errors induced in the $\tilde{n}(\omega)$.
- Inaccurate modeling of the transmission or reflection of the THz pulse through or from the sample, which does not correspond to the actual THz beam shape in THz-TDS, can cause errors.
- If the information about the sample is insufficient or inaccurate, for instance, if scattering is misrepresented by absorption due to the heterogeneity of the sample at the sub-wavelength scale.
- If the computations include rounding (Coutaz et al., 2018).

Figure-A II-1 and Table-A II-1 present the classification of errors (both random and systematic) in THz-TDS (Withayachumnankul et al., 2008).

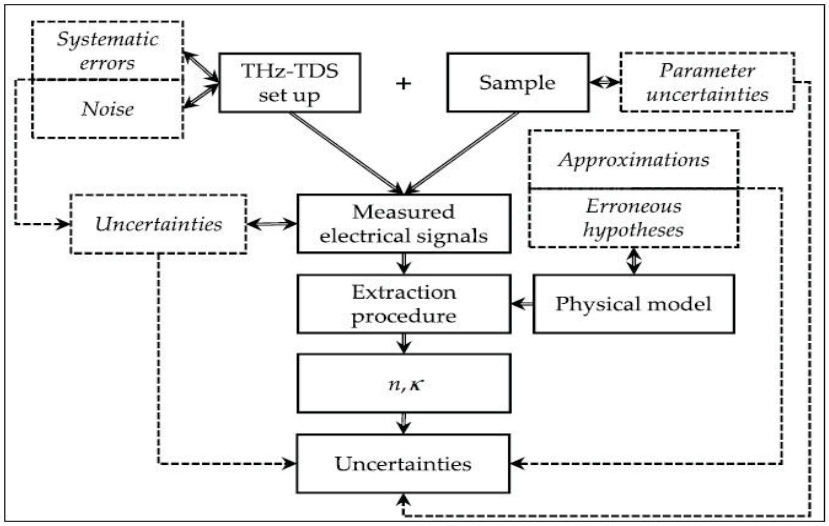

Figure-A II-1 Error sources and uncertainty types in THz-TDS
Taken from (Withayachumnankul et al., 2008)

Table-A II-1 Random and systematic errors in THz-TDS
Taken from (Withayachumnankul et al., 2008)

Electronics and optic source	Random and systematic
Sample alignment	Random or systematic
Sample thickness measurement	Random and systematic
Approximate transmission/ reflection transfer function	Systematic
Refractive index of air	Systematic
Fabry-Perot reflections in the sample	Systematic

Sources of noise in THz-TDS

Sources of noise in THz-TDS can be named as:

- The modulating device's jitter causes inaccuracies in timing and results in the phase noise in detection. This will impact the lock-in amplifier detection and the resultant SNR. In general applications, a mechanical chopper can be used to modulate the THz beam, and its mechanical inaccuracies cause phase noise. In this research, the MD (MEMS) has jitter, which, compared with the previous research (Amirkhan et al., 2021), has higher phase noise and, thus, lower SNR.
- The laser shot noise contributes to the noise in emission, which is different for photoconductive antenna or electro-optic generation. It also contributes to noise in detection.
- Perturbations in the laser beam intensity and photon noise lead to flicker noise and other laser instabilities (generally) in the form of $1/f$ where f is the frequency of the noise power's Fourier transform.
- Another source of error is the emitter's dark current due to the finite resistivity of the PCA, which can be primarily observed in the ion defect for materials with high bandgaps, such as LT-GaAs.
- The fluctuations in the laser beam pointing (direction) due to the mechanical vibrations of the laser cavity's optical parts and thermal effects can cause noise.

- The thermal background, room temperature variations, and the environment's thermal radiation affect the THz detector.
- The detector of a THz-TDS setup measures the electrical current with its intensity proportional to the THz field. The random instant motions of electrons in the conductors can cause Johnson noise in electronics (or thermal noise). Having a preamplifier (voltage or current) in lock-in amplifiers can have an input noise of a few $fA/\sqrt{Hz}$.

To summarize, Figure-A II-2 presents the noise contributions in the time domain (Coutaz et al., 2018).

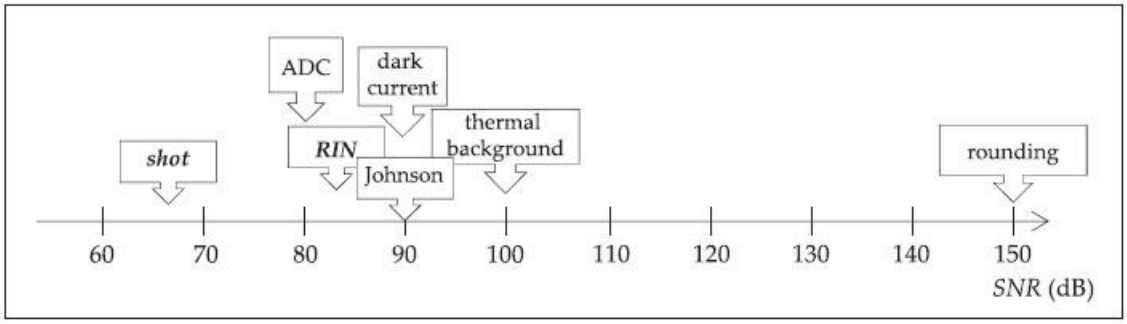

Figure-A II-2 Time domain noise contributions and their SNR values
(RIN: relative intensity noise)
Taken from (Coutaz et al., 2018)

In this research, besides all potential noise sources, the primary source comes from the MD's jitter, which causes timing inaccuracies in lock-in detection, as explained in the following section.

Phase noise in laser

The pulsed functionality of the laser can cause another type of noise, which is either a jitter or phase shift in the optical wave (compared with the pulse's envelope), varying for each pulse (or carrier envelope offset- CEO). The phase jitter $\Delta\varphi_{CEO}$ mean value is proportional to CEO frequency $f_{CEO} = \Delta\varphi_{CEO}/2\pi T_{rep}$, having T_{rep} as the pulse's repetition period. In a pump-probe THz-TDS setup, the phase variations in THz emission are compensated by detection if the setup has the same dispersion in both emitting and detecting parts.

Phase noise in THz-TDS

The delay time τ between the incoming THz pulse and the probe laser pulse at the detector contributes to the phase of the measurement spectrum. As the beam splitter has split the laser beam pulse, both the emitter and detector are excited by the same laser beam; therefore, τ depends on the following conditions:

- The optical path from the beam splitter to the emitter (pump), including the delay line
- The optical path from the beam splitter to the detector (probe)
- The THz pulse's time of flight between emitter and detector

The mechanical vibrations of the optical components in the setup and the perturbations of the optical and THz path in the air cause random variations of τ. The mechanical vibrations can be reduced by the tight installation of optical components on the optical table and by making the paths as short as possible. The perturbance of the path between the emitter and detector can be mitigated by doing the measurements in a vacuum or purging the system with dry air.

Noise effects in time and frequency domains

At delay time of τ, the detected noisy THz wave $S_{meas}(\tau)$ can be written as the sum of the true expected value $S(\tau)$ and noise $\Delta S(\tau)$ [Note: all equations in this section are taken from (Coutaz et al., 2018)]:

$$S_{meas}(\tau) = S(\tau) + \Delta S(\tau) \tag{II.6}$$

The mean value $S(\tau)$ is calculated by averaging at a specific time delay τ over a time duration or by averaging multiple detection results. Taking the Fourier transform gives the following equation:

$$S_{meas}(\omega) = \frac{1}{\sqrt{2\pi}} \int_{-\infty}^{+\infty} \big(S(\tau) + \Delta S(\tau)\big) e^{-j\omega\tau} d\tau \equiv S(\omega) + \Delta S(\omega) \tag{II.7}$$

The variance of the noisy spectra is the variance of the noise ($\bar{x}$ is the mean value of x):

$$\sigma_S^2(\omega) = \overline{|S_{meas}(\omega) - S(\omega)|^2} = \overline{|\Delta S(\omega)|^2} \tag{II.8}$$

As the number of measurements is limited, the Fourier transform in equation (3.7) cannot be over infinity; thus, it is taken from 0 to T_{record}, where T_{record} is the total measurement (recording) duration. Therefore,

$$S_{meas}(\omega) = \frac{1}{\sqrt{2\pi}}\int_0^{T_{record}} \big(S(\tau) + \Delta S(\tau)\big)e^{-j\omega\tau}d\tau \\ = \frac{1}{\sqrt{2\pi}}\int_{-\infty}^{+\infty} \big(S(\tau) + \Delta S(\tau)\big)W_{T_{record}}(\tau)e^{-j\omega\tau}d\tau \tag{II.9}$$

The recording window is described by the rectangle function of $W_{T_{record}}$ as:

$$W_{T_{record}}(\tau \in U) = 1, \quad W_{T_{record}}(\tau \notin U) = 0, \quad U = [0, T_{record}] \tag{II.10}$$

The noise out of the recording window time has an impact on the $S_{meas}(\omega)$ as:

$$S_{meas}(\omega) = \\ \frac{1}{\sqrt{2\pi}}\int_{-\infty}^{+\infty} S(\tau)e^{-j\omega\tau}d\tau + \frac{1}{\sqrt{2\pi}}\int_{-\infty}^{+\infty} \Delta S(\tau)W_{T_{record}}(\tau)e^{-j\omega\tau}d\tau \tag{II.11}$$

Knowing the Fourier transform of a product is the convolution of the Fourier transform, therefore:

$$S_{meas}(\omega) = S(\omega) + \Delta S(\omega) \otimes W_{T_{record}}(\omega) \tag{II.12}$$

$$\Rightarrow \sigma_S^2(\omega) = \overline{|S_{meas}(\omega) - S(\omega)|^2} = \overline{|\Delta S(\omega) \otimes W_{T_{record}}(\omega)|^2} \tag{II.13}$$

Having the recording window longer than the THz wave and taking the Fourier transform of the time window with the amplitude of 1 and width of $2\pi/T_{record}$ approximations, where $\Delta S(\omega)$ does unnoticeable variations, gives the following formulations:

$$\Delta S(\omega) \otimes W_{T_{record}}(\omega) \approx \frac{2\pi}{T_{record}}\Delta S(\omega) \tag{II.14}$$

$$\Rightarrow \sigma_S^2(\omega) \approx \left(\frac{2\pi}{T_{record}}\right)^2 \overline{|\Delta S(\omega)|^2}$$

$$SNR(\omega) = \left(\frac{T_{record}}{2\pi}\right)^2 \frac{|S(\omega)|^2}{\overline{|\Delta S(\omega)|^2}} \quad \text{(II.15)}$$

The first term of $\Delta S(\omega)^2$ and the variance can be estimated as (having $\tau^{"} = \tau - \tau'$) :

$$|\Delta S(\omega)|^2 = \frac{1}{2\pi}\left|\int_{-\infty}^{+\infty} \Delta S(\tau)\, e^{-j\omega\tau}\, d\tau\right|^2 \quad \text{(II.16)}$$

$$= \frac{1}{2\pi}\left|\int_{-\infty}^{+\infty}\left(\int_{-\infty}^{+\infty} \Delta S(\tau)\Delta S(\tau')\, e^{-j\omega(\tau-\tau')}\, d\tau d\tau'\right.\right|$$

$$= \frac{1}{2\pi}\left|\int_{-\infty}^{+\infty}\left(\int_{-\infty}^{+\infty} \Delta S(\tau)\Delta S\left(\tau - \tau^{"}\right)d\tau\right)\, e^{-j\omega\tau^{"}}\, d\tau^{"}\right|$$

In the above equation, the autocorrelation of noise is the integral over τ, written as:

$$\int_{-\infty}^{+\infty} \Delta S(\tau)\Delta S\left(\tau - \tau^{"}\right)d\tau = \Delta S\left(\tau^{"}\right) \otimes \Delta S\left(\tau^{"}\right) \quad \text{(II.17)}$$

$$\Rightarrow |\Delta S(\omega)|^2 = \frac{1}{2\pi}\left|\int_{-\infty}^{+\infty} \Delta S(\tau) \otimes \Delta S(\tau) e^{-j\omega t} dt\right|$$

$$= \frac{|FT[\Delta S(\tau) \otimes \Delta S(\tau)]|}{\sqrt{2\pi}}$$

Thus, the $|\Delta S(\omega)|^2$ is considered as the phase noise PSD. The PSD is constant and frequency-independent for white noise.

Temporal/spectral sampling

The measured discrete values of the time-domain signal can be obtained by the step-by-step movement of the delay line, like a sampling procedure. Therefore, discrete Fourier transform (DFT) will be utilized. If N is the recorded number of points, $\Delta\tau$ is the interval between two continuous points, and the recorded time is calculated as $T_{record} = (N-1) \times \Delta\tau$. With n as

an integer and $0 \leq n \leq N-1$, at any discrete time $\tau_n = n \times \Delta\tau$, the measured signal can be calculated as

$$S_{meas}(n\Delta\tau) \equiv S_{meas,n} \propto \int_{t=-\infty}^{+\infty} \left(E_{THz}(t) + \Delta E_{THz}(t)\right) I(t - n\Delta\tau)dt \tag{II.18}$$

Where $E_{THz}(t)$ is the THz field and $I(t)$ is the impulse response. If $I(t)$ is replaced by a rectangle function with amplitude of 1 and width δt, the first approximation is calculated as:

$$S_{meas,n} \propto \int_{t=n\Delta\tau-\frac{\delta t}{2}}^{n\Delta\tau+\frac{\delta t}{2}} \left(E_{THz}(t) + \Delta E_{THz}(t)\right) dt \tag{II.19}$$

$$\approx \delta t \times E_{THz}(n\Delta t) + \delta t \times \Delta E_{THz}(n\Delta t)$$

Or simply written

$$S_{meas,n} = S_n + \Delta S_n \tag{II.20}$$

where

$$S_n \propto \delta t \times E_{THz}(n\Delta t), \qquad \Delta S_n \propto \delta t \times \Delta E_{THz}(n\Delta t) \tag{II.21}$$

Thus, as shown in Figure-A II-3, the measured signal is a series of square pulses with various amplitudes and equally placed in the period of $\Delta\tau$.

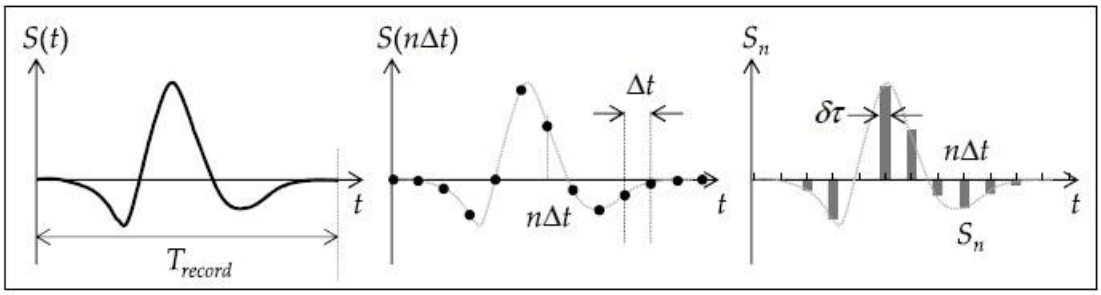

Figure-A II-3 (left) THz pulse and (right) sampled waveform
Taken from (Coutaz et al., 2018)

The measured signal is a set of N data with S_n values ($0 \le n \le N-1$) and will be Fourier transformed. The result of the Fourier transform is also a set of N discrete data (spectral data) at ω_k frequencies, presented as $\omega_k = {2\pi k}/{N\Delta\tau}$ where $0 \le k \le N-1$, formulated as:

$$S_{rec}(\omega_k) \equiv S_k = \frac{1}{\sqrt{N}} \sum_{n=0}^{N-1} S_n e^{-j\omega_k \Delta\tau n} = \frac{1}{\sqrt{N}} \sum_{n=0}^{N-1} S_n e^{-j2\pi k \frac{n}{N}} = \sum_{n=0}^{N-1} S_{n,k} \qquad \text{(II.22)}$$

Here, n refers to the time domain, and k refers to frequency-domain formulations. Here, the definitions of S_n and S_k are reciprocal; thus, if ${1}/{\sqrt{N}}$ in the above formula is removed, ${1}/{N}$ is used in the S_n series expression.

In practice, when the time interval is very short Δτ, the spectral spreads up to a maximum frequency of $f_{max} = {1}/{\Delta\tau}$. In another observation, it is noticed that the spectral points' magnitude varies by $\sqrt{N}$ value.

Temporal sampling noise

Considering the random noise gives the following equations:

$$S_{meas,n} = S_n + \Delta S_n \qquad \text{(II.23)}$$
$$\Rightarrow S_n = \frac{1}{I} \sum_{i=1}^{I} S_{meas,n,i}$$
$$\Rightarrow \sigma_n^2 = \overline{\Delta S_n^2} = \frac{1}{I} \sum_{i=1}^{I} \Delta S_{n,i}^2$$

Where I is the number of measurements that $S_{n,i}$ provides at $n\Delta\tau$ delay time. The temporal sample S_n of the THz signal can be calculated by integrating the detected signal during the detector's impulse response time. As the Chameleon femtosecond laser with 100 MHz repetition rate was used for this project, this laser produces repetitive pulses. The THz signal was detected by Zurich Instrument lock-in amplifier (LIA) with the frequency of $f_{LIA} = {1}/{\Delta t_{LIA}}$. The lock-in locks on the modulating frequency of f_{LIA} to modulate the THz beam. In this project, if lock-in locks on the emitter's modulator, then $f_{LIA} = 10\ kHz$, and if locks on

the MD, then $f_{LIA} = 1.1\ kHz$. In general practice, a mechanical or electronic chopper can be used. In this case, the integration time of the lock-in amplifier is longer than the Δt_{LIA}, and the delay between two continuous laser pulses is Δt_{rep}. Therefore, the signal detected by the lock-in amplifier is the sum of the detected signal over laser pulses P, calculated as P=(2×Δt_{rep}), where $^1/_2$ coefficient is for the chopper. Thus:

$$S_{LIA,meas,n} = \sum_{p=1}^{P} S_{mean,n,p} \tag{II.24}$$
$$\Rightarrow S_{LIA,n} = P \times S_n$$
$$\Delta S_{LIA,n} = \sum_{p=1}^{P} \Delta S_{n,p}$$

For each pulse P detected by the LIA, if the noise is not correlated with the noise of the other pulses, the noise's random behavior, considering the central limit theorem, is calculated by:

$$\overline{\Delta S_{LIA,n}} = \frac{1}{\sqrt{P}} \overline{\Delta S_n} \tag{II.25}$$
$$SNR_{LIA,n} = \left(\frac{S_{LIA,n}}{\overline{\Delta S_{LIA,n}}} \right)^2 = P$$

A laser generally has flicker noise $^1/_f$ with characteristic time relative to the lock-in amplifier's integration time. Considering a general condition of $^1/_{f^\alpha}$ noise (α as a real number), the variance would relatively be:

$$|\Delta S(\omega)|^2 \propto \frac{A}{\omega^\alpha} \tag{II.26}$$
$$\Rightarrow\ \sigma^2 = A\, C(\alpha) T_{LIA}^{1+\alpha}$$

where $C(\alpha) = (2^{2+\alpha} - 2^{1+2\alpha})\pi^{\alpha-1}\Gamma(-1-\alpha)\sin\left(\frac{\alpha\pi}{2}\right)$, having Γ as the gamma function. Therefore,

$$\overline{\Delta S_{LIA,n}} = \frac{1}{P^{\sqrt{1+\alpha}}}\overline{\Delta S_n} \tag{II.27}$$

$$SNR_{LIA,n} = \left(\frac{S_{LIA,n}}{\overline{\Delta S_{LIA,n}}}\right)^2 = P^{(1-\alpha)}$$

It can be deduced that when $\alpha > 1$ for flicker noise, the lock-in amplifier's SNR decreases with the increase of P, thus increasing the T_{LIA}. If the recorded pulses go to infinity, the random noise of each temporal sample (n) will go to zero, as the random noise of the temporal sample is proportional to the inverse square root of the recorded pulses. Based on the relation between T_{LIA} and P, it can be deduced that short T_{LIA} gives an extended spread spectrum to high frequencies; thus, the noise is weak. If integrated over all frequencies, the mean noise will be small thanks to the contribution of the high frequencies. With longer T_{LIA} that involves lower frequencies, the mean noise value will be more considerable. Therefore, it is recommended to take several measurements over a short lock-in amplifier integration time and average them rather than measuring over long T_{LIA}. From now on, $S_n = S_{LIA,n}$ as temporal samples, and ${\sigma_n}^2 = {\sigma_{LIA,n}}^2$ as their variances measured by the lock-in amplifier will be considered.

Spectral samples' noise

Calculating the Fourier transform provides the following equation as spectral data:

$$S_{meas,k} = \frac{1}{\sqrt{N}}\sum_{n=0}^{N-1} S_{meas,n}\, e^{-j\frac{2\pi k}{N}n} \tag{II.28}$$

$$\Rightarrow\ S_{meas,k} = \frac{1}{\sqrt{N}}\sum_{n=0}^{N-1} S_n\, e^{-j\frac{2\pi k}{N}n} + \frac{1}{\sqrt{N}}\sum_{n=0}^{N-1} \Delta S_n\, e^{-j\frac{2\pi k}{N}n} = S_k + \Delta S_k \tag{II.29}$$

The sum of random values of ΔS_k gives the noise. As the noise of temporal data n acts randomly, with N a large enough number of data, based on the central limit theorem, the ΔS_k is also random with Gaussian distribution. The "periodogram" or the variance for each spectral segment is calculated as:

$$\sigma_k^2 = \overline{\left|S_{meas,k} - S_k\right|^2} = \overline{|\Delta S_k|^2} = \frac{1}{N}\overline{\left|\sum_{n=0}^{N-1} \Delta S_n\, e^{-J\frac{2\pi k}{N}n}\right|^2} = \frac{1}{I}\sum_{i=0}^{I}\frac{1}{N}\overline{\left|\sum_{n=0}^{N-1} \Delta S_{n,i}\, e^{-J\frac{2\pi k}{N}n}\right|^2} \quad \text{(II.30)}$$

$$\Rightarrow \sigma_k^2 = \frac{1}{N}\left|\sum_{n=0}^{N-1}\sum_{p=0}^{N-1} \overline{\Delta S_n \Delta S_p}\; e^{-j\frac{2\pi k}{N}n}\; e^{-j\frac{2\pi k}{N}p}\right|$$

By having $n' = n + p$:

$$\sigma_k^2 = \frac{1}{N}\left|\sum_{n=0}^{N-1}\sum_{n'=n}^{n+N-1} \overline{\Delta S_n \Delta S_{n'-n}}\; e^{-j\frac{2\pi k}{N}n'}\right| \quad \text{(II.31)}$$

Which is the autocorrelation of the discrete noise values. For Gaussian white noise when $\overline{\Delta S_n{}^2} = \sigma_n^2$, the above term is simplified as:

$$\sigma_k^2 = \frac{N}{2}\sigma_n^2 \quad \text{(II.32)}$$

This shows the relationship between spectral discrete data and temporal data's variance.

To sum up, the magnitude of THz spectra in the frequency domain is affected by the noise proportional to the THz signal or signal-independent noise. The shot noise mainly causes the signal-dependent noise. Therefore, the standard deviation of the noise is smaller than THz signal's PSD. The signal-independent noise affects the dynamic range of the THz-TDS. The phase variation in the spectral region is a few percent, whereas the noise is several times smaller than the magnitude of the THz signal. Otherwise, in other regions, the noise causes random phase jumps of one or a few π when the phase noise increases (Coutaz et al., 2018).

ANNEX III

MATLAB SCRIPT FOR THE RELATION BETWEEN JITTER AND SNR

Here is the script to simulate the relationship between jitter, phase noise, and SNR of an ideal signal. The jitter and phase noise are mathematically modeled. The results are presented in Figures 3.7- 3.9.

JITTER AND SNR RELATIONSHIP AND CALCULATIONS:

```
% ========================================================================
% MATLAB Script: Relation between jitter and SNR
% Behnoosh Meskoob
%
% ========================================================================
% Parameters
Fs = 1e13;  % Sampling frequency (10 THz)
t = 0:1/Fs:10e-12;  % Time vector
f_thz = 1e12;  % THz signal frequency (1 THz)
sigma = 0.7e-12;  % Gaussian width (0.7 ps)
modulation_indices = linspace(0, 0.08, 16);  % Modulation index range
noise_amplitude = 1 ;  % Amplitude of noise signal (controls jitter)

% Generate the reference Gaussian-modulated THz signal
generate_reference_signal = @(t, sigma, f_thz) exp(-((t - 5.0e-12) /
sigma) .^ 2) .* sin(2 * pi * f_thz * t);
reference_signal = generate_reference_signal(t, sigma, f_thz);

% Apply jitter (phase modulation) to the THz Gaussian-modulated signal
add_jitter_to_signal = @(t, sigma, f_thz, modulation_index, noise_signal)
    exp(-((t - 5.0e-12) / sigma) .^ 2) .* sin(2 * pi * f_thz * t +
modulation_index * noise_signal);

% Calculate SNR (in dB) between reference and jittered signals
calculate_snr = @(reference_signal, jittered_signal) ...
    10 * log10(mean(reference_signal .^ 2) / std((reference_signal -
jittered_signal) .^ 2));
% Main execution
SNR_values = zeros(1, length(modulation_indices));
jittered_signals = cell(1, length(modulation_indices));

% Generate jittered signals and calculate SNR
for i = 1:length(modulation_indices)
    modulation_index = modulation_indices(i);
    noise_signal = noise_amplitude * randn();
    % Approximate the signal through averaging (Monte Carlo approach)
```

```
    n = 10000;
    jittered_signal_sum = zeros(1, length(t));
    for j = 1:n
        jittered_signal_sum = jittered_signal_sum +
add_jitter_to_signal(t, sigma, f_thz, modulation_index, noise_signal);
    end
    jittered_signal = jittered_signal_sum / n;

    SNR_values(i) = calculate_snr(reference_signal, jittered_signal);
    jittered_signals{i} = jittered_signal;
end
% Plot results
plot_signals(t, reference_signal, jittered_signals, modulation_indices);
plot_frequency_domain(t, Fs, reference_signal, jittered_signals,
modulation_indices);
plot_snr_vs_modulation(modulation_indices, SNR_values);

% Plot time-domain signals: Reference vs Jittered
function plot_signals(t, reference_signal, jittered_signals,
modulation_indices)
    figure;
    plot(t * 1e12, reference_signal, 'b', 'LineWidth', 1.5);
    hold on;
    colors = jet(length(modulation_indices));
    for i = 1:length(jittered_signals)
        plot(t * 1e12, jittered_signals{i}, 'Color', colors(i,:),
'LineWidth', 1.2);
    end
    xlabel('Time (ps)');
    ylabel('Electrical Field (a.u.)');
    title('Reference vs Jittered THz Pulses');
    legend(['Reference', arrayfun(@(mi) sprintf('Jittered (mi=%.3f)',
mi), modulation_indices, 'UniformOutput', false)]);
    grid on;
    hold off;
end
% Plot frequency-domain signals (FFT): Reference vs Jittered
function plot_frequency_domain(t, Fs, reference_signal, jittered_signals,
modulation_indices)
    figure;
    N = length(t);
    f = Fs * (0:(N / 2)) / N;  % Frequency vector
    % FFT of reference signal
    fft_reference = fft(reference_signal);
    fft_reference_mag = abs(fft_reference / N);
    fft_reference_mag = fft_reference_mag(1:N/2+1);
    fft_reference_mag(2:end-1) = 2 * fft_reference_mag(2:end-1);
    semilogy(f * 1e-12, fft_reference_mag, 'b', 'LineWidth', 1.5);
    hold on;
    colors = jet(length(modulation_indices));
```

```
    for i = 1:length(jittered_signals)
        fft_jittered = fft(jittered_signals{i});
        fft_jittered_mag = abs(fft_jittered / N);
        fft_jittered_mag = fft_jittered_mag(1:N/2+1);
        fft_jittered_mag(2:end-1) = 2 * fft_jittered_mag(2:end-1);
        semilogy(f * 1e-12, fft_jittered_mag, 'Color', colors(i,:),
'LineWidth', 1.2);
    end

    xlabel('Frequency (THz)');
    ylabel('Magnitude (a.u.)');
    title('Reference vs Jittered THz Pulses');
    legend(['Reference', arrayfun(@(mi) sprintf('Jittered (mi=%.3f)',
mi), modulation_indices, 'UniformOutput', false)]);
    grid on;
    hold off;
end

% Plot SNR as a function of modulation index
function plot_snr_vs_modulation(modulation_indices, SNR_values)
    figure;
    plot(modulation_indices, SNR_values, '-o', 'LineWidth', 1.5,
'MarkerSize', 8, 'MarkerFaceColor', 'r');
    xlabel('Modulation Index (Jitter Severity)');
    ylabel('SNR (dB)');
    title('SNR vs Jitter Severity for THz Pulse');
    grid on;
end


%
================================================================================
% End of Script
%
================================================================================
```

ANNEX IV

MATLAB SCRIPT TO CALCULATE PHASE NOISE, JITTER, AND SNR

This script utilizes the data obtained from Vibrometer and calculates the oscillation amplitude of MD, its jitter, and phase noise. Then, the experimental data from THz-TDS setup is loaded so the phase jitter can be added to it and observe its impact on SNR. The results are presented in Figures 3.11-3.21.

PHASE NOISE, JITTER, AND SNR CALCULATIONS:

```
%
================================================================================
% MATLAB Script: Power Spectrum, Phase Noise, FFT Mag, Phase noise PSD,
SNR
% Behnoosh Meskoob
%
================================================================================

clear all
close all
clc

% 1. Load Data and Calculate Phase Noise and Jitter of MD
% Load data file
load('Speaker_1100Hz_20Vpp.mat')
proper_size_signal=2048000;
te1=t(2);
Sampling_frequency1=1/te1;
L1=proper_size_signal;
f1=Sampling_frequency1/L1*(0:(L1/2));
t(proper_size_signal+1:end)=[];
speed(proper_size_signal+1:end)=[];
voltage(proper_size_signal+1:end)=[];

Y_speed = fft(speed);
P2_speed = abs(Y_speed/L1);
P1_speed = P2_speed(1:L1/2+1);
P1_speed(2:end-1) = 2*P1_speed(2:end-1);

P1_MD_db = pow2db(P1_speed); %speed is for MD- frequency domain signal of
MD in dB
```

```
% FFT for voltage

Y_voltage = fft(voltage);
P2_voltage = abs(Y_voltage/L1);
P1_voltage = P2_voltage(1:L1/2+1);
P1_voltage(2:end-1) = 2*P1_voltage(2:end-1);

P1_FuncGen1_db = pow2db(P1_voltage); %voltage is for function generator

rbw=1;
FrOffset1 = [2.5 10 100 1e3 2.5e3 5e3 10e3 15e3 100e3]; % frequency
offset
%single sided phase noise levels calculation from frequency domain
signal and plot it
PN_MD = phaseNoiseMeasure(f1,P1_MD_db,rbw,FrOffset1,'on','Phase noise');
PN_FuncGen1 =
phaseNoiseMeasure(f1,P1_FuncGen1_db,rbw,FrOffset1,'on','Phase noise');

offset_phase_noise1=70;
PN_MD=PN_MD-offset_phase_noise1;
PN_FuncGen1=PN_FuncGen1-offset_phase_noise1;

figure()
hold all
plot(f1,P1_speed,'b-*')
xlim([1085,1115])
xlabel('Frequency (Hz)');
ylabel('FFT Magnitude');
legend('MD')
title('FFT Magnitude of MD')
grid on;

figure()
hold all
plot(f1,P1_voltage,'r-*')
xlim([900,1200])
xlabel('Frequency (Hz)');
ylabel('FFT Magnitude');
legend('MD','Function Generator1')
title('FFT Magnitude of MD')
grid on;
figure()
hold all
plot(FrOffset1,PN_MD, 'LineWidth', 2)
plot(FrOffset1,PN_FuncGen1, 'LineWidth', 2)
xlabel('Frequency (Hz)');
ylabel('PSD (dBc/Hz)');
legend('MD','Function Generator1')
title('Phase Noise Power Spectral Density in dB for MD')
grid on;
xlim([0 1e4])
```

```
figure()
semilogx(FrOffset1,PN_MD, 'LineWidth', 2)
hold on
semilogx(FrOffset1,PN_FuncGen1, 'LineWidth', 2)
xlabel('Frequency (Hz)');
ylabel('PSD (dBc/Hz)');
legend('MD','Function Generator1')
title('Phase Noise Power Spectral Density in dB for MD')
grid on;
xlim([0 1e5])

% jitter
frequency1 =1100;
[Jrms_rad_MD,Jrms_deg_MD, Jrms_s_MD]  =
phaseNoiseToJitter(FrOffset1,PN_MD,'Frequency',frequency1)
[Jrms_rad_FuncGen1,Jrms_deg_FuncGen1, Jrms_s_FuncGen1]  =
phaseNoiseToJitter(FrOffset1,PN_FuncGen1,'Frequency',frequency1)

% Display calculated jitter values for MEMS
fprintf('MEMS RMS Jitter:\n');
fprintf('  Jrms_rad_MD = %.4e radians\n', Jrms_rad_MD);
fprintf('  Jrms_s_MD = %.4e seconds\n', Jrms_s_MD);

fprintf('  Jrms_rad_FG = %.4e radians\n', Jrms_rad_FuncGen1);
fprintf('  Jrms_s_FG = %.4e seconds\n', Jrms_s_FuncGen1);

% 2. Load Data and Calculate Phase Noise and Jitter of PM
% Load data file
load('MEMS_fatemeh_10680Hz_20Vpp.mat')
proper_size_signal2=2048000;
te=t(2);
Sampling_frequency2=1/te;
L2=proper_size_signal2;
f=Sampling_frequency2/L2*(0:(L2/2));
t(proper_size_signal2+1:end)=[];
speed(proper_size_signal2+1:end)=[];
voltage(proper_size_signal2+1:end)=[];

Y_speed2 = fft(speed);
P2_speed2 = abs(Y_speed2/L2);
P1_speed2 = P2_speed2(1:L2/2+1);
P1_speed2(2:end-1) = 2*P1_speed2(2:end-1);

P1_PM_db = pow2db(P1_speed2); %speed is for PM

Y_voltage2 = fft(voltage);
P2_voltage2 = abs(Y_voltage2/L2);
P1_voltage2 = P2_voltage2(1:L2/2+1);
P1_voltage2(2:end-1) = 2*P1_voltage2(2:end-1);
P1_FuncGen2_db=pow2db(P1_voltage2); %voltage is for function generator
```

```
rbw=1;
FrOffset2 = [2.5 10 100 1e3 5e3 10e3 12e3 15e3 100e3];
PN_PM = phaseNoiseMeasure(f,P1_PM_db,rbw,FrOffset2,'on','Phase noise');
PN_FuncGen2 =
phaseNoiseMeasure(f,P1_FuncGen2_db,rbw,FrOffset2,'on','Phase noise');

offset_phase_noise2=80;
PN_PM=PN_PM-offset_phase_noise2;
PN_FuncGen2=PN_FuncGen2-offset_phase_noise2;

figure()
hold all
plot(f,P1_speed2,'b-*')
xlim([10665,10695])
xlabel('Frequency (Hz)');
ylabel('FFT Magnitude');
legend('PM')
title('FFT Magnitude of PM')
grid on;

figure()
hold all
plot(f,P1_speed2,'b-*')
plot(f,P1_voltage2,'r-*')
xlim([8000,12000])
xlabel('Frequency (Hz)');
ylabel('FFT Magnitude');
legend('PM','Function Generator1')
title('FFT Magnitude of PM')
grid on;

figure()
hold all
plot(FrOffset2,PN_PM, 'LineWidth', 2)
plot(FrOffset2,PN_FuncGen2, 'LineWidth', 2)
xlabel('Frequency (Hz)');
ylabel('PSD (dBc/Hz)');
legend('PM','Function Generator1')
title('Phase Noise Power Spectral Density in dB for PM')
grid on;
xlim([0 1.5e4])
figure()
semilogx(FrOffset2,PN_PM,'LineWidth', 2)
hold on
semilogx(FrOffset2,PN_FuncGen2,'LineWidth', 2)
xlabel('Frequency (Hz)');
ylabel('PSD (dBc/Hz)');
legend('PM','Function Generator1')
title('Phase Noise Power Spectral Density in dB for PM')
grid on;
xlim([0 1e5])
```

```
% comparison between MD vs. PM
figure()
semilogx(FrOffset1,PN_MD, 'LineWidth', 2)
hold on
semilogx(FrOffset2,PN_PM,'LineWidth', 2)
semilogx(FrOffset2,PN_FuncGen2,'LineWidth', 2)


xlabel('Frequency (Hz)');
ylabel('PSD (dBc/Hz)');
legend('MD','PM','Function Generator')
title('Phase Noise Power Spectral Density for MD and PM')
grid on;
xlim([0 1e5])

figure()
semilogx(FrOffset2,PN_PM,'LineWidth', 2)
hold on
semilogx(FrOffset1,PN_MD, 'LineWidth', 2)
xlabel('Frequency (Hz)');
ylabel('PSD (dBc/Hz)');
legend('PM','MD')
title('Phase Noise Power Spectral Density in dB for MD and PM')
grid on;
xlim([0 1e5])

% jitter
frequency2=10680;
[Jrms_rad_PM,Jrms_deg_PM, Jrms_s_PM]  =
phaseNoiseToJitter(FrOffset2,PN_PM,'Frequency',frequency2)
[Jrms_rad_FuncGen2,Jrms_deg_FuncGen2, Jrms_s_FuncGen2]  =
phaseNoiseToJitter(FrOffset2,PN_FuncGen2,'Frequency',frequency2)

% Display calculated jitter values for MEMS
fprintf('MEMS RMS Jitter:\n');
fprintf('  Jrms_rad_PM = %.4e radians\n', Jrms_rad_PM);
fprintf('  Jrms_s_PM = %.4e seconds\n', Jrms_s_PM);
fprintf('  Jrms_rad_FuncGen2 = %.4e radians\n', Jrms_rad_PM);
fprintf('  Jrms_s_FuncGen2 = %.4e seconds\n', Jrms_s_PM);

% 3. Import the THz Pulse Data from Excel for reference and derivative
excel_file1 = 'ref_membrane.xlsx'; % Reference THz pulse
data1 = readmatrix(excel_file1); % Reference THz pulse
% Extract time and electric field values
t_ps = data1(:, 1);       % Time in picoseconds
g_original = data1(:, 2); % Electric field values

% Convert time to seconds
t = t_ps * 1e-12; % Convert picoseconds to seconds
```

```
% Ensure time vector is sorted and unique
[t, unique_indices] = unique(t);
g_original = g_original(unique_indices);

% 4. Simulate Pulses with Measured Phase Jitter
% Set random seed for reproducibility
rng(0);

% Number of pulses to simulate
M = 1000;

% Preallocate matrix to store pulses
G_pulses_MD = zeros(length(t), M);
G_pulses_PM = zeros(length(t), M);

% Use MD RMS jitter
Jrms_rad1 = Jrms_rad_MD; % RMS phase jitter in radians

% Generate M pulses with phase jitter added
for n = 1:M
    % Generate random phase jitter for each pulse
    delta_phi_n = randn * Jrms_rad1; % Phase jitter in radians

    % Get the analytic signal
    analytic_signal = hilbert(g_original);

    % Apply phase shift
    g_n = real(analytic_signal .* exp(1i * delta_phi_n));

    % Store the pulse
    G_pulses_MD(:, n) = g_n;
end

% Calculate the mean signal over all pulses
mean_g_MD = mean(G_pulses_MD, 2);

% 5. Calculate Variance and SNR Numerically
% Calculate variance (noise power) over all pulses
var_g_MD = var(G_pulses_MD, 0, 2);

% Calculate standard deviation
std_g_MD = sqrt(var_g_MD);

%for the PM
rng(0); % Reset random seed for consistency

Jrms_rad2 = Jrms_rad_PM; % RMS phase jitter in radians for PM
```

```
for n = 1:M
    delta_phi_n = randn * Jrms_rad2;
    analytic_signal = hilbert(g_original);
    g_n = real(analytic_signal .* exp(1i * delta_phi_n));
    G_pulses_PM(:, n) = g_n;
end

% Calculate mean and variance for PM
mean_g_PM = mean(G_pulses_PM, 2);
var_g_PM = var(G_pulses_PM, 0, 2);
std_g_PM = sqrt(var_g_PM);

% Compute total signal power and noise power using energy (integral over
time)
signal_power_MD = trapz(t, mean_g_MD.^2);
noise_power_MD = trapz(t, var_g_MD);

% Calculate SNR_MD
SNR_total_MD = signal_power_MD / noise_power_MD;
SNR_dB_MD = 10 * log10(SNR_total_MD);

signal_power_PM = trapz(t, mean_g_PM.^2);
noise_power_PM = trapz(t, var_g_PM);

% Calculate SNR_PM
SNR_total_PM = signal_power_PM / noise_power_PM;
SNR_dB_PM = 10 * log10(SNR_total_PM);

% 6. SNR vs. RMS Phase Jitter Plot
% Define a range of jitter values
max_jitter = max(Jrms_rad_MD, Jrms_rad_PM);
jitter_values_rad1 = linspace(0, 1.5 * Jrms_rad_MD, 50);
jitter_values_rad2 = linspace(0, 1.5 * Jrms_rad_PM, 50);

% Preallocate array for SNR values
SNR_dB_values_MD = zeros(size(jitter_values_rad1));
SNR_dB_values_PM = zeros(size(jitter_values_rad2));

% Loop over jitter values
for idx = 1:length(jitter_values_rad1)
    Jrms_rad_current = jitter_values_rad1(idx);

    % Reset random seed for consistency
    rng(0); % Ensure consistency across runs
    % Generate M pulses with current phase jitter
    for n = 1:M
        delta_phi_n = randn * Jrms_rad_current;
        analytic_signal = hilbert(g_original);
        g_n = real(analytic_signal .* exp(1i * delta_phi_n));
        G_pulses_MD(:, n) = g_n;
    end
```

```
 % Calculate mean and variance
    mean_g = mean(G_pulses_MD, 2);
    var_g = var(G_pulses_MD, 0, 2);

    % Compute signal and noise power
    signal_power = trapz(t, mean_g.^2);
    noise_power = trapz(t, var_g);

    % Calculate SNR
    SNR_total = signal_power / noise_power;
    SNR_dB_values_MD(idx) = 10 * log10(SNR_total);
end

% Loop over jitter values for PM
for idx = 1:length(jitter_values_rad2)
    Jrms_rad_current = jitter_values_rad2(idx);
    rng(0); % Ensure consistency across runs
    for n = 1:M
        delta_phi_n = randn * Jrms_rad_current;
        analytic_signal = hilbert(g_original);
        g_n = real(analytic_signal .* exp(1i * delta_phi_n));
        G_pulses_PM(:, n) = g_n;
    end
    mean_g = mean(G_pulses_PM, 2);
    var_g = var(G_pulses_PM, 0, 2);
    signal_power = trapz(t, mean_g.^2);
    noise_power = trapz(t, var_g);
    SNR_total = signal_power / noise_power;
    SNR_dB_values_PM(idx) = 10 * log10(SNR_total);
end

% Plot SNR vs. RMS Phase Jitter
figure;

plot(jitter_values_rad1, SNR_dB_values_MD, 'b-', 'LineWidth', 2); hold
on;
%yyaxis right
SNR_at_calculated_jitter_MD = interp1(jitter_values_rad1,
SNR_dB_values_MD, Jrms_rad_MD);
plot(Jrms_rad_MD, SNR_at_calculated_jitter_MD, 'bo', 'MarkerSize', 8,
'LineWidth', 2);

plot(jitter_values_rad2, SNR_dB_values_PM, 'm-', 'LineWidth', 2); hold
on;
% Mark the calculated RMS jitter value
SNR_at_calculated_jitter_PM = interp1(jitter_values_rad2,
SNR_dB_values_PM, Jrms_rad_PM);
plot(Jrms_rad_PM, SNR_at_calculated_jitter_PM, 'mo', 'MarkerSize', 8,
'LineWidth', 2);

xlabel('RMS Phase Jitter (radians)');
ylabel('SNR (dB)');
title('SNR vs. RMS Phase Jitter for MD and PM');
```

```
grid on;
legend('SNR MD', 'Measured RMS Jitter MD','SNR PM', 'Measured RMS Jitter
PM');

% Display the SNR at the measured jitter value
fprintf('\nSNR at measured phase jitter for MD (%.4e radians): %.2f
dB\n', Jrms_rad_MD, SNR_dB_MD);
fprintf('\nSNR at measured phase jitter for PM (%.4e radians): %.2f
dB\n', Jrms_rad_PM, SNR_dB_PM);

%
================================================================================
% End of Script
%================================================================================
```

ANNEX V

LOCK-IN AMPLIFIER FUNCTIONALITY SIMULATION

This Matlab script, simulates the functionality of a lock-in amplifier as explained in section 3.4. The results are presented in Figures 3.18-3.22.

LOCK-IN AMPLIFIER SIMULATION TO INVESTIGATE JITTER IMPACT:

```
% ========================================================================
% MATLAB Script: Lock-In Amplifier Simulation with MEMS Jitter
% Behnoosh Meskoob
% ========================================================================

% Clear workspace and close all figures
clear; close all; clc;

% 0. Set Random Seed for Reproducibility
rng(0); % Set the random seed to a fixed value

% 1. Measure the jitter and phase noise of MD and PM
% RMS phase jitter values (provided from ANNEX4)
Jrms_rad_MD = 3.8704e-3; % radians (MD has higher jitter)
Jrms_rad_PM = 7.7046e-4; % radians (PM has lower jitter)

% Display the RMS phase jitter values
fprintf('MD RMS Phase Jitter:\n');
fprintf('  Jrms_rad_MD = %.4e radians\n\n', Jrms_rad_MD);

fprintf('PM RMS Phase Jitter:\n');
fprintf('  Jrms_rad_PM = %.4e radians\n\n', Jrms_rad_PM);

% 2. Add the phase jitter to the reference of lock-in amplifier
% Reference Signal Parameters
reference_frequency = 0.5e12; % Reference frequency (0.5 THz)
Ar = 1;                       % Reference amplitude

% Time Parameters
fsample = 50e12;              % Sampling frequency (50 THz) to capture
maxima and minima
T = 25e-12;                   % Total time (25 picoseconds)
dt = 1 / fsample;             % Time step
t = 0 : dt : T - dt;          % Time vector starting from zero
N = length(t);                % Number of samples
```

```
% 3. Generate 1000 Gaussian THz pulses as input signals
% THz Pulse Parameters
pulse_width = 0.5e-12;  % Pulse width (0.5 picoseconds)
As = 1;                 % Signal amplitude (maximum amplitude is 1)
f_THz = 0.5e12;         % Central frequency of the THz pulse (0.5 THz)

% Generate a Gaussian-modulated sinusoidal THz pulse
THz_pulse = As * exp(-((t - T/2) / pulse_width).^2) .* cos(2 * pi * f_THz
* (t - T/2));

% Number of measurements
num_measurements = 1000;

% Preallocate array for THz measurements using single precision
THz_measurements = repmat(single(THz_pulse'), 1, num_measurements);

% Plot the first 10 THz pulses
figure;
plot(t * 1e12, THz_measurements(:, 1:10));
xlabel('Time (ps)');
ylabel('Amplitude (a.u.)');
title('Simulated THz Measurements (First 10 Pulses)');
grid on;

% 4. Process the signals through the lock-in amplifier
% Low-Pass Filter Parameters
LPF_cutoff = 1e12; % Low-pass filter cutoff frequency (1 THz)
[b, a] = butter(4, LPF_cutoff / (fsample / 2)); % 4th-order Butterworth
filter

% Time index for selecting the same point from each output pulse
t0 = T/2;                % Time point (center of the pulse)
t_index = find(t >= t0, 1); % Index corresponding to t0

% Preallocate arrays for outputs
lockin_outputs_MD = zeros(length(t), num_measurements, 'single');
selected_points_MD = zeros(1, num_measurements, 'single');

lockin_outputs_PM = zeros(length(t), num_measurements, 'single');
selected_points_PM = zeros(1, num_measurements, 'single');


% 5. Process Measurements for MD
% Function to generate phase noise time series given RMS jitter
generate_phase_noise = @(sigma_phi, N) sigma_phi * randn(1, N);
```

```
for n = 1:num_measurements
    % ----------------------------
    % Generate Reference Signal with Phase Noise (MD)
    % ----------------------------
    delta_phi_MD = generate_phase_noise(Jrms_rad_MD, 1); % Single random
phase offset
    R_t_MD = Ar * cos(2 * pi * reference_frequency * t + delta_phi_MD);

    % ----------------------------
    % Lock-In Amplifier Operation (MD)
    % ----------------------------
    % Multiply input signal and reference signal (mixing)
    mixer_output_MD = THz_measurements(:, n) .* R_t_MD';

    % Apply low-pass filter
    V_out_MD = filtfilt(b, a, mixer_output_MD);

    % Store the lock-in amplifier output
    lockin_outputs_MD(:, n) = V_out_MD;

    % ----------------------------
    % Select the same point from each output pulse
    % ----------------------------
    selected_points_MD(n) = V_out_MD(t_index);
end

% 6. Process Measurements for PM
for n = 1:num_measurements
    % ----------------------------
    % Generate Reference Signal with Phase Noise (PM)
    % ----------------------------
    delta_phi_PM = generate_phase_noise(Jrms_rad_PM, 1); % Single random
phase offset
    R_t_PM = Ar * cos(2 * pi * reference_frequency * t + delta_phi_PM);

    % ----------------------------
    % Lock-In Amplifier Operation (PM)
    % ----------------------------
    mixer_output_PM = THz_measurements(:, n) .* R_t_PM';

    % Apply low-pass filter
    V_out_PM = filtfilt(b, a, mixer_output_PM);

    % Store the lock-in amplifier output
    lockin_outputs_PM(:, n) = V_out_PM;
    % ----------------------------
    % Select the same point from each output pulse
    % ----------------------------
    selected_points_PM(n) = V_out_PM(t_index);
end
```

```
% 7. Plot the selected points from the output pulses
% ----------------------------
% Plot Lock-In Amplifier Outputs (First 10 Pulses) for MD
% ----------------------------
figure;
plot(t * 1e12, lockin_outputs_MD(:, 1:10));
xlabel('Time (ps)');
ylabel('LIA Output Voltage (a.u.)');
title('Lock-In Amplifier Outputs (First 10 Pulses) for MD');
grid on;

% ----------------------------
% Plot Lock-In Amplifier Outputs (First 10 Pulses) for PM
% ----------------------------
figure;
plot(t * 1e12, lockin_outputs_PM(:, 1:10));
xlabel('Time (ps)');
ylabel('LIA Output Voltage (a.u.)');
title('Lock-In Amplifier Outputs (First 10 Pulses) for PM');
grid on;

% ----------------------------
% Plot Selected Points for MD
% ----------------------------
figure;
plot(1:num_measurements, selected_points_MD, 'b.', 'MarkerSize', 10);
xlabel('Measurement Number');
ylabel('Signal Value at t_0 (a.u.)');
title('Selected Points from Output Pulses for MD');
grid on;

figure;
plot(1:num_measurements, selected_points_MD, 'b.', 'MarkerSize', 10);
hold on
%
% ----------------------------
% Plot Selected Points for PM
% ----------------------------
plot(1:num_measurements, selected_points_PM, 'r.', 'MarkerSize', 10);
xlabel('Measurement Number');
ylabel('Signal Value at t_0 (a.u.)');
title('Selected Points from Output Pulses for MD and PM');
legend ('MD','PM');
grid on;

figure;
plot(1:num_measurements, selected_points_PM, 'r.', 'MarkerSize', 10);
xlabel('Measurement Number');
ylabel('Signal Value at t_0 (a.u.)');
title('Selected Points from Output Pulses for PM');
grid on;
```

```
% 8. Calculate mean and standard deviation
% Calculate percentage variation for MD
mean_value_MD = mean(selected_points_MD);
std_value_MD = std(selected_points_MD);

% Calculate percentage variation for PM
mean_value_PM = mean(selected_points_PM);
std_value_PM = std(selected_points_PM);

% ----------------------------
% Display the Results
% ----------------------------
fprintf('Selected Point Statistics for MD:\n');
fprintf('  Mean Value = %.4e\n', mean_value_MD);
fprintf('  Standard Deviation = %.4e\n', std_value_MD);

fprintf('Selected Point Statistics for PM:\n');
fprintf('  Mean Value = %.4e\n', mean_value_PM);
fprintf('  Standard Deviation = %.4e\n', std_value_PM);

% 9. Calculate the Average SNR of the 1000 THz Pulses for MD and PM
% ----------------------------
% Calculate SNR for MD
% ----------------------------
% Compute the mean signal across all pulses (expected signal)
mean_signal_MD = mean(lockin_outputs_MD, 2);
% Compute the noise (difference from mean signal)
noise_MD = lockin_outputs_MD - mean_signal_MD;
% Calculate signal power (mean square of the mean signal)
signal_power_MD = mean(mean_signal_MD.^2);
% Calculate noise power (mean square of the noise)
noise_power_MD = mean(mean(noise_MD.^2, 1));
% Calculate SNR in dB for MD
SNR_MD = 10 * log10(signal_power_MD / mean(noise_power_MD));
% ----------------------------
% Calculate SNR for PM
% ----------------------------
% Compute the mean signal across all pulses (expected signal)
mean_signal_PM = mean(lockin_outputs_PM, 2);
% Compute the noise (difference from mean signal)
noise_PM = lockin_outputs_PM - mean_signal_PM;

% Calculate signal power (mean square of the mean signal)
signal_power_PM = mean(mean_signal_PM.^2);

% Calculate noise power (mean square of the noise)
noise_power_PM = mean(mean(noise_PM.^2, 1));

% Calculate SNR in dB for PM
SNR_PM = 10 * log10(signal_power_PM / mean(noise_power_PM));
```

```
% ----------------------------
% Display Average SNR Values
% ----------------------------
fprintf('Average SNR for MD: %.2f dB\n', SNR_MD);
fprintf('Average SNR for PM: %.2f dB\n', SNR_PM);

% 10. Calculate the FFT of Each THz Pulse and Plot Spectra for MD and PM
% ----------------------------
% For MD
% ----------------------------

% spectra amplitudes (a.u.) for the first 10 pulses

for n = 1:10
    % Compute FFT of the nth output pulse
    Y_MD = fft(lockin_outputs_MD(:, n));
    % Compute the two-sided spectrum
    P2_MD = abs(Y_MD / N);
    % Single-sided spectrum
    P1_MD = P2_MD(1:N/2+1);
    P1_MD(2:end-1) = 2 * P1_MD(2:end-1);
    % Plot the amplitude spectrum
    f = fsample * (0:(N/2)) / N;
end

% ----------------------------
% For PM
% ----------------------------

% spectra amplitudes (a.u.) for the first 10 pulses

for n = 1:10
    % Compute FFT of the nth output pulse
    Y_PM = fft(lockin_outputs_PM(:, n));
    % Compute the two-sided spectrum
    P2_PM = abs(Y_PM / N);
    % Single-sided spectrum
    P1_PM = P2_PM(1:N/2+1);
    P1_PM(2:end-1) = 2 * P1_PM(2:end-1);
    % Plot the amplitude spectrum
    f = fsample * (0:(N/2)) / N;

end

% 11. Plot SNR Values for MD and PM for Each Pulse
% Initialize arrays to store SNR values for each pulse
SNR_values_MD = zeros(1, num_measurements);
SNR_values_PM = zeros(1, num_measurements);
```

```
% Calculate SNR for each pulse
for n = 1:num_measurements
    % MD
    signal_power_pulse_MD = mean(lockin_outputs_MD(:, n).^2);
    noise_power_pulse_MD = mean((lockin_outputs_MD(:, n) -
mean_signal_MD).^2);
    SNR_values_MD(n) = 10 * log10(signal_power_pulse_MD /
noise_power_pulse_MD);

    % PM
    signal_power_pulse_PM = mean(lockin_outputs_PM(:, n).^2);
    noise_power_pulse_PM = mean((lockin_outputs_PM(:, n) -
mean_signal_PM).^2);
    SNR_values_PM(n) = 10 * log10(signal_power_pulse_PM /
noise_power_pulse_PM);
end

% 12. Calculate and Plot SNR (dB) versus Frequency (THz)
% ----------------------------
% Compute FFTs of Lock-In Outputs for MD and PM
% ----------------------------

% Initialize arrays to store FFTs
Y_MD = zeros(N, num_measurements);
Y_PM = zeros(N, num_measurements);

for n = 1:num_measurements
    % MD
    Y_MD(:, n) = fft(lockin_outputs_MD(:, n));

    % PM
    Y_PM(:, n) = fft(lockin_outputs_PM(:, n));
end

% Compute Mean FFTs (Signal) for MD and PM
mean_Y_MD = mean(Y_MD, 2);
mean_Y_PM = mean(Y_PM, 2);

% Compute Noise FFTs (Difference from Mean)
noise_Y_MD = Y_MD - mean_Y_MD;
noise_Y_PM = Y_PM - mean_Y_PM;

% Compute Signal Power and Noise Power at each frequency bin
signal_power_MD = abs(mean_Y_MD).^2;
signal_power_PM = abs(mean_Y_PM).^2;
noise_power_MD = mean(abs(noise_Y_MD).^2, 2);
noise_power_PM = mean(abs(noise_Y_PM).^2, 2);

% Avoid division by zero
noise_power_MD(noise_power_MD == 0) = eps;
noise_power_PM(noise_power_PM == 0) = eps;
```

```
% Compute SNR in dB for each frequency bin
SNR_vs_freq_MD = 10 * log10(signal_power_MD ./ noise_power_MD);
SNR_vs_freq_PM = 10 * log10(signal_power_PM ./ noise_power_PM);

% Frequency vector
f_vector = fsample * (0:(N-1)) / N;
N_half = N/2 + 1;
f_vector_half = f_vector(1:N_half);
SNR_vs_freq_MD_half = SNR_vs_freq_MD(1:N_half);
SNR_vs_freq_PM_half = SNR_vs_freq_PM(1:N_half);

% Plot SNR versus Frequency for MD and PM
figure;
plot(f_vector_half / 1e12, SNR_vs_freq_MD_half, 'b', 'LineWidth', 1.5);
hold on;
plot(f_vector_half / 1e12, SNR_vs_freq_PM_half, 'r', 'LineWidth', 1.5);
xlabel('Frequency (THz)');
ylabel('SNR (dB)');
title('SNR versus Frequency for MD and PM');
legend('MD', 'PM');
grid on;
hold off;

%
================================================================================
% End of Script
%
================================================================================
```

ANNEX VI

MATLAB SCRIPT TO CALCULATE QUALITY FACTOR

This script utilizes the data obtained from Vibrometer and calculates the quality factor of MD, and PM based on their frequency response. The results are presented in Figures 3.24-3.25 and Table 3.5.

QUALITY FACTOR CALCULATION:

```
 ========================================================================
% MATLAB Script: Q factor calculations for PM and MD
% Behnoosh Meskoob%
========================================================================
% Load the data
load('Speaker_1100Hz_20Vpp.mat');
% Convert the speed and voltage data to decibels
P1_MEMS_db = pow2db(P1_speed);    % Speed is for MEMS
P1_FuncGen_db = pow2db(P1_voltage); % Voltage is for function generator
frequency = f;
amplitude = P1_MEMS_db;
% Find the resonance frequency (frequency at maximum amplitude)
[maxAmplitude, idx_max] = max(amplitude);
f0 = frequency(idx_max);

% Calculate the amplitude at -3 dB point (3 dB less than maximum
amplitude)
amp_3dB = maxAmplitude - 3; % in dB

% Find frequencies where amplitude crosses the -3 dB level
crossing_indices = find((amplitude(1:end-1) >= amp_3dB & amplitude(2:end)
<= amp_3dB) | ...
                        (amplitude(1:end-1) <= amp_3dB & amplitude(2:end)
>= amp_3dB));

% Initialize array to hold the frequencies at which amplitude equals
amp_3dB
f_crossings = [];

% For each crossing, interpolate to find the exact frequency
for i = 1:length(crossing_indices)
    idx = crossing_indices(i);
    f1 = frequency(idx);
    f2 = frequency(idx+1);
    a1 = amplitude(idx);
    a2 = amplitude(idx+1);
```

```
    % Linear interpolation to find frequency at which amplitude equals
amp_3dB
    f_cross = f1 + (amp_3dB - a1)*(f2 - f1)/(a2 - a1);
    f_crossings = [f_crossings; f_cross];
end
% Find the frequencies below and above f0
frequencies_below = f_crossings(f_crossings < f0);
frequencies_above = f_crossings(f_crossings > f0);
if isempty(frequencies_below) || isempty(frequencies_above)
    error('Could not find -3 dB points on both sides of the resonance
frequency.');
end
f1 = max(frequencies_below);
f2 = min(frequencies_above);
% Calculate delta f (bandwidth at -3 dB points)
delta_f = f2 - f1;
% Calculate Q-factor
Q = f0 / delta_f;
% Display the results
fprintf('Resonance frequency (f0): %.4f Hz\n', f0);
fprintf('-3 dB frequencies: f1 = %.4f Hz, f2 = %.4f Hz\n', f1, f2);
fprintf('Bandwidth (delta_f): %.4f Hz\n', delta_f);
fprintf('Quality Factor (Q): %.4f\n', Q);
% plot the frequency response and mark the points
figure;
plot(frequency, amplitude, 'b-', 'LineWidth', 1.5);
hold on;
plot(f0, maxAmplitude, 'ro', 'MarkerSize', 8, 'MarkerFaceColor', 'r');
plot([f1 f2], [amp_3dB amp_3dB], 'gx', 'MarkerSize', 8, 'LineWidth', 1.5);
line([f1 f1], [min(amplitude) amp_3dB], 'Color', 'g', 'LineStyle', '--');
line([f2 f2], [min(amplitude) amp_3dB], 'Color', 'g', 'LineStyle', '--');
xlabel('Frequency (Hz)');
ylabel('Amplitude (dB)');
title('Frequency Response of MD');
legend('Frequency Response', 'Resonance Frequency', '-3 dB Points');
grid on;
hold off;
%
================================================================================
% End of Script
%================================================================================
```

ANNEX VII

FUTURE WORKS

In conclusion and recommendations, three new candidates for modulating device (*AST0760MCTRQ*, 2024; *CPT-7502-65-SMT-TR Same Sky | Mouser*, 2024; *CPT-9019S-SMT-TR | Audio Transducers | Buzzers*, 2024) are introduced. Figure-A VII-1 presents these devices.

Figure-A VII-1 Options for modulating device (*AST0760MCTRQ*, 2024; *CPT-7502-65-SMT-TR Same Sky | Mouser*, 2024; *CPT-9019S-SMT-TR | Audio Transducers | Buzzers*, 2024)

The technical specifications of these buzzers are presented in Table-A VII-1 as follows:

Table-A VII-1 Technical specifications of the piezo buzzer transducers

Part number	Size (mm × mm × mm)	Total oscillation amplitude (peak-to-peak) (µm)	Oscillation frequency (Hz)	Voltage (peak-to-peak) (v)
AST0760MCTRQ	7.5×7.5×2	48	7650	20
CPT-9019S-SMT-TR	9×9×1.9	48	4995	20
CPT-7502-65-SM-TR	7.5×7.5×2	36	7630	20

Using the Matlab script provided in Annex III, the RMS phase jitter of these buzzers is calculated and presented in Table-A VII-2.

Table-A VII-2 RMS phase jitter calculation results for buzzers

	RMS phase jitter (rad)	**RMS phase jitter (sec)**
	(AST0760MCTRQ)	
Buzzer	9.5127×10^{-4}	1.9791×10^{-8}
Function Generator	2.9730×10^{-4}	6.1853×10^{-9}
	(CPT-9019S-SMT-TR)	
Buzzer	1.4973×10^{-3}	4.7709×10^{-8}
Function Generator	2.3407×10^{-4}	7.4582×10^{-9}
	(CPT-7502-65-SM-TR)	
Buzzer	1.3374×10^{-3}	2.7896×10^{-8}
Function Generator	2.8031×10^{-4}	5.8471×10^{-9}

As mentioned in Conclusion, future works, A team of PFE students and a summer intern, Eliott Bardat, worked on designing the array of speakers. They used a buzzer (*AST0760MCTRQ*, 2024) and designed a PCB to connect and control the pixels and create arrays of 2×2, 4×4, and 6×6 pixels, as shown in Figure-A VII-2.

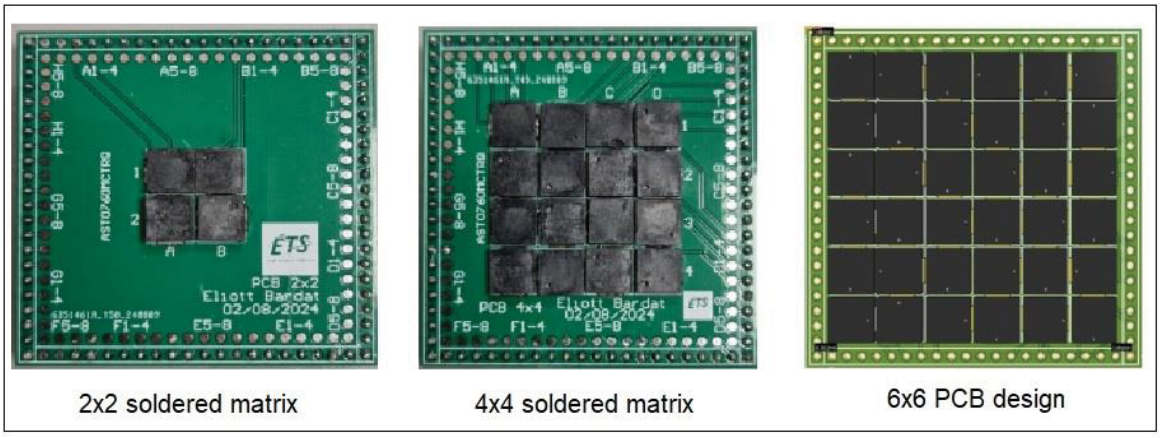

Figure-A VII-2 The designed arrays of buzzers
Taken from (Bardat, 2024; Terjani et al., 2023)

LIST OF BIBLIOGRAPHICAL REFERENCES

Akalin, T., & Treizebré, A. (2006). *Microspectroscopy with Terahertz bioMEMS* (H. Ürey & A. El-Fatatry, Eds.; p. 61860E). https://doi.org/10.1117/12.662966

Alves, F., Grbovic, D., & Karunasiri, G. (2014). Investigation of microelectromechanical systems bimaterial sensors with metamaterial absorbers for terahertz imaging. *Optical Engineering*, *53*(9), 097103–097103.

Alves, F., Grbovic, D., Kearney, B., & Karunasiri, G. (2012). Microelectromechanical systems bimaterial terahertz sensor with integrated metamaterial absorber. *Optics Letters*, *37*(11), 1886–1888.

Alves, F., Pimental, L., Grbovic, D., & Karunasiri, G. (2018). MEMS terahertz-to-infrared band converter using frequency selective planar metamaterial. *Scientific Reports*, *8*(1), 12466. https://doi.org/10.1038/s41598-018-30858-z

Amirkhan, F. (2021). *Development of novel metrology methods for time domain THz spectroscopy systems*.

Amirkhan, F., Gratuze, M., Ropagnol, X., Ozaki, T., Nabki, F., & Blanchard, F. (2020). *Terahertz differentiator using a piezoelectric micromachined device*. 2020 45th International Conference on Infrared, Millimeter, and Terahertz Waves (IRMMW-THz).

Amirkhan, F., Gratuze, M., Ropagnol, X., Ozaki, T., Nabki, F., & Blanchard, F. (2021). Terahertz time-domain derivative spectrometer using a large-aperture piezoelectric micromachined device. *Opt Express*, *29*(14), 22096–22107. https://doi.org/10.1364/OE.428106

Amirkhan, F., Robichaud, A., Ropagnol, X., Gratuze, M., Ozaki, T., Nabki, F., & Blanchard, F. (2020). Active terahertz time differentiator using piezoelectric micromachined ultrasonic transducer array. *Optics Letters*, *45*(13), 3589. https://doi.org/10.1364/OL.393917

Anthonys, G. (2022). *Timing Jitter in Time-of-Flight Range Imaging Cameras*. Springer International Publishing. https://doi.org/10.1007/978-3-030-94159-8

Anwar, M., Grbovic, D., Dhar, N. K., Karunasiri, G., & Crowe, T. W. (2009). *Fabrication of Bi-material MEMS detector arrays for THz imaging*. Terahertz Physics, Devices, and Systems III: Advanced Applications in Industry and Defense.

Arzeno, N. M., Poon, C.-S., & Deng, Z.-D. (2006). Quantitative Analysis of QRS Detection Algorithms Based on the First Derivative of the ECG. *2006 International Conference of the IEEE Engineering in Medicine and Biology Society*, 1788–1791. https://doi.org/10.1109/IEMBS.2006.260051

AST0760MCTRQ. (2024). DigiKey Electronics. https://www.digikey.ca/en/products/detail/mallory-sonalert-products-inc/AST0760MCTRQ/11567566

Balistreri, G., Tomasino, A., Dong, J., Yurtsever, A., Stivala, S., Azaña, J., & Morandotti, R. (2021). Time-Domain Integration of Broadband Terahertz Pulses in a Tapered Two-Wire Waveguide. *Laser & Photonics Reviews*, *15*(8), 2100051. https://doi.org/10.1002/lpor.202100051

Bardat, E. (2024). *Fabrication et Contrôle Automatisé de Matrices de Speakers sur Circuit Imprimé*.

Béliveau, L.-P. (2022a). *Développement de l'imagerie à un pixel aux fréquences électromagnétiques térahertz (THz) avec l'utilisation d'un modulateur de type microsystème électromécaniques (MEMS)*. ÉCOLE DE TECHNOLOGIE SUPÉRIEURE UNIVERSITÉ DU QUÉBEC.

Béliveau, L.-P. (2022b). *Développement de l'imagerie à un pixel aux fréquences électromagnétiques térahertz (THz) avec l'utilisation d'un modulateur de type microsystème électromécaniques (MEMS)*. École de technologie supérieure.

Bhugra, H., & Piazza, G. (Eds.). (2017). *Piezoelectric MEMS Resonators*. Springer International Publishing. https://doi.org/10.1007/978-3-319-28688-4

Bogue, R. (2018). Sensing with terahertz radiation: A review of recent progress. *Sensor Review*, *38*(2), 216–222. https://doi.org/10.1108/SR-10-2017-0221

Bonfiglioli, G., & Brovetto, P. (1964). Principles of Self-Modulating Derivative Optical Spectroscopy. *Applied Optics*, *3*(12), 1417. https://doi.org/10.1364/AO.3.001417

Collier, G. L., & Singleton, F. (1957). Infra-red analysis by the derivative method. *Journal of Applied Chemistry*, *7*(4), 204–204. https://doi.org/10.1002/jctb.5010070408

Coutaz, J.-L., Garet, F., & Wallace, V. P. (2018). *Principles of terahertz time-domain spectroscopy*. Pan Stanford publ.

Cox, J. A., Higashi, R., Nusseibeh, F., Newstrom-Peitso, K., Zins, C., Osiander, R., Lehtonen, J., & Dodson, E. (2009). *Uncooled MEMS-based detector arrays for THz imaging applications* (M. Anwar, N. K. Dhar, & T. W. Crowe, Eds.; p. 73110R). https://doi.org/10.1117/12.818766

CPT-7502-65-SMT-TR Same Sky | Mouser. (2024). Mouser Electronics. https://www.mouser.ca/ProductDetail/Same-Sky/CPT-7502-65-SMT-TR?qs=HoCaDK9Nz5cKdJajIU0%2Fjw%3D%3D

CPT-9019S-SMT-TR | Audio Transducers | Buzzers. (2024). https://www.sameskydevices.com/product/audio/buzzers/audio-transducers/cpt-9019s-smt-tr

Cui, H., Zhang, X., Su, J., Yang, Y., Fang, Q., & Wei, X. (2015). Vibration–rotation absorption spectrum of water vapor molecular in frequency selector at 0.5–2.5 THz range. *Optik*, *126*(23), 3533–3537. https://doi.org/10.1016/j.ijleo.2015.08.066

Da Dalt, N., & Sheikholeslami, A. (2018). *Understanding Jitter and Phase Noise: A Circuits and Systems Perspective* (1st ed.). Cambridge University Press. https://doi.org/10.1017/9781316981238

Da Silva, I. J. G., Raimundo, I. M., & Mizaikoff, B. (2022). Analysis of sugars and sweeteners *via* terahertz time-domain spectroscopy. *Analytical Methods*, *14*(27), 2657–2664. https://doi.org/10.1039/D2AY00377E

Dragoman, D., & Dragoman, M. (2004). Terahertz fields and applications. *Progress in Quantum Electronics*, *28*(1), 1–66. https://doi.org/10.1016/S0079-6727(03)00058-2

Dubuc, D., Saddaoui, M., Melle, S., Flourens, F., Rabbia, L., Ducarouge, B., Grenier, K., Pons, P., Boukabache, A., Bary, L., Takacs, A., Aubert, H., Vendier, O., Roux, J. L., & Plana, R. (2004). Smart MEMS concept for high secure RF and millimeterwave communications. *Microelectronics Reliability*, *44*(6), 899–907. https://doi.org/10.1016/j.microrel.2004.02.008

Duvillaret, L., Garet, F., & Coutaz, J.-L. (2000). Influence of noise on the characterization of materials by terahertz time-domain spectroscopy. *JOSA B*, *17*(3), 452–461.

Filin, A., Stowe, M., & Kersting, R. (2001). Time-domain differentiation of terahertz pulses. *Optics Letters*, *26*(24), 2008–2010.

Fischer, B. M. (2005). *Broadband THz time-domain spectroscopy of biomolecules: A comprehensive study of the dielectric properties of biomaterials in the far-infrared* [Albert-Ludwigs-Universitat]. https://d-nb.info/98063623X/34

Franz, M., Fischer, B. M., & Walther, M. (2008). The Christiansen effect in terahertz time-domain spectra of coarse-grained powders. *Applied Physics Letters*, *92*(2).

Ghann, W., & Uddin, J. (2017). Terahertz (THz) Spectroscopy: A Cutting-Edge Technology. In J. Uddin (Ed.), *Terahertz Spectroscopy—A Cutting Edge Technology*. InTech. https://doi.org/10.5772/67031

Giese, A. T., & French, C. S. (1955). The analysis of overlapping spectral absorption bands by derivative spectrophotometry. *Applied Spectroscopy*, *9*(2), 78–96.

Gordon, D. F., Ting, A., Alexeev, I., Fischer, R., Sprangle, P., Kapetenakos, C. A., & Zigler, A. (2006). Tunable, high peak power terahertz radiation from optical rectification of a short modulated laser pulse. *Optics Express*, *14*(15), 6813. https://doi.org/10.1364/OE.14.006813

Han, N., De Geofroy, A., Burghoff, D. P., Chan, C. W. I., Lee, A. W. M., Reno, J. L., & Hu, Q. (2014). Broadband all-electronically tunable MEMS terahertz quantum cascade lasers. *Optics Letters*, *39*(12), 3480. https://doi.org/10.1364/OL.39.003480

Hirori, H., Doi, A., Blanchard, F., & Tanaka, K. (2011). Single-cycle terahertz pulses with amplitudes exceeding 1 MV/cm generated by optical rectification in LiNbO3. *Applied Physics Letters*, *98*(9), 091106. https://doi.org/10.1063/1.3560062

Huang, H., Shao, S., Wang, G., Ye, P., Su, B., & Zhang, C. (2022). Terahertz spectral properties of glucose and two disaccharides in solid and liquid states. *iScience*, *25*(4), 104102. https://doi.org/10.1016/j.isci.2022.104102

Huang, Y., Sai Sarathi Vasan, A., Doraiswami, R., Osterman, M., & Pecht, M. (2012). MEMS Reliability Review. *IEEE Transactions on Device and Materials Reliability*, *12*(2), 482–493. https://doi.org/10.1109/TDMR.2012.2191291

Jepsen, P. U., Cooke, D. G., & Koch, M. (2011). Terahertz spectroscopy and imaging – Modern techniques and applications. *Laser & Photonics Reviews*, *5*(1), 124–166. https://doi.org/10.1002/lpor.201000011

Jiang, Z., Li, M., & Zhang, X. C. (2000). Dielectric constant measurement of thin films by differential time-domain spectroscopy. *Applied Physics Letters*, *76*(22), 3221–3223. https://doi.org/10.1063/1.126587

Karpinska, J. (2004). Derivative spectrophotometry-recent applications and directions of developments. *Talanta*, *64*(4), 801–822. https://doi.org/10.1016/j.talanta.2004.03.060

King, E. E., Sullivan, M., Kato, E., & Heaps, D. (2013). Pharmaceutical, biological and industrial applications of terahert spectroscopy and imaging for IRMMW-THz 2013. *2013 38th International Conference on Infrared, Millimeter, and Terahertz Waves (IRMMW-THz)*, 1–2. https://doi.org/10.1109/IRMMW-THz.2013.6665846

Klein, M. P., & Dratz, E. A. (1968). Derivative Spectroscopy with Recording Spectrometers. *Review of Scientific Instruments*, *39*(3), 397–399. https://doi.org/10.1063/1.1683382

Kloos, G. (2018). *Applications of lock-in amplifiers in optics*. SPIE Press.

Langner, P. H., & Geselowitz, D. B. (1962). First Derivative of the Electrocardiogram. *Circulation Research*, *10*(2), 220–226. https://doi.org/10.1161/01.RES.10.2.220

Li, C., Zhang, Y., & Hirakawa, K. (2023). Terahertz Detectors Using Microelectromechanical System Resonators. *Sensors*, *23*(13), 5938. https://doi.org/10.3390/s23135938

Li, D., & Ma, G. (2008). Pump-wavelength dependence of terahertz radiation via optical rectification in (110)-oriented ZnTe crystal. *Journal of Applied Physics*, *103*(12), 123101. https://doi.org/10.1063/1.2938847

Lin, Y.-J., & Jarrahi, M. (2020). Heterodyne terahertz detection through electronic and optoelectronic mixers. *Reports on Progress in Physics*, *83*(6), 066101. https://doi.org/10.1088/1361-6633/ab82f6

Liu, H.-B., Zhong, H., Karpowicz, N., Chen, Y., & Zhang, X.-C. (2007). Terahertz Spectroscopy and Imaging for Defense and Security Applications. *Proceedings of the IEEE*, *95*(8), 1514–1527. https://doi.org/10.1109/JPROC.2007.898903

Liu, Y., Zhou, T., & Cao, J.-C. (2019). Terahertz spectral of enantiomers and racemic amino acids by time-domain-spectroscopy technology. *Infrared Physics & Technology*, *96*, 17–21. https://doi.org/10.1016/j.infrared.2018.10.026

Mahalik, N. P. (2008). Principle and applications of MEMS: A review. *International Journal of Manufacturing Technology and Management*, *13*(2/3/4), 324. https://doi.org/10.1504/IJMTM.2008.016780

Mahdavi, M., Ramezany, A., Kumar, V., & Pourkamali, S. (2015). SNR improvement in amplitude modulated resonant MEMS sensors via thermal-piezoresistive internal

amplification. *2015 28th IEEE International Conference on Micro Electro Mechanical Systems (MEMS)*, 913–916. https://doi.org/10.1109/MEMSYS.2015.7051108

Mittleman, D. (Ed.). (2003). *Sensing with Terahertz Radiation* (Vol. 85). Springer Berlin Heidelberg. https://doi.org/10.1007/978-3-540-45601-8

Mouser Electronics. (2024). *Piezo MEMS Speaker*. https://www.mouser.com/datasheet/2/334/APS2509S-T-R-270437.pdf

Naftaly, M. (2013). Metrology Issues and Solutions in THz Time-Domain Spectroscopy: Noise, Errors, Calibration. *IEEE Sensors Journal*, *13*(1), 8–17. https://doi.org/10.1109/jsen.2012.2208624

Naftaly, M., & Dudley, R. (2009). Methodologies for determining the dynamic ranges and signal-to-noise ratios of terahertz time-domain spectrometers. *Optics Letters*, *34*(8), 1213–1215.

Nagatsuma, T. (2011). Terahertz technologies: Present and future. *IEICE Electronics Express*, *8*(14), 1127–1142. https://doi.org/10.1587/elex.8.1127

Nakagawa, M., Kanda, N., Otsu, T., Ito, I., Kobayashi, Y., & Matsunaga, R. (2023). Jitter correction for asynchronous optical sampling terahertz spectroscopy using free-running pulsed lasers. *Opt Express*, *31*(12), 19371–19381. https://doi.org/10.1364/OE.488866

Neu, J., & Schmuttenmaer, C. A. (2018). Tutorial: An introduction to terahertz time domain spectroscopy (THz-TDS). *Journal of Applied Physics*, *124*(23), 231101. https://doi.org/10.1063/1.5047659

Nsengiyumva, W., Zhong, S., Zheng, L., Liang, W., Wang, B., Huang, Y., Chen, X., & Shen, Y. (2023). Sensing and Nondestructive Testing Applications of Terahertz Spectroscopy and Imaging Systems: State-of-the-Art and State-of-the-Practice. *IEEE Transactions*

on Instrumentation and Measurement, *72*, 1–83. https://doi.org/10.1109/TIM.2023.3318676

Nuss, M. C., & Orenstein, J. (2007). Terahertz time-domain spectroscopy. *Millimeter and Submillimeter Wave Spectroscopy of Solids*, 7–50.

Oberhammer, J. (2018). Micromachined THz Systems—Enabling the Large-Scale Exploitation of the THz Frequency Spectrum. *2018 Asia-Pacific Microwave Conference (APMC)*, 25–27. https://doi.org/10.23919/APMC.2018.8617359

Pacheco-Peña, V. (2021). Terahertz Technologies and Its Applications. *Electronics*, *10*(3), 268. https://doi.org/10.3390/electronics10030268

Pawar, A. Y., Sonawane, D. D., Erande, K. B., & Derle, D. V. (2013). Terahertz technology and its applications. *Drug Invention Today*, *5*(2), 157–163. https://doi.org/10.1016/j.dit.2013.03.009

Pemsler, J. P. (1957). Method of Obtaining Derivative Spectra. *Review of Scientific Instruments*, *28*(4), 274–275. https://doi.org/10.1063/1.1715857

Petrov, V., Pyattaev, A., Moltchanov, D., & Koucheryavy, Y. (2016). Terahertz band communications: Applications, research challenges, and standardization activities. *2016 8th International Congress on Ultra Modern Telecommunications and Control Systems and Workshops (ICUMT)*, 183–190. https://doi.org/10.1109/ICUMT.2016.7765354

Phase Noise in Oscillators—MATLAB & Simulink. (2024). https://www.mathworks.com/help/msblks/ug/phase-noise-in-oscillators.html?s_tid=srchtitle_site_search_3_phase%20noise

Pitchappa, P., Kumar, A., Singh, R., Lee, C., & Wang, N. (2021). Terahertz MEMS metadevices. *Journal of Micromechanics and Microengineering*, *31*(11). https://doi.org/10.1088/1361-6439/ac1eed

Pulikkoonattu, R. (2007). *OSCILLATOR PHASE NOISE AND SAMPLING CLOCK JITTER*. ST Microelectronics.

Roux, J.-F., Garet, F., & Coutaz, J.-L. (2014). Principles and Applications of THz Time Domain Spectroscopy. In M. Perenzoni & D. J. Paul (Eds.), *Physics and Applications of Terahertz Radiation* (Vol. 173, pp. 203–231). Springer Netherlands. https://doi.org/10.1007/978-94-007-3837-9_8

Schmitt, L., Liu, X., Czylwik, A., & Hoffmann, M. (2021). Design and Fabrication of MEMS Reflectors for THz Reflect-Arrays. *2021 Fourth International Workshop on Mobile Terahertz Systems (IWMTS)*, 1–5. https://doi.org/10.1109/IWMTS51331.2021.9486804

Sharma, G., Singh, K., Ibrahim, A., Al-Naib, I., Morandotti, R., Vidal, F., & Ozaki, T. (2013). Self-referenced spectral domain interferometry for improved signal-to-noise measurement of terahertz radiation. *Optics Letters*, *38*(15), 2705. https://doi.org/10.1364/OL.38.002705

Smith, R. C. (1963). Resolution in the Derivative Recording of Absorption Spectra. *Review of Scientific Instruments*, *34*(3), 296–297. https://doi.org/10.1063/1.1718336

Song, H.-J., & Nagatsuma, T. (2011). Present and Future of Terahertz Communications. *IEEE Transactions on Terahertz Science and Technology*, *1*(1), 256–263. https://doi.org/10.1109/TTHZ.2011.2159552

Stauffer, F. R., & Sakai, H. (1968). Derivative spectroscopy. *Applied Optics*, *7*(1), 61–65.

Sun, Q., He, Y., Liu, K., Fan, S., Parrott, E. P. J., & Pickwell-MacPherson, E. (2017). Recent advances in terahertz technology for biomedical applications. *Quantitative Imaging in Medicine and Surgery*, *7*(3), 345–355. https://doi.org/10.21037/qims.2017.06.02

Tani, M., Herrmann, M., & Sakai, K. (2002). Generation and detection of terahertz pulsed radiation with photoconductive antennas and its application to imaging. *Measurement Science and Technology*, *13*(11), 1739–1745. https://doi.org/10.1088/0957-0233/13/11/310

Terjani, B., Hamoud-Michel, H., BOIVIN, P., & Desbiens, R. (2023). *CONTRÔLEUR D'ACTUATEUR MATRICIEL DE TYPE MEMS POUR DES APPLICATIONS EN SPECTROSCOPIE ET IMAGERIE TÉRAHERTZ*. ÉCOLE DE TECHNOLOGIE SUPÉRIEURE UNIVERSITÉ DU QUÉBEC.

The Lock-In Amplifier: Noise Reduction and Phase Sensitive Detection. (n.d.). The University of Konstanz, Department of Physics. Retrieved October 18, 2024, from https://wp.optics.arizona.edu/jpalmer/wp-content/uploads/sites/65/2018/11/Gesamttext.pdf

The Phase Noise Challenge Pacing the Race to 5G | 2019-11-10 | Microwave Journal. (2019, November 14). https://www.microwavejournal.com/articles/33095-the-phase-noise-challenge-pacing-the-race-to-5g

Wietzke, S., Jansen, C., Krumbholz, N., Peters, O., Vieweg, N., Jordens, C., Scheller, M., Romeike, D., Jung, T., Reuter, M., Chatterjee, S., Koch, M., Physik, F., Baudrit, B., Zentgraf, T., Hochrein, T., & Bastian, M. (2010). Terahertz spectroscopy: A powerful tool for the characterization of plastic materials. *2010 10th IEEE International Conference on Solid Dielectrics*, 1–4. https://doi.org/10.1109/ICSD.2010.5567915

Withayachumnankul, W., Fischer, B. M., Lin, H., & Abbott, D. (2008). Uncertainty in terahertz time-domain spectroscopy measurement. *JOSA B*, *25*(6), 1059–1072.

Withayachumnankul, W., & Naftaly, M. (2013). Fundamentals of Measurement in Terahertz Time-Domain Spectroscopy. *Journal of Infrared, Millimeter, and Terahertz Waves*, *35*(8), 610–637. https://doi.org/10.1007/s10762-013-0042-z

Wu, Q., & Zhang, X.-C. (1995). Free-space electro-optic sampling of terahertz beams. *Applied Physics Letters*, *67*(24), 3523–3525. https://doi.org/10.1063/1.114909

Xie, J., Zhu, X., Zhang, H., Zang, X., Chen, L., Balakin, A. V., Shkurinov, A. P., & Zhu, Y. (2020). Terahertz-frequency temporal differentiator enabled by a high-Q resonator. *Opt Express*, *28*(6), 7898–7905. https://doi.org/10.1364/OE.387775

Xu, C., Ren, Z., Wei, J., & Lee, C. (2022). Reconfigurable terahertz metamaterials: From fundamental principles to advanced 6G applications. *iScience*, *25*(2), 103799. https://doi.org/10.1016/j.isci.2022.103799

Yan, Y. W. (2014). The Application of Derivative in the Field of Manufacturing and Mathematical Modeling. *Applied Mechanics and Materials*, *602–605*, 3–6. https://doi.org/10.4028/www.scientific.net/AMM.602-605.3

Zanotto, L. (2022). *Development of a scanless terahertz time-domain imaging system*. Doctorat en sciences de l'énergie et des matériaux.

Zhang, C. W., & Forbes, L. (2003). Simulation of timing jitter in ring oscillators. *Proceedings of the 15th Biennial University/Government/ Industry Microelectronics Symposium (Cat. No.03CH37488)*, 356–359. https://doi.org/10.1109/UGIM.2003.1225765

Zhang, Y., Zhang, L., Sun, P., He, Y., Zou, Y., & Deng, Y. (2016). Extracting Complex Refractive Index from Polycrystalline Glucose with Self-Referenced Method for

Terahertz Time-Domain Reflection Spectroscopy. *Appl Spectrosc*, *70*(7), 1102–1108. https://doi.org/10.1177/0003702816652318

Zurich Instruments. (2023, April). *Principles of lock-in detection and the state of the art*. https://www.zhinst.com/sites/default/files/documents/2023-04/zi_whitepaper_principles_of_lock-in_detection_0.pdf